



**WICHITA STATE
UNIVERSITY**

UNIVERSITY LIBRARIES

Reliability analysis and anomaly detection considering long-range dependence effects

Item Type	Dissertation
Authors	Shao, Yunfei
Publisher	Wichita State University
Rights	© Copyright 2023 by Yunfei Shao All Rights Reserved
Download date	2026-05-17 23:40:58
Link to Item	https://soar.wichita.edu/handle/10057/25411

RELIABILITY ANALYSIS AND ANOMALY DETECTION CONSIDERING LONG-RANGE
DEPENDENCE EFFECTS

A Dissertation by

Yunfei Shao

Bachelor of Science, University of Science and Technology of China, China, 2016

Submitted to the Department of the Industrial and Manufacturing Engineering
and the faculty of the Graduate School of
Wichita State University
in partial fulfillment of
the requirements for the degree of
Doctor of Philosophy

May 2023

© Copyright 2023 by Yunfei Shao

All Rights Reserved

RELIABILITY ANALYSIS AND ANOMALY DETECTION CONSIDERING LONG-RANGE
DEPENDENCE EFFECTS

The following faculty members have examined the final copy of this dissertation for form and content, and recommend that it be accepted in partial fulfillment of the requirement for the degree of Doctor of Philosophy with major in Industrial Engineering.

Wujun Si, Committee Chair

Krishna Krishnan, Committee Member

Mehmet Bayram Yildirim, Committee Member

Enkhsaikhan Boldsaikhan, Committee Member

Wei Wei, Committee Member

Accepted for the College of Engineering

Anthony Muscat, Dean

Accepted for the Graduate School

Coleen Pugh, Dean

DEDICATION

To my beloved family
for their unconditional love and support

ACKNOWLEDGEMENTS

I would like to express my sincere gratitude to several individuals that supported me to complete this doctoral dissertation. I am highly grateful to my advisor, Professor Wujun Si, for his thoughtful guidance and scholarly support. I would like to extend my gratitude to my committee members, Professor Krishna Krishnan, Professor Mehmet Bayram Yildirim, Professor Enkhsaikhan Boldsaikhan, and Professor Wei Wei, for their kindly support and constructive advice for my research. I also want to thank all my family. This dissertation could not be completed without the unconditional love and support from my family. I would also like to thank all of my professors for years of advice and instruction.

ABSTRACT

Reliability analysis and anomaly detection are crucial to the Prognostics and Health Management (PHM) of modern complex systems. Recently, with the advancement of measurement technology, a Long-Range Dependence/Long-Term Memory (LRD/LTM) effect has recently been detected in reliability and quality monitoring fields. The LRD effect is a type of non-Markovian property and refers to the high dependence between two measurements across a long-time interval or a long-distance range. In mathematics, the LRD effect indicates that the autocorrelation of the metrics is non-summable. In reliability and anomaly detection fields, most studies have been conducted ignoring the LRD effect, which could incur some serious issues, such as biased lifetime prediction or inaccurate anomaly detection. To overcome these challenges, we propose novel reliability analysis and anomaly detection approaches to integrate the LRD effect. Specifically, in Chapter 2 we propose a reliability analysis considering the LRD effect and random errors simultaneously under normal operating conditions. In Chapter 3, we develop a reliability analysis integrating the LRD effect under accelerated conditions. In Chapter 4, we propose a quality control analysis on surface anomaly detection considering LRD. In Chapter 5, we develop an LRD-integrated anomaly detection using 3D composite structure information. Results show that the proposed LRD-integrated approaches, by considering the LRD effect, significantly outperforms the conventional models that ignore the LRD effect.

TABLE OF CONTENTS

Chapter	Page
INTRODUCTION	1
1.1 Literature Review on Reliability Analysis.....	2
1.2 Literature Review on Anomaly detection.....	4
1.3 Dissertation Overview	5
RELIABILITY ANALYSIS CONSIDERING THE LRD EFFECT AND RANDOM ERRORS UNDER NORMAL OPERATING CONDITIONS.....	6
2.1 Introduction.....	6
2.2 The Proposed Degradation Model.....	10
2.2.1 Fixed-Effect Scenario.....	10
2.2.2 Random-Effect Scenario	13
2.3 Reliability Analysis.....	17
2.4 Simulation Study.....	18
2.4.1 Fixed-Effect Model	19
2.4.2 Random-Effect Model.....	22
2.5 Case Study	26
2.5.1 Case Data Description.....	26
2.5.2 Parameter Estimation	27
2.5.3 Model Comparison.....	28
2.6 Conclusion	33
RELIABILITY ANALYSIS CONSIDERING THE LRD EFFECT UNDER ACCELERATED CONDITIONS.....	35
3.1 Introduction.....	35
3.2 Statistical Model	39
3.2.1 Long-Range Dependence Effect	39
3.2.2 ADT Modeling with Long-Range Dependence	41
3.2.3 Life Estimation under Normal Use Condition	44
3.3 Model Parameter Estimation	47
3.4 Hypothesis Test of Memory Effect.....	50
3.5 Simulation Study.....	51
3.5.1 Data Simulation.....	51
3.5.2 Model Parameter Estimation.....	52
3.5.3 Test of Degradation Memory Effect	53
3.5.4 Lifetime Distribution.....	54
3.5.5 Model Comparison.....	55

TABLE OF CONTENTS (continued)

Chapter	Page
3.6 Case Study	57
3.6.1 Experimental and Data Collection	57
3.6.2 Data Analysis and Parameter Estimation	59
3.6.3 Test of Degradation Memory Effect	60
3.6.4 Lifetime Estimation.....	60
3.6.5 Model Comparison.....	61
3.7 Conclusion	63
SURFACE ANOMALY DETECTION CONSIDERING LONG-RANGE DEPENDENCE	
4.1 Introduction.....	65
4.1.1 Motivation.....	65
4.1.2 Related Literature Review.....	67
4.1.3 Overview of the Proposed Work.....	70
4.2 An LRD-Integrated Spatial Model	71
4.2.1 Preliminaries on the LRD Effect.....	71
4.2.2 The Isotropic LRD-Integrated Spatial Model	74
4.2.3 The Anisotropic LRD-Integrated Spatial Model.....	75
4.3 LRD-Integrated Surface Monitoring	77
4.3.1 In-Control Surface Parameters Identification	77
4.3.2 A GLRT-based Surface Monitoring Framework	79
4.4 Simulation Study.....	81
4.4.1 Isotropic Scenario.....	82
4.4.2 Anisotropic Scenario	87
4.5 Case Study	92
4.5.1 Data Description.....	92
4.5.2 Parameter Estimation	93
4.5.3 Surface Anomaly Detection	94
4.5.4 Model Comparison.....	95
4.6 Conclusion	96
LRD-INTEGRATED STATISTICAL MONITORING USING 3D STRUCTURE INFORMATION	
5.1 Introduction.....	98
5.1.1 Background and Motivation.....	98
5.1.2 Literature Review.....	99
5.1.3 Outline of the Proposed Model	101
5.2 The Proposed model	102

TABLE OF CONTENTS (continued)

Chapter	Page
5.2.1 The Long-Range Dependence in 3D Space	102
5.2.2 The LRD-Integrated 3D Model.....	104
5.3 LRD-Integrated Material Monitoring using 3D Structure Information.....	106
5.3.1 An MLE Approach for model parameter estimation	106
5.3.2 A Multivariate HT-type Control Chart.....	108
5.3.3 A GLRT-based Control Chart.....	109
5.4 Simulation Study.....	111
5.4.1 3D Structure Simulation.....	111
5.4.2 Model Parameter Estimation and Product Monitoring	114
5.5 Case Study	115
5.5.1 Experiment and Data Collection Process	116
5.5.2 A Generative Adversarial Network.....	117
5.5.3 Parameter Estimation and Composite Monitoring.....	118
5.6 Conclusion	120
CONCLUSIONS AND FUTURE WORKS	121
REFERENCES	125
APPENDIXES	142

LIST OF TABLES

Table	Page
2-1. Point Estimates and Standard Errors of P_1 Parameters	20
2-2. RMSEs of Parameter Estimation of P_1 under Different Sample Sizes.....	21
2-3. Point Estimates and Standard Errors of P_2 Parameters	21
2-4. Point Estimates and Standard Errors of P_3 Parameters	23
2-5. RMSEs of Parameter Estimation of P_3 under Different Sample Sizes.....	24
2-6. Point Estimates and Standard Errors of P_4 Parameters	25
2-7. Point Estimates and Standard Errors of P_5 and P_6 Parameters.....	28
2-8. Point Estimates and Standard Errors of P_7 and P_8 Parameters.....	29
2-9. Point Estimates and Standard Errors of P_B Parameters	31
2-10. Life Means, Standard deviations, and BICs of $P_5 \sim P_8$ and P_B	32
2-11. Point Estimates and Standard Errors of P_R Parameters	33
3-1. Point and Standard Error Estimation of M_1 Parameters	53
3-2. RMSEs of Parameter Estimation under Different Sample Sizes.....	53
3-3. Point and Standard Error Estimation of M_2 Parameters	55
3-4. Point and Standard Error Estimation of M_{random} Parameters	56
3-5. Log-likelihood Values and BIC Values of M_1 , M_2 and M_{random}	57
3-6. Parameter Estimation Results of M_1 and M_3	59
3-7. Parameter Estimation Results of M_2 and M_4	61
3-8. Log-likelihood Values and BIC Values of $M_1 \sim M_4$	63
4-1. Five Settings of Out-of-control Surfaces.....	82
4-2. The Point Estimates and Standard Errors of M_1 Parameters	84
4-3. RMSEs of Parameter Estimation of M_1 under Different Image Sizes.....	85

LIST OF TABLES (continued)

Table	Page
4-4. Detection Power and ARL_1 for Model M_1 under Five Out-of-control Settings at $q = 0.0027$	86
4-5. ARL_1 of $M_1 \sim M_4$ under Five Out-of-control Settings at $q = 0.0027$	87
4-6. Six Settings of Out-of-control Surfaces.....	88
4-7. Point Estimates and Standard Errors of M_5 Parameters	90
4-8. RMSEs of Parameter Estimation of M_5 under Different Image Sizes.....	90
4-9. ARL_1 of M_5 under Six Out-of-control Settings at $q = 0.0027$	91
4-10. ARL_1 of $M_5 \sim M_8$ under Six Settings of Out-of-control Surfaces at $q = 0.0027$	92
4-11. Four Settings of Out-of-control Surfaces	93
4-12. Point Estimates and Standard Errors of M_9 and M_{10} Parameters.....	94
4-13. ARL_1 of Models M_9 and M_{10} on Surface Anomaly Detection at $q = 0.0027$	95
4-14. ARL_1 of Models $M_9 \sim M_{15}$ at $q = 0.0027$	96
5-1. Five Settings of Out-of-control Structures along with the In-control Setting	112
5-2. The Point Estimates and Standard Errors of P_1 Parameters of In-control Samples	114
5-3. ARL_1 of P_1 under Five Out-of-control Settings at Nominal $ARL_0 = 370$	115
5-4. The point Estimates and Standard Errors of P_1 Parameters of In-control Samples.....	119
5-5. ARL_1 s and Detection Power of P_2 using HT-type and GLRT-based charts at Nominal $ARL_0 = 370$	119
A-1. Point Estimates and Standard Errors of P_3 Parameters under Three Levels of Measurement Errors.....	146

LIST OF FIGURES

Figure	Page
1.1. (a) A Capacity degradation signal of a lithium-ion battery; (b) A wood surface image; (c) A 3D-printed carbon composite sample	2
2.1. Simulated degradation paths using model P_1	19
2.2. PDFs of predicted lifetime using P_1 and P_2	22
2.3 Simulated degradation paths using model P_3	23
2.4. Predicted lifetime distributions using P_3 and P_4	25
2.5. Degradation paths of eight Kokam 740 mAh lithium-ion pouch cells (loss of capacity vs. degradation cycle).....	27
2.6. PDFs of predicted lifetime using models P_5 and P_7	29
2.7. PDFs of predicted lifetime using models P_6 and P_8	30
2.8. PDFs of predicted lifetime using models P_5 and P_6	30
2.9. PDFs of predicted lifetime calculated by models P_6 and P_B	31
3.1. Simulated degradation paths at three accelerated temperature levels.....	52
3.2. PDFs of lifetime at normal use temperature with different failure threshold values.....	54
3.3. PDFs of lifetime at normal use temperature for M_1 and M_2	56
3.4 The accelerated testing system (left) and normalized performance degradation of Pt/black TiO ₂ at two accelerated temperatures (right).....	59
3.5. Predicted lifetime distribution at 450°C	61
3.6. Lifetime distribution prediction at normal use temperature of M_1 versus M_2 (left) and M_3 versus M_4 (right).....	63
4.1. (a) A wood surface with the LRD effect along the vertical direction; (b) A silver surface with the LRD effect along the horizontal direction; (c) Autocorrelation (absolute value) function of the wood surface in the vertical direction, along with the fitted exponential curve; (d) Autocorrelation (absolute value) function of the silver surface in the horizontal direction, along with the fitted exponential curve.....	67
4.2. (a) In-control surface; (b) Out-of-control surface under Setting 1; (c) Out-of-control surface under Setting 4	84

LIST OF FIGURES (continued)

Figure	Page
4.3. (a) In-control surface; (b) Out-of-control surface under Setting 1; (c) Out-of-control surface under Setting 5	89
4.4. (a) In-control wood surface; (b) Out-of-control wood surface under Setting 2; (c) Out-of-control wood surface under Setting 3	93
5.1. 1st, 3rd, 5th, 7th and 9th images of the first sample of in-control setting	114
5.2. 1st, 3rd, 5th, 7th and 9th images of the first sample of out-of-control setting.....	114
5.3. 1st, 3rd, 5th, 7th and 9th cross-sectional slices of the first sample of in-control samples....	117
5.4. 1st, 3rd, 5th, 7th and 9th cross-sectional slices of the first sample of out-of-control samples	117
5.5. 1st, 3rd, 5th, 7th and 9th cross-sectional slices of a generated in-control sample	118
5.6. 1st, 3rd, 5th, 7th and 9th cross-sectional slices of a generated out-of-control sample	118
A.1. PDFs of predicted lifetime using P_3 when $d^2 = 0.1, 0.5$ and 1.0	147
A.2. $P(Y \leq 1)$ for small t (left) and $P(Y \geq 0)$ for large t (right) of the simulation study	148
A.3. $P(Y \leq 1)$ for small t (left) and $P(Y \geq 0)$ for large t (right) of the case study	148

CHAPTER 1

INTRODUCTION

Reliability analysis and anomaly detection refer to lifetime analysis and quality assessment of assets, which are crucial to the Prognostics and Health Management (PHM) of modern complex systems [1-3]. Recently, by virtue of advances in the measurement technology, a Long-Range dependence (LRD) effect has been detected in several complex systems/assets, such as turbofan engines [4], chemical catalysts [5], lithium-ion batteries [6], and blast furnaces [7]. The LRD effect (also entitled as long-range persistence) is a type of non-Markovian property and refers to that the health/quality metrics of the asset are highly correlated over a long time range or a long spatial distance [5]. The LRD effect has been detected in various data from one-dimensional to three-dimensional. In mathematics, the LRD effect indicates that the auto-correlation functions of the metrics are non-summable. Specifically, in reliability field, the LRD effect implies that the future degradation behavior of complex systems not only depends on the current asset health status but also highly correlates with the entire degradation history. In material/product monitoring field, the LRD effect indicates that structures/properties of two points on material are highly dependent even though they are distant from each other. In addition to the reliability analysis and anomaly detection, the LRD effect has also been observed in many other fields such as finance [8], hydrology [9] and biology [10]. Figure 1.1 shows the LRD effect from one-dimensional case to three-dimensional case. Specifically, Figure 1.1 (a) presents a degradation signal of a lithium-ion battery that holds the one-dimensional temporal LRD effect; Figure 1.1 (b) presents a wood surface that holds the two-dimensional spatial LRD effect; and Figure 1.1 (c) presents a 3D-printed carbon

composite that holds the three-dimensional spatial LRD effect. Due to the widespread existence and criticality of LRD effects, it is meaningful to develop the LRD-integrated reliability analysis and anomaly detection.

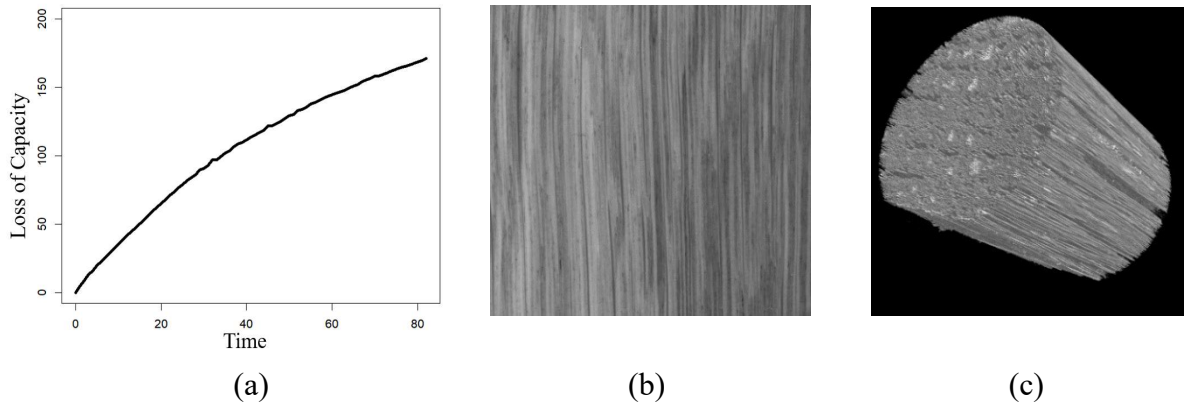


Figure 1.1. (a) A Capacity degradation signal of a lithium-ion battery; (b) A wood surface image; (c) A 3D-printed carbon composite sample

1.1 Literature Review on Reliability Analysis

Reliability analysis is to study the ability of systems/assets to function under a good condition for a period of time, which is critical to manufacturing fields, such as product lifetime prediction [11], remaining useful life prediction [4], and accelerated lifetime prediction [12]. In reliability analysis, two types of data are widely used, including lifetime data [13] and degradation data [11]. The lifetime data only record lifetimes of all products, while the degradation data record whole degradation trajectories of all products. Hence, the degradation data contains more information. Therefore, we select to apply the degradation data in this dissertation.

In the literature of reliability analysis on degradation modeling, most existing models ignore the LRD effect. These models can generally be classified into three groups, i.e., physical models [14, 15], statical process models [16-18], and Artificial Intelligence (AI) models [19-21].

For the physical models, Hack, et al. [14] developed physical models for degradation of polysilicon thin-film transistors. Vichard, et al. [15] illustrated several physical models to predict the lifetime for solar panels. Although these physical models have been widely applied, two limitations are that they are not efficient enough to characterize the stochastic behavior, and they usually require rigorous physical laws, which are difficult to obtain in many practical cases. To better capture the randomness within degradation signals, some researchers studied ADT data using some statistical models such as Wiener process [16], geometric Brownian motion [17], Gamma process [18] and Inverse Gaussian process models [22]. However, these models cannot capture the long-range dependence. Recently, some AI methods have also been developed for degradation analysis. For example, a generic health index approach [19], a multiscale convolutional neural network model [20], and a deep-learning-based data fusion approach [21]. However, none of these methods can capture the LRD effect.

To track the LRD effect in the reliability analysis, some researchers adopted the Fractional Brownian Motion (FBM) [4, 6]. It has to be mentioned that only a few LRD studies have been conducted in the reliability field with a focus on very specific applications. For example, Xi, et al. [4] proposed a degradation model with LRD effect to predict the remaining useful life of turbo engines under normal operating conditions. Zhang, et al. [23] incorporated multiple degradation modes into an FBM-based degradation model without considering measurement errors. However, all of the aforementioned methods did not consider the LRD effect in more general operating settings, such as accelerated conditions and the existence of random errors, which could result in biased lifetime prediction and incur high costs.

1.2 Literature Review on Anomaly detection

As a main cause of failure, product anomaly detection has been receiving increasing attention in statistical process control (SPC). The characteristics of products highly impact material properties such as strength, stiffness, and damage-resistance, which in turn significantly influence product quality and usage life. Therefore, it is crucial to build efficient spatial anomaly detection models that can accurately characterize those complex characteristics of products and detect the anomalies within products.

In anomaly detection literature, most conventional methods do not consider the LRD effect. For product anomaly detection monitoring, parametric, semi-parametric and non-parametric methods have been developed in the literature. In parametric methods, researchers commonly develop a specific parametric spatial model to characterize material surface measurements and reduce the data dimension to a small set of model parameters, based on which a multivariate control chart is established for monitoring purposes. For example, Colosimo [24] detected metal defects using a spatial autoregressive model with exogenous variables. Baek, et al. [25] developed a multimode nearest neighbor method for monitoring multimode surfaces based on a nonlinear spatial model. For semi-parametric methods, Bui and Apley [26] developed a semi-parametric autoregressive model to detect anomaly on textile surfaces. Lyu and Chen [27] constructed an automated vision inspection system to inspect anomalies using Hotelling's T^2 control chart. In addition to the parametric and semi-parametric methods, some non-parametric methods have also been proposed to monitor material surfaces. For instance, Qiu, et al. [28] proposed a nonparametric mixed-effect model to capture the spatial variance structure of materials and develop a quality control analysis based on the estimated variance structure. Ulker [29]

conducted a surface quality control of fiber sandwich boards using surface roughness as a quality tool.

However, all of the aforementioned anomaly detection approaches can only consider the spatial dependence to a limited order. This is, these conventional monitoring methods ignore the LRD effect, which can result in poor surface anomaly detection if the spatial LRD actually presents. In practice, some of the product structures demonstrate a spatial LRD as shown in Figure 1.1. Therefore, it is critical to integrate the spatial LRD effect into the product anomaly detection approach.

1.3 Dissertation Overview

To overcome aforementioned challenges, in this research we propose both reliability analyses and anomaly detections with the consideration of the LRD effect. Specifically, in Chapter 2 we develop a reliability analysis considering the LRD effect and random errors simultaneously under normal operating conditions. In Chapter 3, we propose a reliability analysis integrating the LRD effect under accelerated conditions. In Chapter 4, we develop a quality control analysis on surface anomaly detection considering LRD. In Chapter 5, we propose LRD-integrated statistical monitoring using 3D structure information. Results show that the proposed LRD-integrated reliability analysis and anomaly detection, by integrating the LRD effect, significantly outperforms the conventional models that ignore the LRD effect.

CHAPTER 2

RELIABILITY ANALYSIS CONSIDERING THE LRD EFFECT AND RANDOM ERRORS UNDER NORMAL OPERATING CONDITIONS

2.1 Introduction

Degradation modeling and reliability analysis are crucial to the prognostics and health management (PHM) of modern complex systems [1-3]. Recently, by virtue of advances in measurement technology, a long-range dependence (LRD) effect has been detected in the degradation data of many assets, including turbofan engines [4], blast furnaces [7], lithium-ion batteries [6] and chemical catalysts [5]. The LRD effect (also referred to as long-range dependence or long-range persistence) is a type of non-Markovian property and refers to the fact that the increments of asset degradation are highly correlated over a long time range [5]. That is, future degradation behavior not only depends on the current asset health status but also highly correlates with the entire degradation history. In addition to the performance degradation of assets, the LRD effect has also been observed in many other fields, such as finance [8], hydrology [9], and biology [10]. Due to the widespread existence and importance of LRD effects, several LRD -integrated degradation models have recently been proposed for asset degradation modeling and reliability analysis [30-32].

In the real world, it is inevitable that most degradation data are contaminated by measurement errors due to a variety of technical limitations. The measurement error, also referred to as observational error, has been widely studied in various research fields, including psychology [33], biology [34], healthcare [35], chemistry [36], and reliability [37]. Research has shown that ignoring measurement errors can cause several serious problems. For example, in the healthcare

field, Hutcheon, et al. [35] discovered that the failure to consider measurement errors in systolic blood pressure measurement would lead to a biased correlation quantification between systolic blood pressure and the left ventricular mass index. Another example, in psychology, is that ignoring measurement errors of the response in a job satisfaction survey significantly increased the rate of drawing a false conclusion [33]. In the context of reliability analysis, Liu and Wang [37] demonstrated that ignoring measurement errors would result in an inaccurate lifetime prediction. Therefore, it is critical to incorporate the impact of measurement errors into asset degradation modeling and reliability analysis.

In the reliability literature, most existing degradation models either ignore the LRD effect or measurement error. These models can generally be classified into three groups, i.e., general path models, stochastic process models, and artificial intelligence (AI) models. For the first group, Lu and Meeker [11] incorporated measurement errors into a random-effect general path model and studied fatigue crack growth. Si, et al. [38] developed a multivariate general path model to analyze dynamic material deformation by considering measurement errors. For more degradation studies using the general path model, one can refer to [39, 40]. To further capture the random behavior in a degradation path, various stochastic processes have been introduced to model asset degradations, including both Markovian and non-Markovian processes. Typical Markovian processes used for degradation modeling involve the gamma process [18, 41], the inverse Gaussian process [42, 43], and the Wiener process [44, 45]. On the basis of Markovian models, some researchers have further integrated measurement errors. For example, Whitmore [46] developed a fixed-effect Wiener process model subject to measurement errors to analyze the degradation of a transistor. Ye, et al.

[2] developed a random-effect Wiener process model with measurement errors to study the degradation of light emitting diodes. Limited research has been conducted on non-Markovian degradation modeling. For example, Zhou and Huang [47] developed an autoregressive integrated moving average (ARIMA) model to predict the remaining useful life of lithium-ion batteries. Although these non-Markovian processes can model the memory effect among degradation up to a limited order, they are not able to capture the LRD effect across the entire degradation path. Recently, some AI methods have also been developed for degradation analysis. For example, Kim, et al. [19] proposed a generic health index approach based on data fusion to study multi-sensor degradation data. Zhu, et al. [20] developed a multiscale convolutional neural network model for asset degradation analysis and remaining useful life prediction. Wang, et al. [21] modeled the degradation of turbo engines through a deep-learning-based data fusion approach. However, none of these methods can capture the LRD effect.

To track the LRD effect in degradation data, some researchers have adopted fractional Brownian motion (FBM) in asset degradation modeling. The memory structure of FBM is characterized by its Hurst parameter $H \in (0,1)$ [48]. When $0.5 < H < 1$, FBM demonstrates an LRD effect and therefore has recently been employed to study LRD -integrated degradation data of different assets. For instance, Xi, et al. [4] proposed a degradation model with LRD effect to predict the remaining useful life of turbo engines. Zhang, et al. [23] incorporated multiple degradation modes into an FBM-based degradation model. Si, et al. [5] considered the LRD effect in an accelerated degradation test. Zhang, et al. [6] developed an approximate explicit probability density function (PDF) of remaining useful life based on an LRD-integrated degradation model

with multiple hidden state variables. For more studies of FBM-based degradation models, one can refer to [30-32]. However, these LRD -integrated degradation models ignore measurement errors and therefore may result in imprecise lifetime predictions. It should be mentioned that Xi, et al. [49], in a conference paper, considered measurement errors in an FBM-based degradation model to analyze degradation data with a variant of the sigmoid trend. However, their model parameters were estimated via an approximate multi-step procedure that may lead to non-convergent results, and the random effects among degradation data that widely exist in practice were not considered in that paper.

To overcome the aforementioned challenges, in this chapter we propose a novel LRD -integrated degradation model by incorporating measurement errors. Specifically, both a fixed-effect scenario and a random-effect scenario of the proposed model are developed for asset degradation analysis. An exact maximum likelihood estimation (MLE) method is developed to estimate the model parameters. Based on the proposed model, reliability analysis and lifetime prediction are developed. Results of simulation and case studies illustrate that the conventional models, which ignore measurement errors, significantly bias the uncertainty of lifetime estimation.

The remaining structure of this chapter is summarized as follows. In Section 2.2, the novel LRD -integrated degradation model with measurement errors under both fixed-effect and random-effect scenarios is proposed, and the corresponding MLE approach for model parameter estimation is developed. In Section 2.3, the reliability analysis based on the proposed model is developed to calculate asset life distribution. In Section 2.4, simulation studies under various scenarios are implemented to verify the proposed model. In Section 2.5, a real case study using the capacity

degradation data of lithium-ion pouch cells is conducted to demonstrate the superiority of the proposed model over conventional degradation models. Section 2.6 provides the conclusion and outlines future research.

2.2 The Proposed Degradation Model

We propose an LRD -integrated degradation model with measurement errors for the degradation analysis of complex systems. First, a fixed-effect scenario of the proposed model is developed in Section 2.2.1. To capture the heterogeneity among degradation paths, a random-effect scenario of the proposed model is developed in Section 2.2.2. Three model assumptions are made in this chapter: 1) degradation paths demonstrate a monotonically increasing trend over time; 2) measurement errors follow a Gaussian distribution; and 3) the asset fails when its degradation level reaches a pre-specified threshold value. These assumptions have been widely made in the literature [2, 11, 38].

2.2.1 Fixed-Effect Scenario

2.2.1.1 Model Description

We start by considering the fixed-effect scenario, where all degradation paths are homogenous with a common trend term. Under this scenario, an FBM-based degradation model with measurement errors is proposed to capture both the LRD effect and the influence of measurement errors. Suppose there are K degradation paths collected from K degradation units, and the j th degradation path contains N_j degradation measurements. The proposed fixed-effect degradation model is

$$Y(t_{ij}) = \alpha f(t_{ij} | \boldsymbol{\eta}_f) + \sigma B_H(t_{ij}) + \epsilon_{ij}; \epsilon_{ij} \sim N(0, d^2), i \in 1, 2, \dots, N_j, j \in 1, 2, \dots, K \quad (1)$$

where t_{ij} is the time of the i th degradation measurement for the j th unit; $Y(t_{ij})$ is the corresponding degradation measurement at time t_{ij} ; $\alpha f(\bullet|\boldsymbol{\eta}_f)$ is a monotonic trend term with parameters α and $\boldsymbol{\eta}_f$; σ is a diffusion parameter; $B_H(\bullet)$ is the standard FBM with Hurst parameter $H \in (0,1)$; and ϵ_{ij} is the error of the i th degradation measurement for unit j , which is assumed to be normally distributed with a mean of zero and a variance of d^2 .

Specifically, in model (1), FBM (i.e., $B_H(\bullet)$) is a generalized Brownian motion (BM) to capture the memory effect defined as [48]

$$B_H(t) = B_H(0) + \frac{1}{\Gamma(H+1/2)} \left\{ \int_{-\infty}^0 \left[(t-s)^{H-1/2} - (-s)^{H-1/2} \right] dB(s) + \int_0^t (t-s)^{H-1/2} dB(s) \right\} \quad (2)$$

where $\Gamma(\bullet)$ is the gamma function, i.e., $\Gamma(x) = \int_0^\infty t^{x-1} e^{-t} dt$; and $B(\bullet)$ is a standard BM. FBM is a Gaussian process with a mean of zero and a covariance function as follows [50]:

$$\text{Cov}(B_H(t), B_H(s)) = \frac{1}{2} \left(|t|^{2H} + |s|^{2H} - |t-s|^{2H} \right) \quad (3)$$

Furthermore, FBM satisfies the following properties [48]: 1) $B_H(0) = 0$; 2) self-similar property, i.e., $B_H(|a|t) \sim |a|^H B_H(t)$; 3) property of stationary increments, i.e., $B_H(t) - B_H(s) \sim B_H(t-s)$ for $t > s$; and 4) sample paths of $B_H(t)$ are almost surely (a.s.) Hölder continuous of order less than H and are a.s. nowhere differentiable. Based on the value of H , FBM can be classified into three categories. When $0 < H < 0.5$, the increments of FBM are negatively correlated for non-overlapping time intervals, and the incremental process exhibits a short-range dependence memory effect; when $H = 0.5$, FBM degenerates into conventional BM with independent increments; and when $0.5 < H < 1$, the increments are positively correlated, and the incremental process exhibits the LRD effect. Therefore, FBM with $0.5 < H < 1$ has been widely applied to analyzing

degradation data with LRD effects in the reliability field [4, 6, 45].

2.2.1.2 Model Parameter Estimation

For the proposed model described in Section 2.2.1.1, we develop an MLE approach to estimate the model parameters $\boldsymbol{\eta} = (\boldsymbol{\eta}_f, \alpha, \sigma^2, H, d^2)^\top$, given the collection of degradation observations $\mathbf{Y} = \{\mathbf{Y}_1, \mathbf{Y}_2, \dots, \mathbf{Y}_K\}$, where $\mathbf{Y}_j = (Y(t_{1j}), Y(t_{2j}), \dots, Y(t_{N_jj}))^\top$ denotes the measurement collection of the j th degradation path. Let $\mathbf{f}_j = (f(t_{1j}|\boldsymbol{\eta}_f), f(t_{2j}|\boldsymbol{\eta}_f), \dots, f(t_{N_jj}|\boldsymbol{\eta}_f))^\top$; $\mathbf{B}_H^j = (B_H(t_{1j}), B_H(t_{2j}), \dots, B_H(t_{N_jj}))^\top$; and $\boldsymbol{\epsilon}_j = (\epsilon_{1j}, \epsilon_{2j}, \dots, \epsilon_{N_jj})^\top$. A vector form of the j th degradation path function can be written as

$$\mathbf{Y}_j = \alpha \mathbf{f}_j + \sigma \mathbf{B}_H^j + \boldsymbol{\epsilon}_j \quad (4)$$

Since FBM is a Gaussian process, \mathbf{B}_H^j follows a multivariate Gaussian distribution, i.e., $\mathbf{B}_H^j \sim MVN(\mathbf{0}, \boldsymbol{\Sigma}_j)$, where $\boldsymbol{\Sigma}_j$ is the covariance matrix that can be calculated via (3). As a result, \mathbf{Y}_j follows a multivariate Gaussian distribution, i.e., $\mathbf{Y}_j \sim MVN(\alpha \mathbf{f}_j, \mathbf{G}_j)$, where the (u, v) th entry of the covariance matrix \mathbf{G}_j is calculated as

$$(\mathbf{G}_j)_{uv} = \begin{cases} \frac{\sigma^2}{2} (t_{uj}^{2H} + t_{vj}^{2H} - |t_{uj} - t_{vj}|^{2H}) + d^2; & \text{for } u = v \\ \frac{\sigma^2}{2} (t_{uj}^{2H} + t_{vj}^{2H} - |t_{uj} - t_{vj}|^{2H}); & \text{for } u \neq v \end{cases} \quad (5)$$

where t_{uj} and t_{vj} represent the time epochs of the u th and v th degradation measurements of the j th unit, respectively. Therefore, the log-likelihood function given degradation path j is derived as

$$l_j(\boldsymbol{\eta} | \mathbf{Y}_j) = -\frac{N_j}{2} \ln(2\pi) - \frac{1}{2} \ln |\mathbf{G}_j| - \frac{1}{2} (\mathbf{Y}_j - \alpha \mathbf{f}_j)^\top \mathbf{G}_j^{-1} (\mathbf{Y}_j - \alpha \mathbf{f}_j) \quad (6)$$

On the basis of Equation (6), the overall log-likelihood function given the degradation data collection \mathbf{Y} can be developed as

$$l(\boldsymbol{\eta}|\mathbf{Y}) = -\ln(2\pi) \sum_{j=1}^K \frac{N_j}{2} - \frac{1}{2} \sum_{j=1}^K \ln|\mathbf{G}_j| - \frac{1}{2} \sum_{j=1}^K (\mathbf{Y}_j - \alpha \mathbf{f}_j)^\top \mathbf{G}_j^{-1} (\mathbf{Y}_j - \alpha \mathbf{f}_j) \quad (7)$$

The parameters $\boldsymbol{\eta}$ are estimated by maximizing the overall log-likelihood function with respect to the model parameters, i.e.,

$$\hat{\boldsymbol{\eta}} = \arg \max_{\boldsymbol{\eta}} \{l(\boldsymbol{\eta}|\mathbf{Y})\} \quad (8)$$

In addition to the point estimation of $\boldsymbol{\eta}$, we further develop an interval estimation method so that the confidence interval of $\boldsymbol{\eta}$ can be constructed. Based on the theory of MLE, the estimator $\hat{\boldsymbol{\eta}}$ follows an asymptotically normal distribution under a large sample size. Its covariance matrix \mathbf{S} is computed as the inverse of the observed Fisher information matrix $\mathbf{I}(\hat{\boldsymbol{\eta}})$, i.e., $\mathbf{S} = (\mathbf{I}(\hat{\boldsymbol{\eta}}))^{-1}$, where $\mathbf{I}(\hat{\boldsymbol{\eta}})$ can be calculated via [51]

$$\mathbf{I}(\hat{\boldsymbol{\eta}}) = - \left. \frac{\partial^2 l(\boldsymbol{\eta}|\mathbf{Y})}{\partial \boldsymbol{\eta} \partial \boldsymbol{\eta}^\top} \right|_{\boldsymbol{\eta}=\hat{\boldsymbol{\eta}}} \quad (9)$$

The square roots of the diagonal elements of the covariance matrix \mathbf{S} provide the standard errors of the corresponding estimators, i.e., $se(\hat{\eta}_i) = \sqrt{s_{ii}}$, where $\hat{\eta}_i$ is the i th element of $\hat{\boldsymbol{\eta}}$, and s_{mn} is the (m,n) th entry of the matrix \mathbf{S} . Therefore, the $100(1-\alpha)\%$ confidence interval of η_i (the i th element of $\boldsymbol{\eta}$) can be constructed as $(\hat{\eta}_i - z_{1-\alpha/2} \times se(\hat{\eta}_i), \hat{\eta}_i + z_{1-\alpha/2} \times se(\hat{\eta}_i))$, where z_x is the x -quantile of the standard normal distribution.

2.2.2 Random-Effect Scenario

2.2.2.1 Model Description

To further capture the heterogeneity among degradation paths of various units, a random-effect scenario of degradation model is developed in this section. In this scenario, the degradation parameter α is assumed to be random and follow a normal distribution to capture the

heterogeneity. This normality assumption to model the random effects of asset degradations has been widely adopted in the literature [2, 11]. Although the normality assumption can result in a sample of negative value of α , the issue can be neglected when the standard deviation is much lower than the mean of α . The proposed random-effect LRD -integrated degradation model with measurement errors is as follows:

$$Y(t_{ij}) = \alpha_j f(t_{ij} | \boldsymbol{\eta}_f) + \sigma B_H(t_{ij}) + \epsilon_{ij}; \epsilon_{ij} \sim N(0, d^2), \alpha_j \sim N(\mu_\alpha, s_\alpha^2), \quad (10)$$

$$i \in 1, 2, 3 \dots N_j, j \in 1, 2, 3 \dots K$$

where α_j is normally distributed with a mean of μ_α and a variance of s_α^2 as a random-effect parameter in the trend term of the j th degradation path. Notice that when $H = 0.5$, model (10) will degenerate into the conventional Wiener process-based degradation model with measurement errors [2].

2.2.2.2 Model Parameter Estimation

To estimate the parameters $\boldsymbol{\eta} = (\boldsymbol{\eta}_f, \mu_\alpha, s_\alpha^2, \sigma^2, H, d^2)^\top$ of the random-effect model, an MLE approach is developed given the degradation measurements $\mathbf{Y} = \{\mathbf{Y}_1, \mathbf{Y}_2, \dots, \mathbf{Y}_K\}$. Specifically, a vector form of \mathbf{Y}_j based on model (10) can be written as

$$\mathbf{Y}_j = \alpha_j \mathbf{f}_j + \sigma \mathbf{B}_H^j + \boldsymbol{\epsilon}_j; \alpha_j \sim N(\mu_\alpha, s_\alpha^2) \quad (11)$$

As α_j follows a Gaussian distribution, \mathbf{Y}_j follows a multivariate Gaussian distribution, denoted as $\mathbf{Y}_j \sim MVN(\mu_\alpha \mathbf{f}_j, \mathbf{Q}_j)$, where the (u, v) th entry of the covariance matrix \mathbf{Q}_j can be calculated by

$$(\mathbf{Q}_j)_{uv} = \begin{cases} f(t_{uj})f(t_{vj})s_\alpha^2 + \frac{\sigma^2}{2} (t_{uj}^{2H} + t_{vj}^{2H} - |t_{uj} - t_{vj}|^{2H}) + d^2; & \text{for } u = v \\ f(t_{uj})f(t_{vj})s_\alpha^2 + \frac{\sigma^2}{2} (t_{uj}^{2H} + t_{vj}^{2H} - |t_{uj} - t_{vj}|^{2H}); & \text{for } u \neq v \end{cases} \quad (12)$$

Given the degradation observations \mathbf{Y} , the overall log-likelihood function is derived as

$$l(\boldsymbol{\eta}|\mathbf{Y}) = -\ln(2\pi) \sum_{j=1}^K \frac{N_j}{2} - \frac{1}{2} \sum_{j=1}^K \ln|\mathbf{Q}_j| - \frac{1}{2} \sum_{j=1}^K (\mathbf{Y}_j - \mu_\alpha \mathbf{f}_j)^\top \mathbf{Q}_j^{-1} (\mathbf{Y}_j - \mu_\alpha \mathbf{f}_j) \quad (13)$$

The parameters of the random-effect model can be estimated as $\hat{\boldsymbol{\eta}} = \arg \max_{\boldsymbol{\eta}} \{l(\boldsymbol{\eta}|\mathbf{Y})\}$.

In numerous actual cases, asset degradations are measured under the same sampling scheme, i.e., all degradation paths share the same sampling time epochs. Under such a circumstance, the overall log-likelihood function (13) can be efficiently reduced. Suppose each degradation path contains N measurement points. Then \mathbf{Q}_j and \mathbf{f}_j will be identical across different units so that the subscript j can be removed. Therefore, the log-likelihood function in (13) can be written as

$$l(\boldsymbol{\eta}|\mathbf{Y}) = -\frac{KN}{2} \ln(2\pi) - \frac{K}{2} \ln|\mathbf{Q}| - \frac{1}{2} \sum_{j=1}^K (\mathbf{Y}_j - \mu_\alpha \mathbf{f})^\top \mathbf{Q}^{-1} (\mathbf{Y}_j - \mu_\alpha \mathbf{f}) \quad (14)$$

Based on (14), we calculate the partial derivatives of $l(\boldsymbol{\eta}|\mathbf{Y})$ with respect to parameters μ_α and s_α^2 , and set them to zero. Therefore, the estimators of parameters μ_α and s_α^2 are derived and summarized in Proposition 2.1. The proof of Proposition 2.1 is provided in Appendix A1.

Proposition 2.1. The MLE estimators of parameters μ_α and s_α^2 are as follows:

$$\hat{\mu}_\alpha = \frac{\sum_{j=1}^K \mathbf{Y}_j^\top \mathbf{C}^{-1} \mathbf{f}}{K \mathbf{f}^\top \mathbf{C}^{-1} \mathbf{f}} \quad (15)$$

$$\hat{s}_\alpha^2 = -\frac{1}{\mathbf{f}^\top \mathbf{C}^{-1} \mathbf{f}} + \frac{\sum_{j=1}^K (\mathbf{Y}_j^\top \mathbf{C}^{-1} \mathbf{f})^2}{K (\mathbf{f}^\top \mathbf{C}^{-1} \mathbf{f})^2} - \frac{\left(\sum_{j=1}^K \mathbf{Y}_j^\top \mathbf{C}^{-1} \mathbf{f} \right)^2}{(K \mathbf{f}^\top \mathbf{C}^{-1} \mathbf{f})^2} \quad (16)$$

where the (u,v) th entry of the matrix \mathbf{C} is

$$(\mathbf{C})_{uv} = \begin{cases} \frac{\sigma^2}{2} (t_u^{2H} + t_v^{2H} - |t_u - t_v|^{2H}) + d^2; & \text{for } u = v \\ \frac{\sigma^2}{2} (t_u^{2H} + t_v^{2H} - |t_u - t_v|^{2H}); & \text{for } u \neq v \end{cases} \quad (17)$$

where t_u and t_v are the time epochs of the u th and v th degradation measurements shared by all degradation paths when all units adopt the same sampling scheme, respectively, i.e.,

$$t_u = t_{u1} = t_{u2} \dots = t_{uK} \text{ and } t_v = t_{v1} = t_{v2} \dots = t_{vK}.$$

Let $\boldsymbol{\eta}^* = (\boldsymbol{\eta}_f, H, \sigma^2, d^2)^\top$ be the collection of other model parameters. By substituting $\widehat{\mu}_\alpha$ and \widehat{s}_α^2 into (14), the reduced log-likelihood function is obtained as

$$l(\boldsymbol{\eta}^* | \mathbf{Y}) = -\frac{1}{2}K - \frac{KN}{2} \ln(2\pi) - \frac{K}{2} \ln |\mathbf{C}| - \frac{K}{2} \ln \left(\frac{K \sum_{j=1}^K (\mathbf{f}^\top \mathbf{C}^{-1} \mathbf{Y}_j)^2 - \left(\sum_{j=1}^K \mathbf{Y}_j^\top \mathbf{C}^{-1} \mathbf{f} \right)^2}{K^2 (\mathbf{f}^\top \mathbf{C}^{-1} \mathbf{f})} \right) - \frac{1}{2} \sum_{j=1}^K \mathbf{Y}_j^\top \mathbf{C}^{-1} \mathbf{Y}_j + \frac{\sum_{j=1}^K (\mathbf{Y}_j^\top \mathbf{C}^{-1} \mathbf{f})^2}{2 \mathbf{f}^\top \mathbf{C}^{-1} \mathbf{f}} \quad (18)$$

In (18), the reduced log-likelihood is a function of parameters $\boldsymbol{\eta}^*$, which can be estimated as $\widehat{\boldsymbol{\eta}}^* = \arg \max_{\boldsymbol{\eta}^*} \{l(\boldsymbol{\eta}^* | \mathbf{Y})\}$. Subsequently, μ_α and s_α^2 can be calculated by substituting the estimated parameters $\widehat{\boldsymbol{\eta}}^* = (\widehat{\boldsymbol{\eta}}_f, \widehat{H}, \widehat{\sigma}^2, \widehat{d}^2)^\top$ into Equations (15) and (16), respectively.

To obtain an interval estimation of $\boldsymbol{\eta}^*$, the standard errors of parameters $\boldsymbol{\eta}_f$, H , σ^2 , and d^2 are calculated from the inverse of the Fisher information matrix with respect to the log-likelihood function (18). Subsequently, the standard errors of μ_α and s_α^2 are calculated based on Equations (15) and (16) using the Delta rule [51], which are summarized as

$$se(\hat{\mu}_\alpha) = \text{sqrt} \left(\begin{aligned} & \left(W_1 se(\hat{\sigma}^2) \right)^2 + \left(W_2 se(\hat{H}) \right)^2 + \left(W_3 se(\hat{d}^2) \right)^2 + \left(\frac{\partial \hat{\mu}_\alpha}{\partial \eta_{f1}} se(\hat{\eta}_{f1}) \right)^2 + \\ & \left(\frac{\partial \hat{\mu}_\alpha}{\partial \eta_{f2}} se(\hat{\eta}_{f2}) \right)^2 + \dots + \left(\frac{\partial \hat{\mu}_\alpha}{\partial \eta_{fn}} se(\hat{\eta}_{fn}) \right)^2 \end{aligned} \right) \quad (19)$$

$$se(\hat{s}_\alpha^2) = \text{sqrt} \left(\begin{aligned} & \left(W_4 se(\hat{\sigma}^2) \right)^2 + \left(W_5 se(\hat{H}) \right)^2 + \left(W_6 se(\hat{d}^2) \right)^2 + \left(\frac{\partial \hat{s}_\alpha^2}{\partial \eta_{f1}} se(\hat{\eta}_{f1}) \right)^2 + \\ & \left(\frac{\partial \hat{s}_\alpha^2}{\partial \eta_{f2}} se(\hat{\eta}_{f2}) \right)^2 + \dots + \left(\frac{\partial \hat{s}_\alpha^2}{\partial \eta_{fn}} se(\hat{\eta}_{fn}) \right)^2 \end{aligned} \right) \quad (20)$$

where $\boldsymbol{\eta}_f = (\eta_{f1}, \eta_{f2}, \dots, \eta_{fn})^T$, and the details of $W_1 \sim W_6$ are derived and provided in Appendix A2.

2.3 Reliability Analysis

Based on the proposed LRD-integrated degradation model with measurement errors, we develop a method of reliability analysis to obtain the asset lifetime distribution given the estimated parameters $\hat{\boldsymbol{\eta}}$. The failure time T_f of an asset is assumed to be the first passage time when its underlying degradation level goes beyond a pre-determined degradation threshold value y_{th} , i.e.,

$$T_f = \inf \{ t | Y_u(t | \boldsymbol{\eta}) \geq y_{th} \} \quad (21)$$

where $Y_u(t | \boldsymbol{\eta})$ is the underlying degradation level, and $Y(t | \boldsymbol{\eta}) = Y_u(t | \boldsymbol{\eta}) + \varepsilon(t)$. Due to the complexity of the proposed model, the closed-form lifetime distribution is not available in most situations. To overcome this difficulty, a Monte Carlo (MC) approach is developed to calculate the lifetime distribution. Details of the MC method are summarized in Algorithm 2.1.

Algorithm 2.1. A Monte Carlo approach to calculate the asset lifetime distribution

Step 1. Obtain the point estimates $\hat{\boldsymbol{\eta}}$ of model parameters via the MLE method in Section 2.2.

Step 2. For $j = 1 \sim L$, simulate the j th underlying degradation path (i.e., \mathbf{Y}_u^j) using $\hat{\boldsymbol{\eta}}$ (L is sufficiently large):

2.1 Simulate the j th trend term: for the fixed-effect scenario, $\alpha = \hat{\alpha}$; for the random-effect

scenario, $\hat{\alpha}_j \sim N\left(\hat{\mu}_\alpha, \hat{s}_\alpha^2\right)$; and \mathbf{f}_j is simulated based on parameters $\hat{\boldsymbol{\eta}}_j$.

2.2 Simulate the j th FBM term \mathbf{B}_H^j using a fast Fourier transformation (FFT) method [52].

2.3 Obtain \mathbf{Y}_u^j of the fixed-effect and random-effect scenarios, respectively, as follows:

$$\mathbf{Y}_u^j = \hat{\alpha}\mathbf{f}_j + \hat{\sigma}\mathbf{B}_H^j \quad \text{and} \quad \mathbf{Y}_u^j = \hat{\alpha}_j\mathbf{f}_j + \hat{\sigma}\mathbf{B}_H^j,$$

Step 3. Calculate the lifetime distribution:

3.1 For $j = 1 \sim L$, calculate the j th failure time using Equation (21), denoted as T_f^j .

3.2 Calculate the lifetime distribution as $F(t|\hat{\boldsymbol{\eta}}) = L^{-1} \sum_{j=1}^L I_t(T_f^j)$, where

$$I_t(T_f^j) = \begin{cases} 1; & \text{if } T_f^j \leq t \\ 0; & \text{otherwise} \end{cases}.$$

More specifically, in Step 2.2 of Algorithm 2.1, the FFT method is applied to simulating \mathbf{B}_H^j . In the literature, there are three major approaches to simulate a path of the FBM, i.e., Hosking method [53], Cholesky method [54], and FFT method. Among them, the FFT method has the lowest computational complexity of $O(n \log(n))$ for simulating a discretized FBM of length n , while the computational complexity of the Hosking and Cholesky methods are $O(n^3)$ and $O(n^2)$, respectively [55].

2.4 Simulation Study

To evaluate the performance of the proposed model and the corresponding MLE approach

for parameter estimation, we implement simulation studies under both fixed-effect and random-effect scenarios. The fixed-effect model and the random-effect model are assessed in Section 2.4.1 and Section 2.4.2, respectively.

2.4.1 Fixed-Effect Model

2.4.1.1 Data Simulation

For illustration purposes, a linear trend term is selected in the degradation modeling as the degradation or transformed degradation of numerous assets exhibits a linear trend [2, 46]. The degradation paths are simulated using the following fixed-effect LRD-integrated model with measurement errors:

$$P_1 : Y(t) = \alpha t + \sigma B_H(t) + \epsilon; \epsilon \sim N(0, d^2) \quad (22)$$

The model parameters $\boldsymbol{\eta} = (H, \sigma^2, \alpha, d^2)^\top$ are specified as $(0.8, 1, 4, 0.1)^\top$, and the number of generated degradation paths is set at $K=10$. Each degradation path contains $N_j=100$ measurements that are equally spaced in a time interval $[0, 30]$. The simulated degradation paths are shown in Figure 2.1.

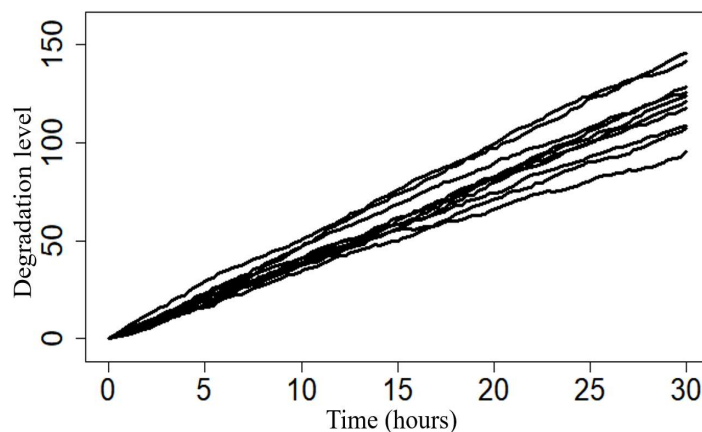


Figure 2.1. Simulated degradation paths using model P_1

2.4.1.2 Parameter Estimation

The simulated degradation paths shown in Figure 2.1 are then analyzed using the fixed-effect model P_1 . The model parameters $\boldsymbol{\eta}$ and corresponding standard errors are estimated through Equations (8) and (9), which are listed in Table. 2-1. Note that the point estimates of the model parameters are close to the pre-specified values, which demonstrates that the proposed MLE method performs well under the current sample size.

Table 2-1. Point Estimates and Standard Errors of P_1 Parameters

Parameter	Point Estimate	Standard Error
H	0.809	0.0363
σ^2	0.862	0.116
α	4.04	0.152
d^2	0.107	8.69×10^{-3}

To further evaluate the performance of the proposed MLE method, we repeat the simulation process for $M = 1000$ times under different sample sizes, i.e., $K = 10, 20,$ and 50 . The root mean square errors (RMSEs) of the parameter estimation are calculated as $RMSE(\hat{\eta}_i) = \text{sqr}t\left(\frac{1}{M} \sum_{l=1}^M (\eta_i - \hat{\eta}_{i,l})^2\right)$, where $\hat{\eta}_{i,l}$ is the estimate of parameter η_i in the l th iteration, and results are summarized in Table 2-2. It can be observed that the RMSEs are generally small. As the sample size increases, the RMSEs of the parameter estimation all decrease, which demonstrates the efficiency of the MLE approach.

Table 2-2. RMSEs of Parameter Estimation of P_1 under Different Sample Sizes

Sample Size (K)	10	30	50
$RMSE(\hat{H})$	0.0395	0.0213	0.0165
$RMSE(\hat{\sigma}^2)$	0.132	0.0715	0.0564
$RMSE(\hat{\alpha})$	0.162	0.0918	0.0719
$RMSE(\hat{d}^2)$	9.20×10^{-3}	5.16×10^{-3}	3.88×10^{-3}

2.4.1.3 Model Comparison

To illustrate the advantage of the proposed fixed-effect model P_1 , a model comparison is conducted between P_1 and a conventional LRD-integrated fixed-effect degradation model (P_2) that ignores measurement errors:

$$P_2: Y(t) = \alpha t + \sigma B_H(t) \quad (23)$$

where P_2 depends on three parameters $\boldsymbol{\eta} = (H, \sigma^2, \alpha)^T$. Model P_2 is applied to studying the simulated degradation data in Figure 2.1. Point estimates of the model parameters and corresponding standard errors are summarized in Table 2-3.

Table 2-3. Point Estimates and Standard Errors of P_2 Parameters

Parameter	Point Estimate	Standard Error
H	0.526	0.0150
σ^2	1.20	0.0704
α	4.05	0.0690

Based on the estimated parameters of P_1 and P_2 , the PDFs of the predicted lifetime using these two models are computed following Algorithm 2.1, where the failure threshold value is specified as $y_{th} = 150$. The predicted lifetime distributions along with a histogram of the true lifetime are presented in Figure 2.2. Note that the histogram of the true lifetime is obtained based on the

true/pre-specified parameter values of model P_1 .

In addition, the means and standard deviations of the predicted lifetime distributions of P_1 and P_2 are calculated. The means of lifetime are 37.52 and 37.07 for P_1 and P_2 , respectively, and the standard deviations are 4.41 and 1.82, respectively. It can be seen that the mean values are relatively close, while the conventional model P_2 significantly underestimates the uncertainty of asset lifetime. Therefore, it is critical to consider measurement errors in LRD-integrated degradation modeling.

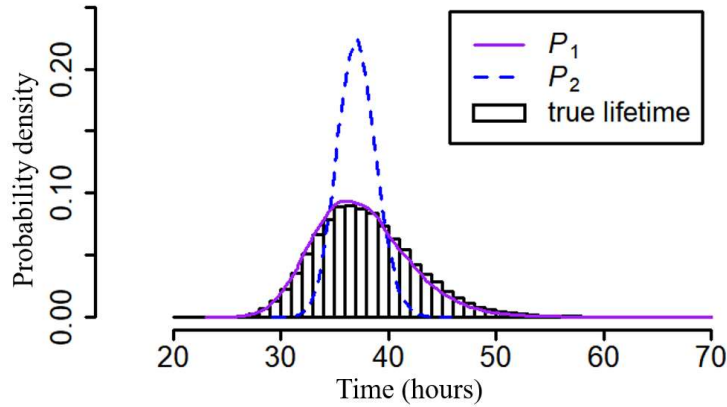


Figure 2.2. PDFs of predicted lifetime using P_1 and P_2

2.4.2 Random-Effect Model

2.4.2.1 Data Simulation

For some assets, the degradation may demonstrate heterogeneities among different units. To capture such heterogeneities, we consider a random-effect LRD-integrated degradation model with measurement errors as follows:

$$P_3 : Y(t) = \alpha t^\beta + \sigma B_H(t) + \epsilon; \alpha \sim N(\mu_\alpha, s_\alpha^2), \epsilon \sim N(0, d^2) \quad (24)$$

Specifically, a power law trend term is employed in the degradation model, which has been widely

used in the reliability literature [2, 56]. The model parameters of P_3 are $\boldsymbol{\eta} = (H, \sigma^2, d^2, \mu_\alpha, s_\alpha^2, \beta)^T$.

To simulate degradation paths using P_3 , the model parameters are designated as $\boldsymbol{\eta} = (0.85, 0.5, 0.05, 5, 1, 0.7)^T$. Based on this parameter setting, we simulate $K=10$ degradation paths, and each path contains $N_j=100$ measurements that are equally distributed in a time interval $[0, 50]$. The simulated degradation paths are illustrated in Figure 2.3.

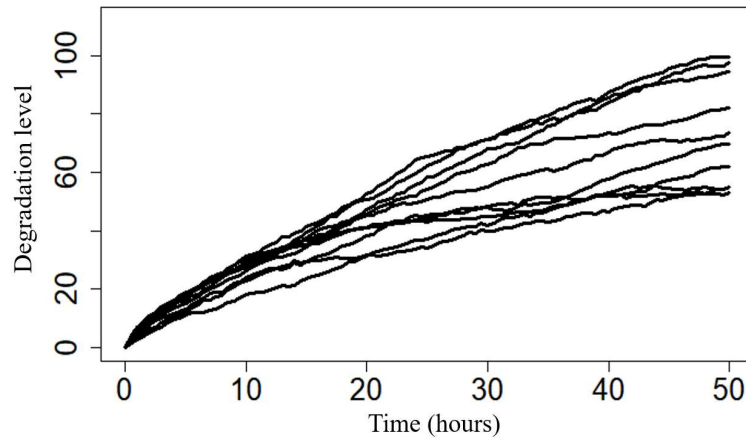


Figure 2.3 Simulated degradation paths using model P_3

2.4.2.2 Parameter Estimation

We apply the proposed random-effect model to analyzing the simulated degradation paths in Figure 2.3. The model parameters $\boldsymbol{\eta}$ and the corresponding standard errors are estimated using the MLE method developed in Section 2.2.2.2, which are summarized in Table. 2-4.

Table 2-4. Point Estimates and Standard Errors of P3 Parameters

Parameter	Point Estimate	Standard Error
H	0.833	0.0370
σ^2	0.469	0.0652
d^2	0.0491	5.46×10^{-3}
μ_α	4.82	0.0213
s_α^2	0.671	0.105
β	0.709	0.0148

To examine the performance of the proposed MLE approach for parameter estimation, a

RMSE test is also conducted under different sample sizes. We repeat the simulation process in Section 2.4.2.1 for $M=1000$ times, and the sample sizes are specified as $K = 10, 30,$ and 50 . Table 2-5 summarizes the calculated RMSEs of parameter estimates of P_3 . It can be seen that the RMSEs are generally small and decrease as the sample size increases, which demonstrates a good performance of the proposed MLE approach.

Table 2-5. RMSEs of Parameter Estimation of P_3 under Different Sample Sizes

Sample Size (K)	10	30	50
$RMSE\left(\widehat{H}\right)$	0.0393	0.0229	0.0160
$RMSE\left(\widehat{\sigma}^2\right)$	0.0826	0.0531	0.0347
$RMSE\left(\widehat{d}^2\right)$	5.58×10^{-3}	3.21×10^{-3}	2.43×10^{-3}
$RMSE\left(\widehat{\mu}_\alpha\right)$	0.376	0.211	0.163
$RMSE\left(\widehat{s}_\alpha^2\right)$	0.593	0.373	0.296
$RMSE\left(\widehat{\beta}\right)$	1.62×10^{-2}	9.06×10^{-3}	7.50×10^{-3}

2.4.2.3 Model Comparison

To demonstrate the superiority of the proposed random-effect model P_3 , we compare it with an LRD-integrated random-effect model without considering the measurement errors as follows:

$$P_4: Y(t) = \alpha t^\beta + \sigma B_H(t); \alpha \sim N(\mu_\alpha, s_\alpha^2) \quad (25)$$

where the parameters of model P_4 are $\boldsymbol{\eta} = (H, \sigma^2, \mu_\alpha, s_\alpha^2, \beta)^\top$. The model P_4 is applied to studying the simulated degradation paths in Figure 2.3. Point estimates of $\boldsymbol{\eta}$ and corresponding standard errors are computed and listed in Table 2-6.

Table 2-6. Point Estimates and Standard Errors of P_4 Parameters

Parameter	Point Estimate	Standard Error
H	0.601	0.0182
σ^2	0.519	0.0305
μ_α	4.93	0.336
s_α^2	0.765	0.424
β	0.697	0.0111

On the basis of the estimated parameters of models P_3 and P_4 , the lifetime distributions of both models are calculated using Algorithm 2.1 with a failure threshold value specified as $y_{th} = 100$. The predicted lifetime distributions along with the histogram of the true lifetime are illustrated in Figure 2.4. Furthermore, we compute the means and standard deviations of the predicted lifetime distributions of P_3 and P_4 . The means of P_3 and P_4 are 88.63 and 83.15, respectively, and the standard deviations are 70.14 and 30.43, respectively. Similarly, results reveal that the means are relatively close for these two models, whereas the conventional model P_4 , which ignores measurement errors, significantly misestimates the lifetime uncertainty. This also demonstrates the necessity of incorporating measurement errors into the LRD-integrated degradation model.

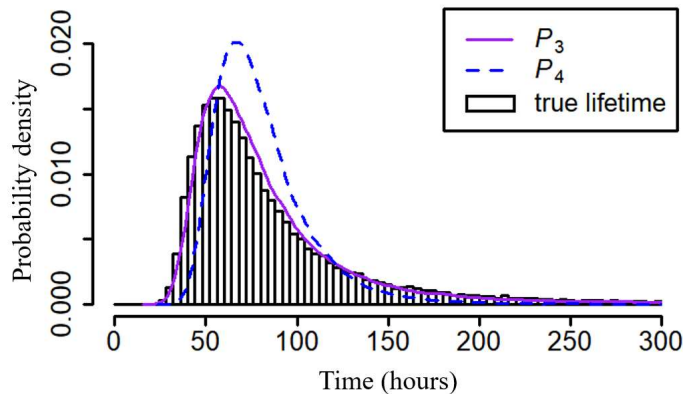


Figure 2.4. Predicted lifetime distributions using P_3 and P_4

2.5 Case Study

To further verify the proposed model, we conduct a real case study based on the degradation data of lithium-ion pouch cells. Section 2.5.1 briefly describes the dataset, Section 2.5.2 provides the estimation results of model parameters, and Section 2.5.3 performs comparisons between the proposed model and conventional models.

2.5.1 Case Data Description

A publicly accessible dataset on the capacity degradation of eight Kokam 740 mAh lithium-ion pouch cells is applied to validating the performance of the proposed model [57]. The capacity degradation of these cells was measured via an aging experiment, which was conducted in a thermal chamber at 40°C under predetermined stress cycles. Each stress cycle consisted of a constant-current-constant-voltage charging process and a discharging process based on the urban Artemis profile. The capacities of the cells were periodically measured with a time interval of 100 cycles via a pseudo open-circuit voltage discharging method (i.e., discharging cells under a current of 40 mA). Figure 2.5 illustrates the eight capacity degradation paths of the cells (notice that eight outliers have been removed from the 511 measurements in total).

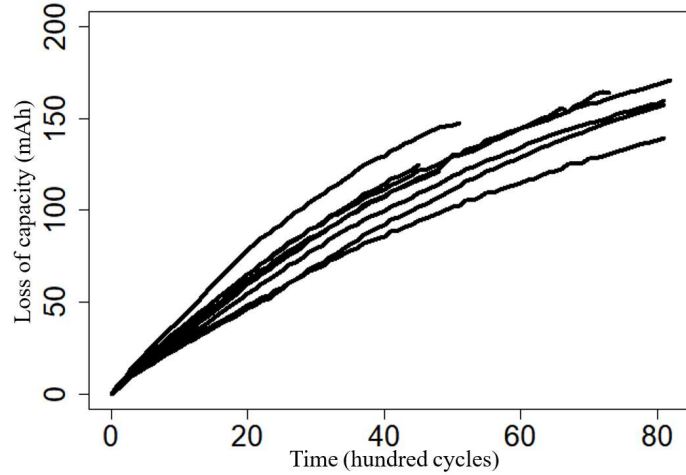


Figure 2.5. Degradation paths of eight Kokam 740 mAh lithium-ion pouch cells (loss of capacity vs. degradation cycle)

2.5.2 Parameter Estimation

We apply the proposed model to studying the cell degradation data in Figure 2.5. Since these degradation paths demonstrate an approximate power law trend, a power law function is selected to model the trend term of degradation. Therefore, the proposed models under the fixed-effect and random-effect scenarios are constructed, respectively, as follows:

$$P_5: Y(t) = \alpha t^\beta + \sigma B_H(t) + \epsilon; \epsilon \sim N(0, d^2) \quad (26)$$

$$P_6: Y(t) = \alpha t^\beta + \sigma B_H(t) + \epsilon; \alpha \sim N(\mu_\alpha, s_\alpha^2), \epsilon \sim N(0, d^2) \quad (27)$$

Parameters of the fixed-effect model P_5 and random-effect model P_6 are $\boldsymbol{\eta} = (H, \sigma^2, d^2, \beta, \alpha)^T$ and $\boldsymbol{\eta} = (H, \sigma^2, d^2, \beta, \mu_\alpha, s_\alpha^2)^T$, respectively. Given the degradation measurements shown in Figure 2.5, the parameters and corresponding standard errors of models P_5 and P_6 are calculated using the MLE approach in Sections 2.2.1.2 and 2.2.2.2, respectively, which are listed in Table 2-7. It can be observed from Table 2-7 that the standard deviation of α (i.e., 0.170) is much lower than the mean value of α (i.e., 4.63) using the proposed random-effect model P_6 . This justifies

the normality assumption made earlier in Section 2.2.2.1. Similar observations can also be made from Table. 2-4 in the simulation study.

Table 2-7. Point Estimates and Standard Errors of P_5 and P_6 Parameters

P_5			P_6		
η	Point Estimate	Standard Error	η	Point Estimate	Standard Error
H	0.967	0.0179	H	0.964	0.0196
σ^2	0.451	0.205	σ^2	0.638	0.136
d^2	0.166	0.0139	d^2	0.177	0.0150
β	0.836	0.0135	β	0.839	0.0129
α	4.61	0.254	μ_α	4.63	0.254
	—		s_α^2	0.170	0.868

2.5.3 Model Comparison

To demonstrate the superiority of the proposed model, a comparison with conventional models that ignore measurement errors is conducted. The following models P_7 and P_8 denote the conventional fixed-effect and random-effect models, respectively:

$$P_7: Y(t) = \alpha t^\beta + \sigma B_H(t) \quad (28)$$

$$P_8: Y(t) = \alpha t^\beta + \sigma B_H(t); \alpha \sim N(\mu_\alpha, s_\alpha^2) \quad (29)$$

The model parameters of P_7 and P_8 are $\eta = (H, \sigma^2, \beta, \alpha)^\top$ and $\eta = (H, \sigma^2, \beta, \mu_\alpha, s_\alpha^2)^\top$, respectively. Models P_7 and P_8 are then applied to analyzing the degradation data of pouch cells shown in Figure 2.5. Parameters and corresponding standard errors of P_7 and P_8 are computed via the MLE approach and are summarized in Table 2-8.

Table 2-8. Point Estimates and Standard Errors of P_7 and P_8 Parameters

P_7			P_8		
η	Point Estimate	Standard Error	η	Point Estimate	Standard Error
H	0.624	0.0212	H	0.564	0.0254
σ^2	0.574	0.0371	σ^2	0.529	0.0340
β	0.813	0.0116	β	0.812	0.0103
α	4.86	0.231	μ_α	4.94	0.286
	—		s_α^2	0.301	0.184

For reliability analysis of the pouch cells, we specify the failure threshold value as $y_{th} = 150$ mAh, i.e., the failure occurs when the loss of capacity reaches 150 mAh. Based on the estimated model parameters, the predicted lifetime distributions of models $P_5 \sim P_8$ are calculated using Algorithm 2.1. Figures 2.6 and 2.7 illustrate PDFs of the predicted lifetime using the proposed model and the conventional model under the fixed-effect and random-effect scenarios, respectively. It is observed that the conventional model that ignores measurement errors significantly biases the uncertainty of the lifetime estimation under both scenarios, which is consistent with the results of simulation studies discussed in Section 2.4.

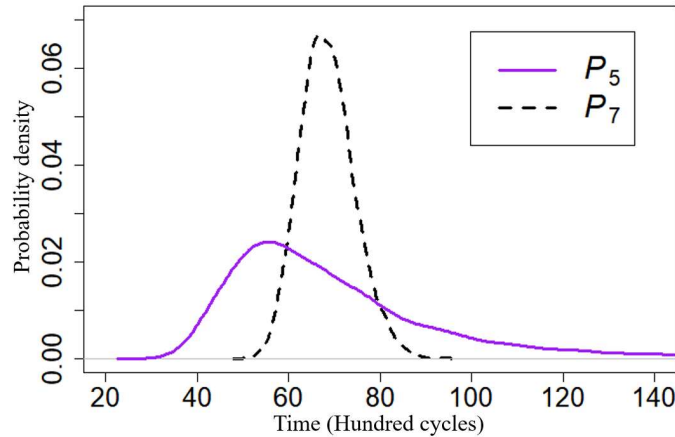


Figure 2.6. PDFs of predicted lifetime using models P_5 and P_7

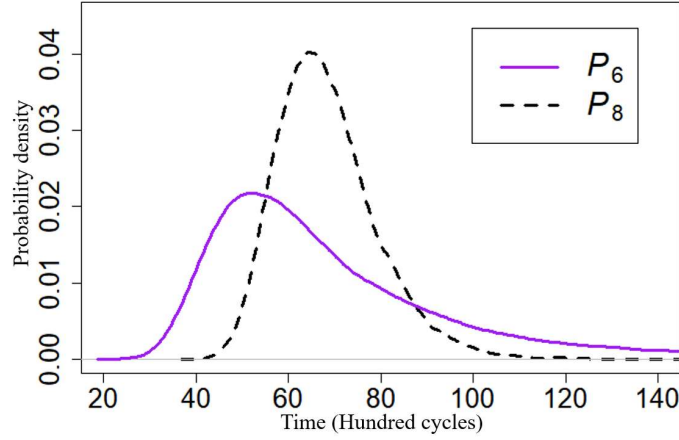


Figure 2.7. PDFs of predicted lifetime using models P_6 and P_8

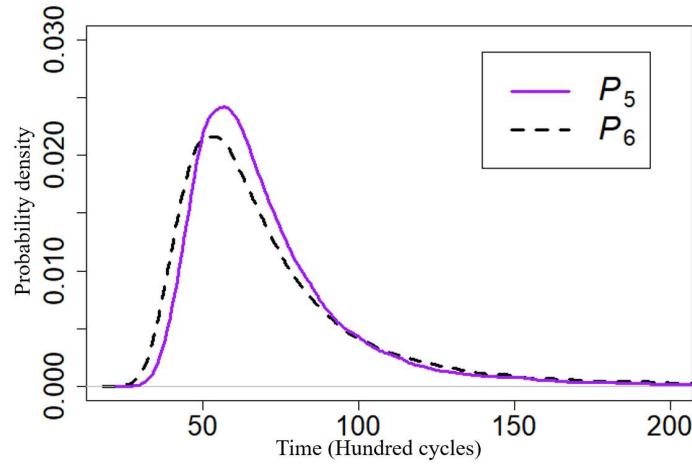


Figure 2.8. PDFs of predicted lifetime using models P_5 and P_6

In addition to the conventional LRD-integrated degradation models, we further compare the proposed model with a conventional BM-based random-effect degradation model with measurement errors in [2], which does not consider the LRD effect. The BM-based model is

$$P_B: Y(t) = \alpha t^\beta + \sigma B(t) + \epsilon; \alpha \sim N(\mu_\alpha, s_\alpha^2), \epsilon \sim N(0, d^2) \quad (30)$$

where $B(t)$ is the standard BM. The model parameters of P_B are $\boldsymbol{\eta} = (\sigma^2, d^2, \beta, \mu_\alpha, s_\alpha^2)^\top$, which are estimated using the Li-ion pouch cell degradation data in Figure 2.5 by an MLE approach and summarized in Table 2-9.

Table 2-9. Point Estimates and Standard Errors of P_B Parameters

Parameter	Point Estimate	Standard Error
σ^2	0.690	0.0358
d^2	0.0271	0.0212
β	0.806	0.00840
μ_α	5.06	0.270
s_α^2	0.578	0.156

Based on the estimated parameters of model P_B , the predicted lifetime distribution is computed. Figure 2.9 shows PDFs of the predicted lifetime calculated by models P_6 and P_B . It can be observed that the conventional BM-based degradation model, P_B , which ignores the LRD effect, underestimates the lifetime uncertainty.

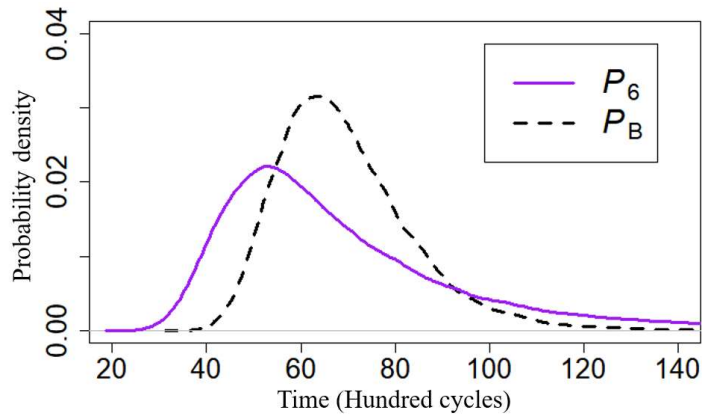


Figure 2.9. PDFs of predicted lifetime calculated by models P_6 and P_B

To further compare the performances of models $P_5 \sim P_8$ and P_B , the means of life prediction, standard deviations of life prediction, and Bayesian information criterions (BICs) are calculated and listed in Table 2-10. It is observed that the means of these five models are relatively close, while the standard deviations of models P_7 and P_8 are significantly smaller than those of models P_5 and P_6 , respectively. This indicates that the conventional models P_7 and P_8 , without

considering measurement errors, significantly underestimate the uncertainty of the lifetime estimation. Moreover, model P_B , which ignores the LRD effect, also significantly underestimates the life uncertainty. In addition, the proposed models have significantly smaller BICs than conventional models, which also demonstrates the superiority of the proposed models. It can be seen that the predicted lifetime distributions using models P_5 and P_6 , as shown in Figure 2.8, are similar, and their BICs are relatively close. This indicates a similar performance between P_5 and P_6 in analyzing the capacity degradation of the lithium-ion pouch cells. That is, for the lithium-ion pouch cell data the better fit attained by introducing heterogeneity as in model P_6 does not improve the performance in terms of BIC.

Table 2-10. Life Means, Standard deviations, and BICs of $P_5 \sim P_8$ and P_B

Model Index	Mean	Standard Deviation	BIC
P_5	69.85	29.36	1071.894
P_6	69.74	35.38	1077.301
P_7	68.42	5.990	1184.579
P_8	68.18	10.68	1177.271
P_B	69.62	14.92	1182.508

In addition, we also consider the random effect of more parameters in the proposed model. Besides the normality assumption on parameter α , parameters σ^2 and d^2 are further assumed to follow gamma distributions to guarantee the non-negativity. This random-effect model is summarized as

$$\begin{aligned}
 P_R : Y(t) &= \alpha t^\beta + \sigma B_H(t) + \epsilon; \alpha \sim N(\mu_\alpha, s_\alpha^2), \epsilon \sim N(0, d^2) \\
 \sigma^2 &\sim \text{Gamma}(k_{\sigma^2}, \theta_{\sigma^2}), d^2 \sim \text{Gamma}(k_{d^2}, \theta_{d^2})
 \end{aligned} \tag{31}$$

where k_{σ^2} and θ_{σ^2} are the shape and scale parameters of σ^2 , respectively; k_{d^2} and θ_{d^2} are the shape and scale parameters of d^2 , respectively; and the model parameters are

$\boldsymbol{\eta} = (H, \beta, \mu_\alpha, s_\alpha^2, k_{\sigma^2}, \theta_{\sigma^2}, k_{d^2}, \theta_{d^2})^T$. Based on an MLE approach, $\boldsymbol{\eta}$ is estimated and summarized in Table 2-11.

Table 2-11. Point Estimates and Standard Errors of P_R Parameters

Parameter	Point Estimate	Standard Error
H	0.895	0.0138
β	0.816	0.00727
μ_α	4.68	0.185
s_α^2	0.348	0.156
k_{σ^2}	2.74	1.42
θ_{σ^2}	0.154	0.0939
k_{d^2}	2.52	1.62
θ_{d^2}	0.110	0.0876

To compare the proposed random-effect model P_6 with model P_R , the BIC of model P_R is computed as 1081.152, which is slightly larger than the BIC of P_6 (i.e., 1077.301). Therefore, model P_6 performs slightly better than model P_R . This result indicates that considering the random effect of more parameters does not improve the performance of the proposed model in terms of BIC. This is due to the fact that although P_R is more general, it introduces several additional parameters that are penalized in the BIC.

2.6 Conclusion

The long-range dependence effect has recently been detected in the degradation process of various assets. Most existing LRD-integrated degradation studies have ignored measurement errors, which may result in a biased reliability estimation and life prediction. In this chapter, we propose a novel LRD-integrated degradation model by incorporating measurement errors under both fixed-effect and random-effect scenarios. A maximum likelihood estimation method is developed for the model parameter estimation. Based on the model and estimated parameters, asset

reliability analysis is developed to compute the lifetime distribution of assets. Simulation studies are implemented to evaluate the performance of the proposed model, and a real case study on the capacity degradation of lithium-ion pouch cells is conducted to validate the proposed model. Results reveal that the conventional LRD-integrated models, which neglect the measurement errors, significantly misestimate asset life uncertainty, while the proposed model provides more accurate life estimations.

CHAPTER 3

RELIABILITY ANALYSIS CONSIDERING THE LRD EFFECT UNDER ACCELERATED CONDITIONS

3.1 Introduction

Under normal use conditions/stresses, many modern engineering assets such as aircraft engines, advanced electronic modules and mechanical devices are highly reliable and would not fail in several months or years. To accelerate the life testing process under finite time resources, testing stresses in excess of the normal use conditions are applied to accelerate the asset degradation and failure, the basis on which asset reliability (life) information under normal stresses can be inferred in a short period of time [58]. Common examples of accelerating stresses include temperature, voltage, pressure, humidity, vibration amplitude, mechanical force, user rate, etc. [59, 60]. On the basis of data observation types, accelerated testing methods can be broadly classified into accelerated life testing (ALT) [61, 62] and accelerated degradation testing (ADT) [63, 64]. Specifically, in an ALT the time-to-failure data [65] of assets are observed, while in an ADT the detailed degradation paths [66] are monitored. As a result, data from an ADT often contain richer information that can be leveraged for asset reliability evaluation. Moreover, ADT is more suitable for highly reliable products as often limited failures of such products can be observed during a finite test period of time [67].

Recently, it has been shown that degradation data of some assets demonstrate a long-range dependence (LRD) effect, i.e., the asset degradations are significantly correlated across a long period of time. In this type of degradation process, the future degradation evolution heavily depends on both the current degradation state and past degradation history, and the increments of

degradation for non-overlapping time intervals are highly correlated. For example, in material crack propagation, the future crack growth rate and direction often highly depend on the historical crack propagation paths, including the physical mode of crack initiation and the geometrical path of the past crack evolution. Another example is on the degradation of an automotive transmission system when a car has experienced two different road conditions in sequence, i.e., good and bad. Both the road surface roughness and historical passing order through the two road conditions will affect the health status of the transmission system, thereby impacting its future degradation process. In the literature, the LRD effect has been observed and researched in the performance degradation of various engineering assets, e.g., Lithium-ion batteries, turbofan engines, ball bearings and blast furnaces [4, 7, 68-70]. Researchers have applied the FBM theory to study the LRD effects in the degradation data and developed several degradation-based asset remaining life predictions. It is worth mentioning that the FBM is different from Bayesian filtering approaches (such as Kalman filtering [71] and Particle filtering [49] methods) in capturing memory effects among degradation data. The filtering-based methods focus on dynamically updating degradation parameters and remaining useful life with the utilization of newly monitored degradation data and thus can capture memory effects to a certain extent. In contrast, the FBM can fundamentally capture long-range dependence across the whole range of a static degradation path. In addition to engineering degradation data, the long-range dependence have also been widely monitored and studied in finance (e.g., stock price and asset return) [72], geophysics (e.g., climatology and hydrology) [73], biology (e.g., DNA sequence, telomere subdiffusion) [74] and telecommunication (e.g., internet traffic and connectionless network) [75].

In fact, a major driven factor for the recent observation of LRD effects in the reliability field is the advancement of sensor technologies that enable a real-time monitoring of asset performance degradation with fast data acquisition rates. In most traditional degradation tests, only a limited number or length of reliability data can be obtained, e.g., a few sparsely sampled performance degradation paths. These data are not “long” and “dense” enough for an observation of the LRD, and thus Markovian assumptions have been widely imposed in literature to ignore the LRD effects. In contrast, when long and dense performance degradation data are frequently acquired in the coming era of “Data Revolution”, e.g., hundreds or thousands of data points per degradation path for multiple paths of asset performance degradation tested at multi-level accelerated stresses, long-term and higher-order correlations among the data can no longer be ignored.

In the existing ADT research, asset degradations are often modeled using general degradation path functions, Markovian stochastic processes or nonparametric methods without considering any LRD effects. The general degradation path method is proposed by Meeker, et al. [39] and models the ADT data using stress adjusted parametric path functions. Common approaches of stress adjustment (i.e., incorporating the stress effect into an ADT) include the Arrhenius relationship [76], Eyring relationship [77] and generalized Eyring relationship [78] used for elevated temperature acceleration, the Inverse power law relationship [79] used for elevated voltage or pressure acceleration, and several empirical relationships [59] for a joint acceleration of temperature-voltage, temperature-humidity and temperature-current density, etc. Although these general path methods have been widely applied, one limitation is that they are not efficient enough

to characterize the stochastic behavior and uncertainty of asset degradation processes. To better capture the stochastic effect, some researchers studied ADT data using Markovian stochastic processes such as Wiener process [16], geometric Brownian motion [17], Gamma process [18] and Inverse Gaussian process [22]. However, these methods assume that the future degradation of assets only depends on the current degradation state without impacts of historical degradation, and the degradation increments are independent for non-overlapping time intervals. In addition to the aforementioned parametric modeling of ADT data, several semi-parametric or nonparametric methods are developed for more flexible degradation path modeling [80, 81]. However, to our best knowledge none of the existing ADT research considers the LRD effect. Without incorporating such effect, the reliability testing result (i.e., lifetime estimation under normal stresses) could be biased, and the lifetime uncertainty quantification can be inaccurate, which may subsequently incur problematic product life design and higher operational/maintenance cost.

To overcome the aforementioned challenge, we propose a novel ADT model by integrating the LRD effect in asset degradation processes. Specifically, a stress adjusted Fractional Brownian Motion (FBM) with drifts is proposed to model the accelerated degradation processes, which can effectively capture the LRD effect. The model incorporates the widely used Wiener-process based ADT as a special case. A maximum likelihood estimation (MLE) approach is developed to estimate the model parameters. Based on the proposed model, a likelihood-ratio hypothesis test is developed to test the existence of the long-range dependence. To illustrate the developed methods, both simulation studies and physical experiments are conducted. Results show that the traditional ADT paradigm significantly underestimates lifetime uncertainty without

considering the LRD effects, while the proposed ADT framework fundamentally improves life testing accuracy.

The remainder of this chapter is summarized as follows. In Section 3.2, we propose the ADT model that integrates the LRD effect. In Section 3.3, we develop an MLE method for the model parameter estimation. Based on the proposed model with parameter estimation, in Section 3.4 we design a likelihood-ratio hypothesis test to examine whether an LRD effect exists. In Section 3.5, simulation studies are implemented to illustrate the developed methods. In Section 3.6, a physical experiment on an ADT of a photocatalyst (Pt/black TiO₂) is conducted to demonstrate and validate the proposed model. Section 3.7 concludes the chapter and outlines some future work.

3.2 Statistical Model

We propose a novel ADT model by incorporating the LRD effect in asset degradation processes. Section 3.2.1 briefly introduces the LRD effect, Section 3.2.2 presents the proposed ADT modeling with long-range dependence, and Section 3.2.4 develops the asset lifetime prediction at normal use conditions.

3.2.1 Long-Range Dependence Effect

LRD, also termed as long-range dependence or long-memory, has been widely observed in nature for various types of time series signals. It relates to the slow decay of auto-correlation or auto-covariance over the time lag so that signals are highly correlated across a long period of time. Mathematically, LRD is often defined through the second-order properties of a stochastic process [82]. Consider a detrended degradation signal $X(t)$, where X is a detrended degradation measure

and $t \geq 0$ is the time index. Denote its auto-covariance function over time lag τ as

$$\rho(\tau) = \text{Cov}(X(t), X(t+\tau)) = E\left[\left(X(t) - E[X(t)]\right)\left(X(t+\tau) - E[X(t+\tau)]\right)\right] \quad (32)$$

$X(t)$ is called a stochastic process with an LRD effect if its auto-covariance decays slowly such that

$$\sum_{\tau=-\infty}^{+\infty} \rho(\tau) = \infty \quad (33)$$

Equation (33) implies that the summation of auto-covariances is divergent, or the auto-covariances of $X(t)$ are non-summable. Typically, stochastic processes with a power-law type of auto-covariance decay have long-range dependence, i.e., when $\rho(\tau) \sim \tau^{-\gamma}, \gamma \in (0,1)$, or equivalently, when there exists a constant c_ρ such that

$$\lim_{\tau \rightarrow \infty} \frac{\rho(\tau)}{\tau^{-\gamma}} = c_\rho; \quad \gamma \in (0,1) \quad (34)$$

In literature, two well-known stochastic processes with LRD effects are the fractional Gaussian noise (i.e., the increment process of an fractional Brownian motion) [48] and fractional difference process [83].

In addition to the aforementioned time-domain definition, another popular and consistent definition is in the spectral domain [84]. That is, $X(t)$ has an LRD effect if there exists a constant c_s such that

$$\lim_{\omega \rightarrow 0} \frac{S(\omega)}{\omega^{-\beta}} = c_s; \quad \beta \in (0,1) \quad (35)$$

where $S(\omega)$ is the power spectral density of $X(t)$ and can be calculated using

$$S(\omega) = \lim_{T \rightarrow \infty} E \left[\frac{1}{2\pi T} \left| \int_0^T X(t) e^{-i\omega t} dt \right|^2 \right] \quad \text{or} \quad S(\omega) = \frac{1}{2\pi} \int_{-\infty}^{\infty} \rho(\tau) e^{-i\omega\tau} d\tau, \quad \text{and} \quad \mathbf{i} = \sqrt{-1} \quad \text{is}$$

the imaginary unit.

In contrast to the long-range dependence defined in (33), $X(t)$ is called a stochastic process with short-range dependence (SRD[85]) if it has summable auto-covariances, i.e., when $\sum_{\tau=-\infty}^{+\infty} \rho(\tau) < \infty$ is finite. For example, stochastic processes with exponentially decaying auto-covariance functions (i.e., $\rho(\tau) \sim e^{-\gamma\tau}$) have short-range dependence. Common stochastic processes with STM effects include the Gaussian white noise [86], Ornstein-Uhlenbeck process [87], and autoregressive and moving average processes [88], etc.

3.2.2 ADT Modeling with Long-Range Dependence

To model ADT with an LRD effect, three basic assumptions are made: (1) the degradation performance measure of an asset has a decreasing trend over the time, without loss of generality; (2) a test asset fails when its degradation level reaches a threshold level y_{th} ; and (3) the physical mechanism of asset degradation does not change over different stress levels. These three assumptions are common and widely made in the ADT literature [39, 63].

Under the aforementioned assumptions, suppose a total number of N units are assigned into M stress levels (s_1, s_2, \dots, s_M) for an accelerated testing, while the stress level of the use condition is s_0 . For accelerating stress level s_i ($1 \leq i \leq M$), denote the number of test units as N_i ($N = \sum_{i=1}^M N_i$). We propose the following model for the degradation of unit j tested under stress s_i at time t_k :

$$Y_{ijk} = f_i(t_{ijk} | s_i, \boldsymbol{\theta}_f) + \sigma B_H(t_{ijk}); \quad i = 1, \dots, M, \quad j = 1, \dots, N_i, \quad k = 1, \dots, K_{ij} \quad (36)$$

where $f_i(\cdot | s_i, \boldsymbol{\theta}_f)$ is a monotonic drift term that describes the degradation trend of assets tested at stress s_i , which depends on parameters vector $\boldsymbol{\theta}_f$; σ is a diffusion parameter that controls the variation of asset degradation; K_{ij} is the number of degradation measurements of asset j tested at stress s_i ; $B_H(\cdot)$ is a standard fractional Brownian motion (FBM); and $H \in (0,1)$ is a Hurst parameter (or exponent) of the FBM. In the literature, FBM has been successfully applied to capturing the LRD effect of various types of time series data such as engineering performance degradation data [4], financial data [72], biological data [10] and telecommunication data [89].

Specifically, $B_H(\cdot)$ in (36) is a generalization of the ordinary standard Brownian motion and can capture the potential LRD effect in a degradation evolution process. Mathematically, it is represented through a Weyl integral as follows [90]:

$$B_H(t) = B_H(0) + \frac{1}{\Gamma(H+1/2)} \left\{ \int_{-\infty}^0 [(t-s)^{H-1/2} - (-s)^{H-1/2}] dB(s) + \int_0^t (t-s)^{H-1/2} dB(s) \right\} \quad (37)$$

where $B(\cdot)$ is a standard Brownian motion, and $\Gamma(\cdot)$ is a gamma function, i.e., $\Gamma(x) = \int_0^{\infty} t^{x-1} e^{-t} dt$. $B_H(t)$ has continuous sample paths with probability one, and the sample paths are almost surely non-differentiable with respect to the time [48]. Moreover, $B_H(\cdot)$ has the following properties: 1) $B_H(0) = 0$; 2) $B_H(t)$ has stationary increments, i.e., $B_H(t) - B_H(s) \sim B_H(t-s)$ for any $s < t$; 3) $E[B_H(t)] = 0$ and $E[B_H^2(t)] = t^{2H}$ for $t \geq 0$; 4) $B_H(t)$ follows a Gaussian distribution for a fixed time $t \geq 0$; 5) $B_H(at) \sim a^H B_H(t)$ for $a > 0$, which is called a self-similar property; and 6) $B_H(\cdot)$ has a covariance function as follows:

$$\text{Cov}(B_H(t), B_H(s)) = E[B_H(t)B_H(s)] = \frac{1}{2} (|t|^{2H} + |s|^{2H} - |t-s|^{2H}) \quad (38)$$

Equation (38) reveals that the Hurst parameter H determines the memory structure of a

degradation process. Specifically, to account for the underlying memory effect in degradation increments, we write the increment process of an FBM as $X_k = B_H(k) - B_H(k-1)$. $\{X_k | k = 1, 2, \dots\}$ is a stationary process with the following auto-covariance function:

$$\begin{aligned} \rho(n) &= E(X_k X_{k+n}) = \text{cov}(B_H(k) - B_H(k-1), B_H(k+n) - B_H(k+n-1)) \\ &= \frac{1}{2} \left[(n+1)^{2H} + (n-1)^{2H} - 2n^{2H} \right] \end{aligned} \quad (39)$$

As $\lim_{n \rightarrow \infty} \rho(n) / [H(2H-1)n^{2H-2}] = 1$, we obtain that $\sum_{n=1}^{\infty} \rho(n) = \infty$ and $\rho(n) > 0$ for a large n when $0.5 < H < 1$; $\sum_{n=1}^{\infty} |\rho(n)| < \infty$ and $\rho(n) < 0$ for a large n when $0 < H < 0.5$; and $\rho(n) = 0$ for $H = 0.5$. These three cases correspond to the LRD, STM and independence effects among the increment process, respectively. Therefore, the proposed ADT model can be classified into different scenarios on the basis of H . That is, when $H = 0.5$, $B_H(t)$ degenerates into the standard Brownian motion $B(t)$ so that the model degenerates into a Wiener process based ADT, in which the memory effect does not exist and the degradation increments are independent. When $H \neq 0.5$, $B_H(t)$ is a non-Markovian self-similar process with stationary increments. Specifically, (1) when $0.5 < H < 1$, the increments of the FBM process for non-overlapping intervals are positively correlated, and the increment process $\{X_k | k = 1, 2, \dots\}$ exhibits long-range dependence; (2) when $0 < H < 0.5$, the increments are negatively correlated, and the increment process has short-range dependence. The case of $H = 1$ is excluded since the corresponding FBM process is a straight line $B_1(t) = tB_1(1)$ with a random slope of $B_1(1)$.

The proposed model (36) is general and flexible to handle a wide class of real ADT problems with different settings of stress-dependent trend term $f_i(\cdot | s_i, \boldsymbol{\theta}_f)$. For example, when the degradation parameters or transformed degradation parameters have a linear relationship with

the applied stress, a linear function of stress vs. degradation parameters can be selected. Otherwise, nonlinear functions and domain-specific physical/empirical stress-dependent functions can be used. Typical functions that determine the stress-degradation relationship include the Arrhenius relationship [76], Eyring relationship [77], generalized Eyring relationship [78] and Inverse power law relationship [79], etc. Later in Section 3.6, we will demonstrate model (36) with a real case study using the Arrhenius relationship to capture the temperature stress effect on asset degradations.

3.2.3 Life Estimation under Normal Use Condition

The main objective of an ADT is to infer asset lifetime distribution at the normal use condition s_0 . The failure time T of an asset at stress s_0 is the first passage time when its degradation level crosses the pre-specified critical value y_{th} . That is,

$$T = \sup \{t | Y(t|s_0) \leq y_{th}\} \quad (40)$$

where $Y(t|s_0) = f(t|s_0, \boldsymbol{\theta}_f) + \sigma B_H(t)$ is the asset degradation path at stress s_0 , and “sup” is the supremum operator.

In most real cases, a closed-form lifetime distribution is not available due to the model complexity, e.g., when the degradation process has a complicated stress-dependent trend function $f(\cdot|s_t, \boldsymbol{\theta}_f)$ integrated with an LRD effect. To overcome this challenge, a Monte Carlo (MC) method is developed to compute the lifetime distribution of assets under normal use condition s_0 . The detailed steps of the MC approach are summarized in Algorithm 3.1.

Algorithm 3.1. A Monte Carlo method to compute asset lifetime distribution at stress s_0

Step 1. Obtain the model parameters $\hat{\boldsymbol{\theta}}$, where $\boldsymbol{\theta} = [\boldsymbol{\theta}_f^T, \sigma, H]^T$ (using the MLE approach

developed in the subsequent Section 3.3);

Step 2. Based on $\hat{\boldsymbol{\theta}}$, simulate P degradation paths at stress level s_0 : For l in $1:P$ (P is the number of MC iterations and should be sufficiently large),

2.1 Simulate the l^{th} standard FBM path $B_H^l(t)$ using a Fast Fourier Transform approach;

2.2 Obtain the degradation path as $Y_l(t|s_0) = f(t|s_0, \boldsymbol{\theta}_f) + \sigma B_H^l(t)$;

Step 3. Compute asset lifetime distribution:

3.1 Compute the failure times based on the P simulated degradation paths using (40), denoted as $T_l (1 \leq l \leq P)$;

3.2 Obtain an empirical estimate of the asset lifetime distribution at stress s_0 as

$$F(t|s_0, \hat{\boldsymbol{\theta}}) = P^{-1} \sum_{l=1}^P \mathbf{1}_l(T_l); \quad \mathbf{1}_l(T_l) = \begin{cases} 1, & \text{if } T_l \leq t \\ 0, & \text{otherwise} \end{cases}$$

Specifically, in Step 2.1 of Algorithm 3.1 to generate a standard FBM path $B_H^l(t)$ a Fast Fourier Transform (FFT) algorithm is applied [91]. This algorithm has computational advantage over several alternative approaches such as Cholesky factorization [55] and Hosking method [53]. More specifically, the computational complexity of the FFT algorithm is $O(n \log(n))$ for simulating a discretized $B_H^l(t)$ of length n , while those of Cholesky factorization and Hosking method are $O(n^3)$ and $O(n^2)$, respectively. Therefore, the FFT algorithm can be used to simulate an FBM path much faster than the other two methods when n is large and thus is selected. The key idea of the algorithm is to first embed the auto-covariance matrix of $\{B_H^l(t)|t = i/n, i = 1, 2, \dots, n\}$, denoted as \mathbf{G} , into a Circulant matrix \mathbf{C} of dimensions $m \times m$, where $m = 2^{g+1}$, $g \in \mathbb{N}^*$ and 2^g is

the first power of two such that $2^s > N$. Then, one can generate a vector $\boldsymbol{\omega} = (\omega_0, \omega_1, \dots, \omega_{m-1})^T \sim MVN(\mathbf{0}, \mathbf{G})$ and obtain $\{B_H^l(t) | t = i/n, i = 1, 2, \dots, n\}$ from $\boldsymbol{\omega}$. The details of the FFT algorithm are summarized in Algorithm 3.2.

Algorithm 3.2. An FFT algorithm for the simulation of $B_H^l(t); t = i/n, i = 1, 2, \dots, n$

Step 1. Compute the eigenvalues $\{\lambda_k\}_{k=0,1,\dots,m-1}$ of a circulant matrix \mathbf{C} defined as follows using

an FFT approach: $\lambda_k = \sum_{j=0}^{m-1} c_j \exp\left(2\pi\mathbf{i} \frac{jk}{m}\right); k = 0, 1, \dots, m-1$ where

$$\mathbf{C} = \begin{pmatrix} c_0 & c_1 & \cdots & c_{m-1} \\ c_{m-1} & c_0 & \cdots & c_{m-2} \\ \vdots & \vdots & \ddots & \vdots \\ c_1 & c_2 & \cdots & c_0 \end{pmatrix}; c_j = \begin{cases} \rho(j/n) & \text{if } 0 \leq j \leq m/2 \\ \rho((m-j)/n) & \text{if } m/2 < j \leq m-1 \end{cases}; \text{ and } \rho(\cdot) \text{ is the}$$

auto-covariance function of the increment process of a standard FBM defined in (39).

Step 2. Calculate $\mathbf{W} = \mathbf{Q}^* \mathbf{Z}$ ($\mathbf{C} = \mathbf{Q} \boldsymbol{\Lambda} \mathbf{Q}^*$ and $\mathbf{Z} \sim MVN(\mathbf{0}, \mathbf{I}_m)$); $\boldsymbol{\Lambda}$ is a diagonal matrix

containing eigenvectors of \mathbf{C} , \mathbf{I}_m is a $m \times m$ dimensional identity matrix, and \mathbf{Q} is

a unitary matrix with the $(j, k)^{th}$ entry being

$$\mathbf{Q}_{j,k} = m^{-1/2} \exp\left(-2\pi\mathbf{i} \frac{jk}{m}\right); j, k = 1, 2, \dots, m).$$

2.1 Generate U_0 and V_0 from standard normal distributions independently, i.e.,

$$U_0, V_0 \sim N(0, 1). \text{ Write } W_0 = U_0 \text{ and } W_{m/2} = V_0;$$

2.2 For $1 \leq j \leq m/2$, generate $U_j, V_j \sim N(0, 1)$ independently and let

$$W_j = \frac{1}{\sqrt{2}}(U_j + \mathbf{i}V_j); W_{m-j} = \frac{1}{\sqrt{2}}(U_j - \mathbf{i}V_j);$$

Step 3. Construct the fractional Gaussian noise $X(t)$ defined as follows, using an FFT

$$\text{method: } X\left(\frac{k}{n}\right) = \frac{1}{\sqrt{m}} \sum_{j=0}^{m-1} \sqrt{\lambda_j} W_j \exp\left(-2\pi i \frac{jk}{m}\right), \quad k = 0, 1, \dots, m-1;$$

Step 4. Obtain $B_H^l(t)$ as the cumulative sums of the fractional Gaussian noise:

$$B_H^l(0) = 0; \quad B_H^l\left(\frac{i}{n}\right) = B_H^l\left(\frac{i-1}{n}\right) + X\left(\frac{i-1}{n}\right) \quad \text{for } i = 1, 2, \dots, n.$$

Notice Algorithm 3.2 generates $B_H^l(t)$ that is discretized into a time interval of $[0, 1]$ with equal spaces. The self-similar property of FBM, i.e., $B_H(at) \sim a^H B_H(t)$, can be utilized to simulate an FBM with a general time range $[0, a]$ as needed. a can be selected with a pre-specified value or through prior knowledge in practice.

3.3 Model Parameter Estimation

Based on Equations (36) and (37), the proposed LRD-integrated ADT model depends on parameters $\boldsymbol{\theta} = [\boldsymbol{\theta}_f^T, \sigma, H]^T$ that need to be specified. In practice, $\boldsymbol{\theta}$ will be estimated given the observed data from an ADT experiment. In this section, we develop an MLE approach to jointly estimate the parameters in $\boldsymbol{\theta}$.

Denote the degradation observations of the N assets tested at M stress levels as $\mathbf{Y} = \{Y_{ijk} \mid i = 1, 2, \dots, M; j = 1, 2, \dots, N_i, k = 1, 2, \dots, K_{ij}\}$. Let $\mathbf{Y}_{ij} = [Y_{ij1}, Y_{ij2}, \dots, Y_{ijK_{ij}}]^T$ be the collection of degradation measurements of the j^{th} asset tested at stress s_i , and define

$$\mathbf{f}_{ij} = [f_i(t_{ij1} | s_i, \boldsymbol{\theta}_f), f_i(t_{ij2} | s_i, \boldsymbol{\theta}_f), \dots, f_i(t_{ijK_{ij}} | s_i, \boldsymbol{\theta}_f)]^T \quad \text{and} \quad \mathbf{B}_H^{ij} = [B_H(t_{ij1}), B_H(t_{ij2}), \dots, B_H(t_{ijK_{ij}})]^T.$$

Then, for the j^{th} asset tested at stress level s_i we have

$$\mathbf{Y}_{ij} = \mathbf{f}_{ij} + \sigma \mathbf{B}_H^{ij} \quad (41)$$

Notice that the initial asset degradations at time $t = 0$ are included in the trend function $f_i(\bullet)$.

In Equation (41), based on the property of FBM [4] \mathbf{Y}_{ij} follows a multivariate normal distribution, i.e.,

$$\mathbf{Y}_{ij} \sim MVN(\mathbf{f}_{ij}, \sigma^2 \mathbf{\Omega}_{ij}) \quad (42)$$

where $\mathbf{\Omega}_{ij}$ is a $K_{ij} \times K_{ij}$ dimensional matrix with the $(u, v)^{th}$ entry being $\mathbf{\Omega}_{ij}(u, v) = \text{Cov}(B_H(t_{iju}), B_H(t_{ijv})) = \frac{1}{2} (t_{iju}^{2H} + t_{ijv}^{2H} - |t_{iju} - t_{ijv}|^{2H})$. Therefore, the log-likelihood function given \mathbf{Y}_{ij} can be derived as follows:

$$\begin{aligned} l_{ij}(\boldsymbol{\theta} | \mathbf{Y}_{ij}, s_i) &= -\frac{1}{2} \left[K_{ij} \ln(2\pi) + \ln(|\sigma^2 \mathbf{\Omega}_{ij}|) + (\mathbf{Y}_{ij} - \mathbf{f}_{ij})^T (\sigma^2 \mathbf{\Omega}_{ij})^{-1} (\mathbf{Y}_{ij} - \mathbf{f}_{ij}) \right] \\ &= -\frac{K_{ij}}{2} \ln(2\pi\sigma^2) - \frac{1}{2} \ln|\mathbf{\Omega}_{ij}| - \frac{1}{2\sigma^2} (\mathbf{Y}_{ij} - \mathbf{f}_{ij})^T \mathbf{\Omega}_{ij}^{-1} (\mathbf{Y}_{ij} - \mathbf{f}_{ij}) \end{aligned} \quad (43)$$

Using the result of Equation (43), the log-likelihood function given the collection of ADT data observations \mathbf{Y} and \mathbf{s} can be developed as

$$\begin{aligned} l(\boldsymbol{\theta} | \mathbf{Y}, \mathbf{s}) &= \sum_{i=1}^M \sum_{j=1}^{N_i} l_{ij}(\boldsymbol{\theta} | \mathbf{Y}_{ij}, s_i) \\ &= -\frac{1}{2} \sum_{i=1}^M \sum_{j=1}^{N_i} \left\{ K_{ij} \ln(2\pi\sigma^2) + \ln|\mathbf{\Omega}_{ij}| + \frac{1}{\sigma^2} (\mathbf{Y}_{ij} - \mathbf{f}_{ij})^T \mathbf{\Omega}_{ij}^{-1} (\mathbf{Y}_{ij} - \mathbf{f}_{ij}) \right\} \end{aligned} \quad (44)$$

The model parameters can be obtained by maximizing the log-likelihood function with respect to parameters $\boldsymbol{\theta}$, i.e.,

$$\hat{\boldsymbol{\theta}} = \arg \max_{\boldsymbol{\theta}} \{l(\boldsymbol{\theta} | \mathbf{Y}, \mathbf{s})\} \quad (45)$$

To maximize the log-likelihood function in (45), analytical solutions often do not exist due to model complexity. In this chapter, the Nelder–Mead method [92] is used as a numerical optimization approach to calculate $\hat{\boldsymbol{\theta}}$. It is a direct search method that has been successfully applied to solve a variety of classical nonlinear optimization problems with multi-dimensional

spaces. Notice that for some restricted parameters (e.g., $\sigma > 0$ and $0 < H < 1$), a parameter transformation has been applied to ensure that the estimated values are within the valid ranges. For σ , a logarithmic transformation is performed, i.e., $\sigma^* = \log(\sigma)$, while for H a logit transformation is applied, i.e., $H^* = \log(H / (1 - H))$. Then, parameters σ and H are obtained using a back-transformation technique.

In addition to the point estimation of parameters $\boldsymbol{\theta}$ provided by (45), we further develop a method for an interval estimation of $\boldsymbol{\theta}$. Interval estimation provides a confidence interval within which the true parameter is covered with a certain probability/confidence level. Specifically, the covariance matrix of $\hat{\boldsymbol{\theta}}$ can be calculated as the inverse of the observed Fisher information matrix $\mathbf{I}(\hat{\boldsymbol{\theta}})$, i.e., $\hat{\Sigma}(\hat{\boldsymbol{\theta}}) = \mathbf{I}^{-1}(\hat{\boldsymbol{\theta}})$, where $\mathbf{I}(\hat{\boldsymbol{\theta}})$ is calculated as [51]:

$$\mathbf{I}(\hat{\boldsymbol{\theta}}) = - \left. \frac{\partial^2 l(\boldsymbol{\theta} | \mathbf{Y}, \mathbf{s})}{\partial \boldsymbol{\theta} \partial \boldsymbol{\theta}^T} \right|_{\boldsymbol{\theta} = \hat{\boldsymbol{\theta}}} \quad (46)$$

The standard error of $\theta \in \boldsymbol{\theta}$, denoted as $se(\hat{\theta})$, can be obtained from $\sqrt{\text{diag}(\hat{\Sigma}(\hat{\boldsymbol{\theta}}))}$. As $\hat{\boldsymbol{\theta}}$ is asymptotically normal based on the maximum likelihood theory under a large sample assumption, the $100(1 - \alpha_0)\%$ confidence interval of θ can be constructed as $(\hat{\theta} - z_{1 - \alpha_0/2} \times se(\hat{\theta}), \hat{\theta} + z_{1 - \alpha_0/2} \times se(\hat{\theta}))$, where z_x is the x quantile of the standard normal distribution. Notice that the aforementioned interval estimation is more suitable for unrestricted parameters. For restricted parameters that are estimated using a parameter transformation method, the standard errors are calculated using the Delta method [51], and the confidence intervals can be obtained with a back-transformation approach.

3.4 Hypothesis Test of Memory Effect

In the real world, the degradation increments of an asset may exhibit an LRD, STM or independence effect. To test the specific memory property of a degradation process, we develop a likelihood-ratio hypothesis test based on the proposed ADT model. Specifically, when the detrended degradation process is Markovian with independent increments, the Hurst parameter equals 0.5 and the FBM term in (36) degenerates into an ordinary Brownian motion. Considering this fact, we specify the null and alternative hypotheses as

$$H_0 : H = 0.5 \quad \text{vs.} \quad H_1 : H \neq 0.5$$

Built upon the aforementioned H_0 and H_1 , the likelihood-ratio test statistic can be calculated as follows:

$$\lambda(DATA) = -2 \ln \frac{\sup\{L(\boldsymbol{\theta}|DATA, H_0)\}}{\sup\{L(\boldsymbol{\theta}|DATA, H_0 \cup H_1)\}} \quad (47)$$

where ‘‘sup’’ refers to the supremum operator; $DATA = \{\mathbf{Y}, \mathbf{s}\}$ is a collection of data observations in an ADT; $L(\boldsymbol{\theta}|DATA, H_0)$ and $L(\boldsymbol{\theta}|DATA, H_0 \cup H_1)$ are the likelihood functions under the null hypothesis H_0 and the full model $H_0 \cup H_1$, respectively. Specifically, $L(\boldsymbol{\theta}|DATA, H_0 \cup H_1)$ is calculated by substituting the estimated parameters $\hat{\boldsymbol{\theta}}$ of Equation (45) into Equation (44), while $L(\boldsymbol{\theta}|DATA, H_0)$ is computed by constraining $H = 0.5$ in Equation (45).

By Wilks' theorem, the test statistic $\lambda(DATA)$ can be approximated by a chi-square distribution under a large sample assumption with degrees of freedom (DOF) being $df = df_1 - df_0$. df_0 and df_1 are the DOF of the null and full models, respectively [93]. Therefore, given a specified test significance level (or Type I error) α_0 , the null hypothesis (H_0) will be rejected if

$\lambda(DATA) > \chi_{df_1-df_0}^2(\alpha_0)$, where $\chi_{df_1-df_0}^2(\alpha_0)$ denotes the upper α_0 quantile of the chi-square distribution with a DOF of $df_1 - df_0$. Or, equivalently, one can make a test conclusion using a p -value criterion. The p -value of the hypothesis test can be calculated as

$$p\text{-value} = \Pr\left(\chi_{df_1-df_0}^2 > \lambda(DATA)\right) \quad (48)$$

H_0 will be rejected if $p < \alpha_0$. More specifically, we have $df_1 - df_0 = 1$ in this chapter. If H_0 is rejected, one can conclude that the LRD effect exists among degradation increments if $\widehat{H} > 0.5$, or the STM effect exists if $\widehat{H} < 0.5$. Otherwise, the asset degradation follows a Markovian process.

3.5 Simulation Study

Simulation studies are conducted to assess the performance of the proposed LRD-integrated ADT model and developed methods. Section 3.5.1 introduces the data simulation approach, Sections 3.5.2 – 3.5.4 provide the data analysis results using the proposed methods, and Section 3.5.5 conducts model comparisons.

3.5.1 Data Simulation

We first simulate a set of ADT data with LRD effects using the temperature as an accelerating stress variable. To formulate the accelerating stress effect, the Arrhenius relationship [39] that has been widely applied for temperature-elevated accelerated testing is chosen.

Specifically, the ADT data are simulated using the following accelerated degradation function:

$$M_1 : Y = D_0 \exp(-R_u \times AF(temp) \times t) + \sigma B_H(t);$$

$$AF(temp) = \exp\left(E_a \left(\frac{11605}{temp_u + 273.15} - \frac{11605}{temp + 273.15}\right)\right) \quad (49)$$

where D_0 is the initial degradation level, which is set as one in this study without loss of generality;

R_u is the reaction rate at the use temperature $temp_u$ (in degrees Celsius); $AF(temp)$ represents the

acceleration factor at a temperature level of $temp$; and E_a denotes the reaction activation energy. For notation simplification purposes, we set $\alpha = E_a$ and $\beta = \log(R_u)$ across this chapter. Therefore, the parameters of M_1 model are summarized as $\boldsymbol{\theta} = [H, \sigma, \alpha, \beta]^T$.

To simulate the ADT data with LM effects using the M_1 model in (49), the parameters are specified as $\boldsymbol{\theta} = [0.8, 0.0025, 0.5, -5.5]^T$. $M = 3$ levels of temperature are set for the accelerated testing, i.e., 40°C, 60°C, 80°C. Under each temperature, $N_i = 3$ (for $i = 1 \sim 3$) assets are tested so that three degradation paths are simulated. The time points for degradation measurements are equally spaced as $0 = t_1 < t_2 < \dots < t_{100} = 35$ hours with $K_{ij} = 100$ for $i, j = 1 \sim 3$. Figure 3.1 illustrates the simulated ADT data at the three test temperatures.

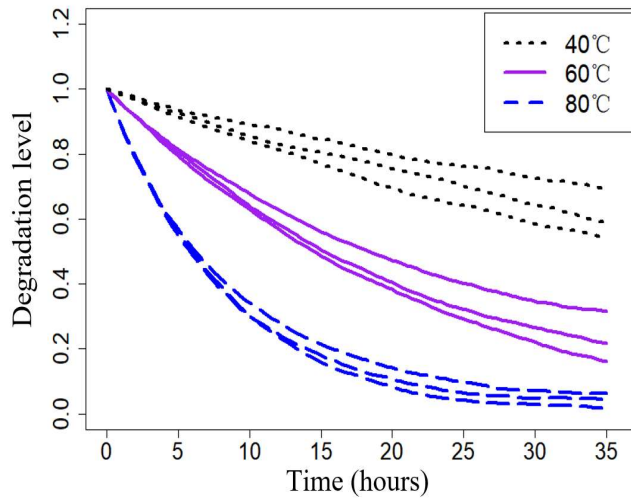


Figure 3.1. Simulated degradation paths at three accelerated temperature levels

3.5.2 Model Parameter Estimation

The proposed methods are then applied to analyzing the simulated ADT data in Figure 3.1. Based on the developed MLE method in Section 3.3, the model parameters and corresponding standard errors are estimated using Equations (45) – (46) and are listed in Table 3-1. The results

show that the estimated parameters are close to the specified values, which indicates that the developed MLE approach performs well for parameter estimation under the current sample size.

Table 3-1. Point and Standard Error Estimation of M_1 Parameters

Parameters	H	σ	α	β
Point estimate	0.807	0.00254	0.499	-5.497
Standard error	0.019	1.5×10^{-4}	0.012	0.073

To further examine the performance of the MLE approach, we repeat the simulation process outlined in Section 3.5.1 for $R=1000$ times and compute the Root Mean Square Errors (RMSEs) of parameter estimation. The RMSE of a parameter $\theta \in \boldsymbol{\theta}$ is calculated as

$$RMSE(\theta) = \sqrt{\sum_{i=1}^R (\hat{\theta}_i - \theta)^2 / R},$$

where $\hat{\theta}_i$ denotes the estimate of θ in the i^{th} iteration. Different

sample sizes (i.e., number of testing assets at each stress level) of ADT are also considered, i.e., $N_i = 3, 6$ and 10 . The results are summarized in Table 3-2.

Table 3-2. RMSEs of Parameter Estimation under Different Sample Sizes

Sample size (N_i)	$RMSE(\hat{H})$	$RMSE(\hat{\sigma})$	$RMSE(\hat{\alpha})$	$RMSE(\hat{\beta})$
3	0.021	1.6×10^{-4}	0.011	0.071
6	0.015	1.1×10^{-4}	0.008	0.051
10	0.011	8.1×10^{-5}	0.006	0.039

From Table 3-2, it is observed that as the sample size increases the RMSEs of model parameter estimation decrease to small levels, which further demonstrates the effectiveness of the MLE approach in terms of parameter estimation accuracy.

3.5.3 Test of Degradation Memory Effect

For the simulated ADT data, the likelihood-ratio test statistic is calculated by using

Equation (47). Specifically, the supremum log-likelihoods for the null and full models are calculated as $\ln\left\{\sup\{L(\boldsymbol{\theta}|DATA, H_0)\}\right\} = 4837.3$ and $\ln\left\{\sup\{L(\boldsymbol{\theta}|DATA, H_0 \cup H_1)\}\right\} = 5034.4$, respectively. The test statistic is $\lambda(DATA) = -2(4837.3 - 5034.4) = 394.2$. The p -value based on this test statistic is computed using Equation (48) and satisfies $p\text{-value} = \Pr(\chi_1^2 > 394.2) \ll 0.01$. Therefore, there is strong evidence to reject the null hypothesis H_0 at a significance level of $\alpha_0 = 0.01$. Considering $\widehat{H} = 0.807 > 0.5$ we conclude that there is an LRD effect in the degradation increment process. This result is consistent with the ADT data simulation process.

3.5.4 Lifetime Distribution

Based on the estimated parameters in Table 3-1, the life distribution at the normal use temperature can be predicted. Specifically, the normal use temperature is set as $s_0 = 20^\circ\text{C}$, and two failure threshold values of degradation are selected for illustration purposes, i.e., $y_{th} = 0.5$ and 0.6 . By substituting these parameters into Algorithms 3.1 and 3.2, the Probability Density Function (PDF) of asset lifetime is calculated and illustrated in Figure 3.2. It can be seen that for a larger failure threshold value, the mean lifetime is shorter.

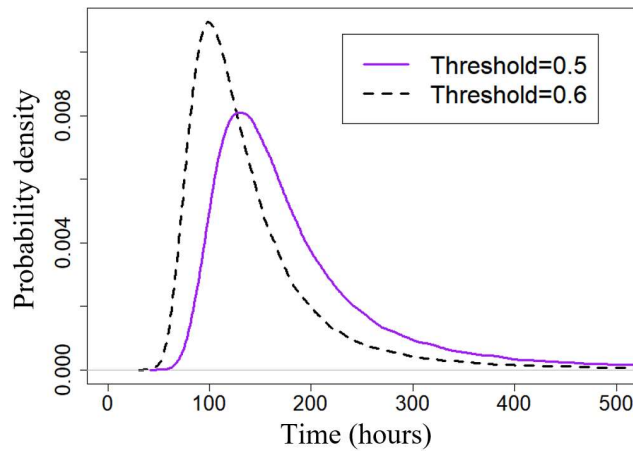


Figure 3.2. PDFs of lifetime at normal use temperature with different failure threshold values

3.5.5 Model Comparison

To demonstrate the advantage of the proposed LRD integrated ADT model, a traditional ADT method without a consideration of LRD effects is used as a benchmark for a comparison. Specifically, the traditional Wiener process based ADT [16] that has wide real applications is selected, which has the following degradation function at stress $temp$:

$$M_2 : Y = D_0 \exp(-R_u \times AF(temp) \times t) + \sigma B(t) \quad (50)$$

where $B(t)$ denotes the standard Brownian motion. This M_2 model depends on three parameters, i.e., $\theta = [\sigma, \alpha, \beta]^T$, where its Hurst parameter satisfies $H = 0.5$.

The M_2 model is applied to studying the simulated ADT data in Figure 3.1. By using the MLE approach, the model parameters and corresponding standard errors are computed and summarized in Table 3-3.

Table 3-3. Point and Standard Error Estimation of M_2 Parameters

Parameters	σ	α	β
Point estimate	0.00189	0.501	-5.52
Standard error	4.47×10^{-5}	0.0043	0.026

Based on the estimated parameters in Table 3-3, we predict the life distribution at the normal use temperature of $s_0 = 20^\circ\text{C}$. For a comparison with the proposed M_1 model, the failure threshold value is fixed as $y_{th} = 0.6$. The lifetime distributions under M_1 and M_2 models along with the histogram of true lifetimes (when the degradation level crosses the failure threshold) are calculated and illustrated in Figure 3.3. Specifically, the lifetime means of M_1 and M_2 are 135.8 and 127.4, respectively; and the lifetime standard deviations of M_1 and M_2 are 57.9 and 8.8, respectively. It is observed that the mean values are relatively close. However, the traditional M_2

model that ignores the LRD effect significantly underestimates the lifetime uncertainty, which causes a large bias of life testing. Therefore, incorporating the LRD effect is critical in an accelerated testing of asset lifetime.

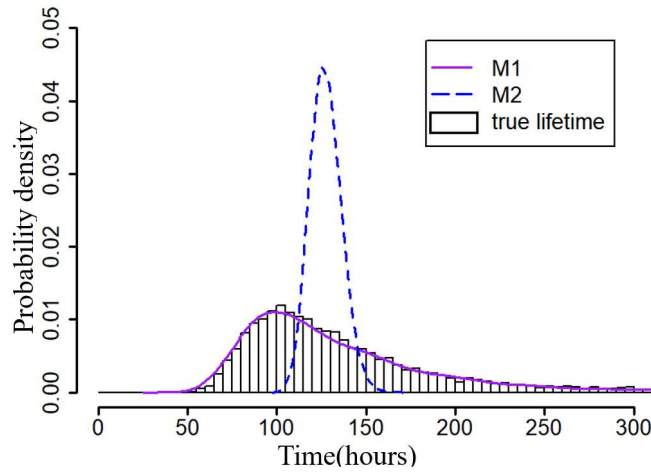


Figure 3.3. PDFs of lifetime at normal use temperature for M_1 and M_2

In addition to M_2 , we further compare the proposed model with a random-effect Wiener process model, i.e., M_{random} as follows:

$$M_{\text{random}} : Y = D_0 \exp(-R_u \times AF(\text{temp}) \times t) + \sigma B_H(t); \alpha = E_a; \beta = \log(R_u); \beta \sim N(\mu_\beta, \sigma_\beta^2) \quad (51)$$

The model parameters $\theta = [\sigma, \alpha, \mu_\beta, \sigma_\beta]^T$ are estimated using an MLE approach and listed in Table 3-4, along with the corresponding standard errors.

Table 3-4. Point and Standard Error Estimation of M_{random} Parameters

Parameters	σ	α	μ_β	σ_β
Point estimate	0.00231	0.417	-5.34	1.35
Standard error	1.3×10^{-5}	0.0011	0.39	0.12

For the comparison, the Bayesian Information Criterion (BIC) is applied, which is defined as follows:

$$BIC = k \ln(N^*) - 2\hat{l} \quad (52)$$

where k is the number of DOF of a model, N^* is the total number of degradation observations, and \hat{l} is the maximized log-likelihood value of the model evaluated at parameters $\hat{\theta}$. BIC introduces a penalty term for the number of model parameters, and the model with the lowest BIC value is preferred. Table 3-5 summarizes the BIC values of M_1 , M_2 and M_{random} . It can be seen that the proposed M_1 performs the best (with the smallest BIC value), M_2 performs slightly worse than M_1 , and M_{random} ranks last.

Table 3-5. Log-likelihood Values and BIC Values of M_1 , M_2 and M_{random}

Model index	Log-likelihood	# of parametes	BIC
M_1	5034.373	4	-10041.5
M_2	4837.341	3	-9654.245
M_{random}	4658.161	4	-9289.073

3.6 Case Study

To demonstrate the proposed ADT model, a physical experiment has been designed and conducted as a real case study, regarding the ADT of Pt/black TiO₂ under an accelerating stress of temperature. Section 3.6.1 briefly describes the experiment and data collection. Sections 3.6.2 – 3.6.4, respectively, present the results of model parameter estimation, hypothesis test of long-range dependence and lifetime estimation at the normal use temperature. Multiple model comparisons are conducted in Section 3.6.5 to illustrate the advantages of the proposed ADT model over classic methods that ignore the LRD effect.

3.6.1 Experimental and Data Collection

We conducted an accelerated testing on the performance degradation of Pt/black TiO₂ photocatalyst. Pt/black TiO₂ is a type of catalyst used for the acceleration of a photoreaction process and has been receiving increasing attentions in the environmental and

energy industries, e.g., photocatalytic organic pollutant treatment, hydrogen generation, and photothermal therapy. In this experiment, we apply the Pt/black TiO₂ in photocatalytic carbon dioxide reforming, a process that produces H₂ and CO from CH₄ and CO₂, i.e., $\text{CH}_4 + \text{CO}_2 \rightarrow 2\text{H}_2 + 2\text{CO}$. During the reforming process, the performance of Pt/black TiO₂ (measured by products yield of H₂ and CO) decreases over the time. Once the reaction yield level reaches a threshold value, the Pt/black TiO₂ fails. As the temperature significantly affects the performance degradation process, we conducted an ADT of Pt/black TiO₂ using the temperature as the accelerating stress.

Specifically, the experiment consists of three steps. First, the Pt/black TiO₂ was synthesized using an impregnation method, then hydrogenated and dispersed on the light-diffuse-reflection surface of SiO₂ substrate. Next, the catalyst/substrate was located in a quartz tube reactor and heated to a specified temperature by an electrical furnace. Finally, CH₄/CO₂ mixture gas (1:1 ratio) flow was introduced into the reactor, and the products (H₂ and CO) were analyzed via Gas Chromatography (GC, Agilent 6890 system) and Mass Spectrometry (MS, Agilent 5977 system) as illustrated in Figure 3.4 (left). In this study, to accelerate the testing two elevated temperatures were set, i.e., 550 °C and 600 °C, while the use condition was specified as 450 °C. Figure 3.4 (right) illustrates the measured degradation (i.e., normalized products yield) of Pt/black TiO₂ over the time under 550 °C and 600 °C. The total number of degradation measurements is $N^* = 174$.

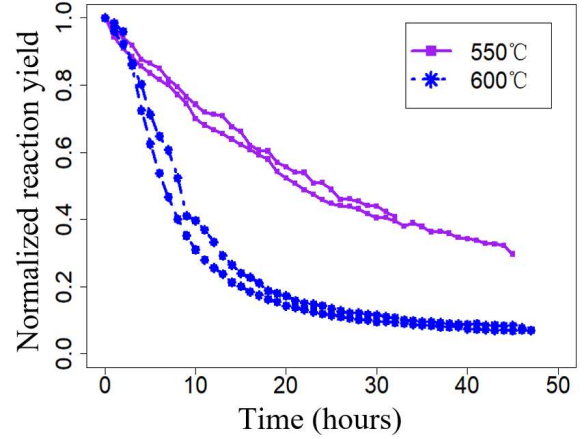


Figure 3.4 The accelerated testing system (left) and normalized performance degradation of Pt/black TiO₂ at two accelerated temperatures (right)

3.6.2 Data Analysis and Parameter Estimation

To analyze the collected ADT data, we apply the proposed LRD integrated ADT model with two different trend terms, i.e., the M_1 model in Equation (49) and the following M_3 model:

$$M_3 : Y = \exp(-bt) + \sigma B_H(t), \quad b = \left(\frac{T + 273.15}{1000} \right)^\alpha \quad (53)$$

The difference between M_1 and M_3 is that M_1 uses the Arrhenius relationship for the temperature acceleration, while M_3 chooses a simple power law relationship. The parameters of the M_3 model are $\theta = [H, \sigma, \alpha]^\top$.

Using Equations (45)–(46), the parameters and corresponding standard errors of M_1 and M_3 are calculated and listed in Table 3-6.

Table 3-6. Parameter Estimation Results of M_1 and M_3

Parameters		H	σ	α	β
M_1	Point estimate	0.77	0.0032	1.23	-5.91
	Standard error	0.034	2.54×10^{-4}	0.074	0.19
M_3	Point estimate	0.78	0.0032	18.53	—
	Standard error	0.033	2.7×10^{-4}	0.15	—

3.6.3 Test of Degradation Memory Effect

We test the memory effect of the degradation process using both the M_1 and M_3 models given the experimental ADT data. The likelihood-ratio test statistics for M_1 and M_3 are calculated using Equation (47) as $\lambda_{M_1}(DATA) = -2(737.3 - 757.7) = 40.8$ and $\lambda_{M_3}(DATA) = -2(728.9 - 753.1) = 48.4$, respectively. Next, the p -values of both models are computed following Equation (48) and satisfy p -value $\ll 0.01$. Therefore, both models imply that there is strong evidence to reject the null hypothesis H_0 . As the estimated Hurst parameters of M_1 and M_3 are 0.77 and 0.78, respectively, we conclude that there is a significant LRD effect in the degradation increment process of Pt/black TiO₂.

3.6.4 Lifetime Estimation

The lifetime distribution at the normal use temperature can be inferred based on the parameter estimates in Table 3-6. The normal use temperature is set as $temp_U = 450^\circ\text{C}$, and the normalized failure threshold value of degradation is set as 0.6. Based on Algorithms 3.1 and 3.2, the lifetime distributions at $temp_U = 450^\circ\text{C}$ using M_1 and M_3 are predicted and illustrated in Figure 3.5. It is observed that the predicted distributions of the two models are similar and consistent.

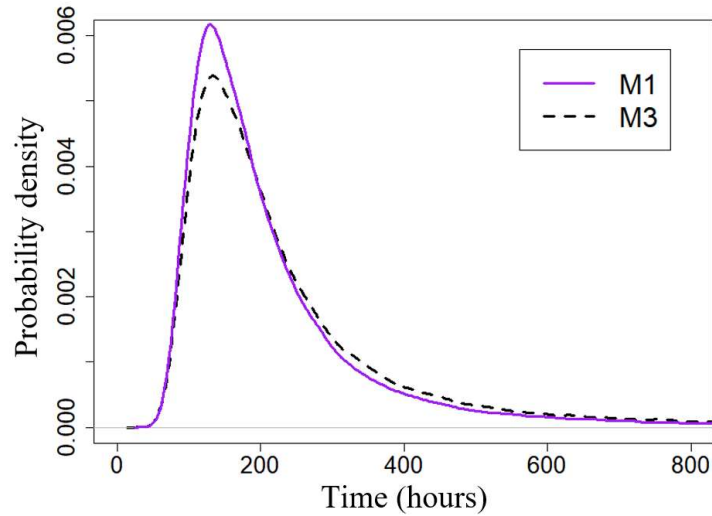


Figure 3.5. Predicted lifetime distribution at 450°C

3.6.5 Model Comparison

To demonstrate the advantage of the proposed model, we choose two benchmark approaches without considering LRD effects. That is, we replace the FBM terms in M_1 and M_3 with standard Brownian motion, which results in M_2 and the following M_4 , respectively:

$$M_4: Y = \exp(-bt) + \sigma B(t), \quad b = \left(\frac{T + 273.15}{1000} \right)^\alpha \quad (54)$$

Based on the MLE approach, the point and standard error estimates of parameters of M_2 and M_4 are calculated and listed in Table 3-7.

Table 3-7. Parameter Estimation Results of M_2 and M_4

Parameters		σ	α	β
M_2	Point estimate	0.0032	1.26	-5.98
	Standard error	1.7×10^{-4}	0.04	0.10
M_4	Point estimate	0.0035	18.69	—
	Standard error	1.3×10^{-4}	0.10	—

Given the estimated parameters, we predict the lifetime distributions of Pt/black TiO₂ at the normal use temperature $temp_U = 450^\circ\text{C}$ using both M_2 and M_4 , and compare the results with those of M_1

and M_3 . Figure 3.6 (left) illustrates the predicted lifetime distributions of M_1 versus M_2 , and Figure 3.6 (right) shows the predicted lifetime distributions of M_3 versus M_4 . Specifically, the lifetime means of $M_1 \sim M_4$ are 216.5, 202.8, 234.2 and 220.7 (hours), respectively; and the lifetime standard deviations of $M_1 \sim M_4$ are 138.9, 30.5, 152.0 and 38.1 (hours), respectively. Again, the comparisons show that without considering the LRD effect both M_2 and M_4 significantly underestimate the lifetime uncertainty, which is consistent with the results obtained in the simulation study of Section 3.5.

To further compare the performance of $M_1 \sim M_4$ models, the BIC values for $M_1 \sim M_4$ are calculated using Equation (52). Table 3-8 summarizes the log-likelihood values, numbers of model parameters and BIC values of the four models. From Table 3-8, M_1 has a slightly smaller BIC value than M_3 , so M_1 performs slightly better than M_3 . Similarly, M_2 performs slightly better than M_4 . One reason is that both M_1 and M_2 utilize the Arrhenius relationship to capture the accelerating stress effects, which accounts for the physical mechanism of temperature elevated degradation acceleration, and thus often perform more accurately than M_3 and M_4 , respectively. Moreover, M_1 has a significantly smaller BIC than M_2 , and M_3 has a significantly smaller BIC than M_4 . This implies that M_1 and M_3 that integrate the LRD effect perform much better than the traditional two benchmark approaches.

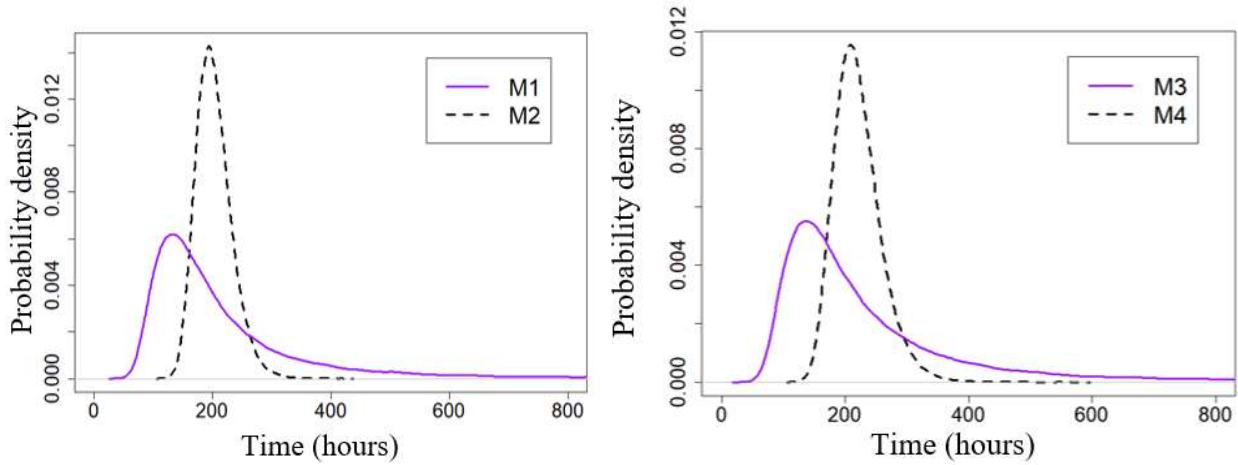


Figure 3.6. Lifetime distribution prediction at normal use temperature of M_1 versus M_2 (left) and M_3 versus M_4 (right)

Table 3-8. Log-likelihood Values and BIC Values of $M_1 \sim M_4$

Model index	Log-likelihood	# of parameters	BIC
M_1	757.69	4	-1494.61
M_2	737.31	3	-1459.04
M_3	753.12	3	-1490.66
M_4	728.95	2	-1447.51

3.7 Conclusion

long-range dependence effects have recently been discovered in the performance degradations of several engineering assets and significantly impact the accuracy of asset reliability/life testing. Motivated by this fact, in this chapter we propose a novel ADT model by incorporating the long-range dependence effects in asset degradation. A maximum likelihood estimation approach is developed for the parameter estimation of the model. A likelihood-ratio hypothesis test is developed based on the proposed model to quantitatively test whether the long-range dependence exist or not given a collection of ADT data. Simulation studies are implemented to investigate the performance of the developed methods. Physical experiments are conducted on the degradation of Pt/black TiO_2 to demonstrate the proposed model. Both simulation and case

study results show that the proposed ADT model, through an incorporation of the long-range dependence effects, fundamentally improves the life testing accuracy, while traditional ADT methods significantly underestimate the lifetime uncertainty.

CHAPTER 4

SURFACE ANOMALY DETECTION CONSIDERING LONG-RANGE DEPENDENCE

4.1 Introduction

4.1.1 Motivation

With advances in image acquisition technology, image-based monitoring has been receiving increasing attention in statistical process control (SPC). In manufacturing, material/product surfaces as a common type of image data often demonstrate complex spatial patterns, such as complicated surface profile and roughness, surface morphology variation, and intricate surface texture. These geometric characteristics highly impact material properties such as strength, stiffness, and damage-resistance, which in turn significantly influence product quality and usage life. Therefore, it is crucial to build efficient spatial models that can accurately characterize those complex spatial patterns (both variations and correlations) of material surfaces. Based on appropriate surface modeling, subsequent quality monitoring and control of material surfaces can be effectively conducted.

Recently, with the advancement of metrology technology, a long-range dependence (LRD) effect has been detected in various spatial/image data [94-96]. The LRD has been firstly discovered in one-dimensional temporal data, and it refers to the fact that the autocovariances are non-summable so that correlations among temporal measurements are strong across a long period of time. A common characteristic of LRD is that the autocorrelation decay demonstrates a heavy tail. For instance, Si, et al. [5] demonstrated that the performance degradation process of a chemical catalyst exhibits the LRD effect. Lahmiri, et al. [97] detected the LRD effect within the volatility of seven Bitcoin markets. Iliopoulou, et al. [98] illustrated that the annual precipitation records of 12,000 years, obtained by paleoclimatic reconstructions, exhibit the LRD effect. Beyond the one-dimensional temporal data, the existence of LRD effects has recently been demonstrated in several

two-dimensional spatial data. Similar to the temporal LRD, the spatial LRD refers to the slow autocorrelation decay over spatial distances, so that strong correlations exist among spatial measurements over long spatial distances. For illustration purposes, Figure 4.1 shows two material surfaces that demonstrate LRD along with their autocorrelation plots. Specifically, Figure 4.1 (a) shows a wood surface with an LRD effect along the vertical direction, and Figure 4.1 (b) shows a silver surface that exhibits the LRD effect along the horizontal direction. Figures 4.1 (c) and (d) show the autocorrelation functions (ACF) in absolute values for the wood surface along its vertical direction and the silver surface along its horizontal direction, respectively. It can be observed that both ACF plots demonstrate heavy tails beyond the exponentially fitted curves, which indicates the existence of LRD. In the literature, Richard [94] discovered such spatial LRD effect within the image texture of photomicrographs of non-printed silver gelatin photographic papers. Lee, et al. [95] illustrated that the height distributions of surfaces of plastic food wrappings possess the LRD effect. Rabiei, et al. [96] revealed the LRD effect on fetal cortical surfaces based on magnetic resonance images.

From the physical perspective, there are several mechanisms that can cause the spatial LRD. For instance, some material surfaces may demonstrate periodic textures or patterns, which can incur strong dependencies across long distances among periodic regions. Another example is that some surface defects, such as scratches or cracks, may demonstrate a strong correlation along the direction of the scratches/cracks. Due to the wide existence of spatial LRD, it is critical to build a spatial modeling and surface monitoring framework that integrates the LRD effect. Otherwise, inaccurate/erroneous surface anomaly detection and deteriorated manufacturing/production quality can be incurred when the spatial LRD actually presents.

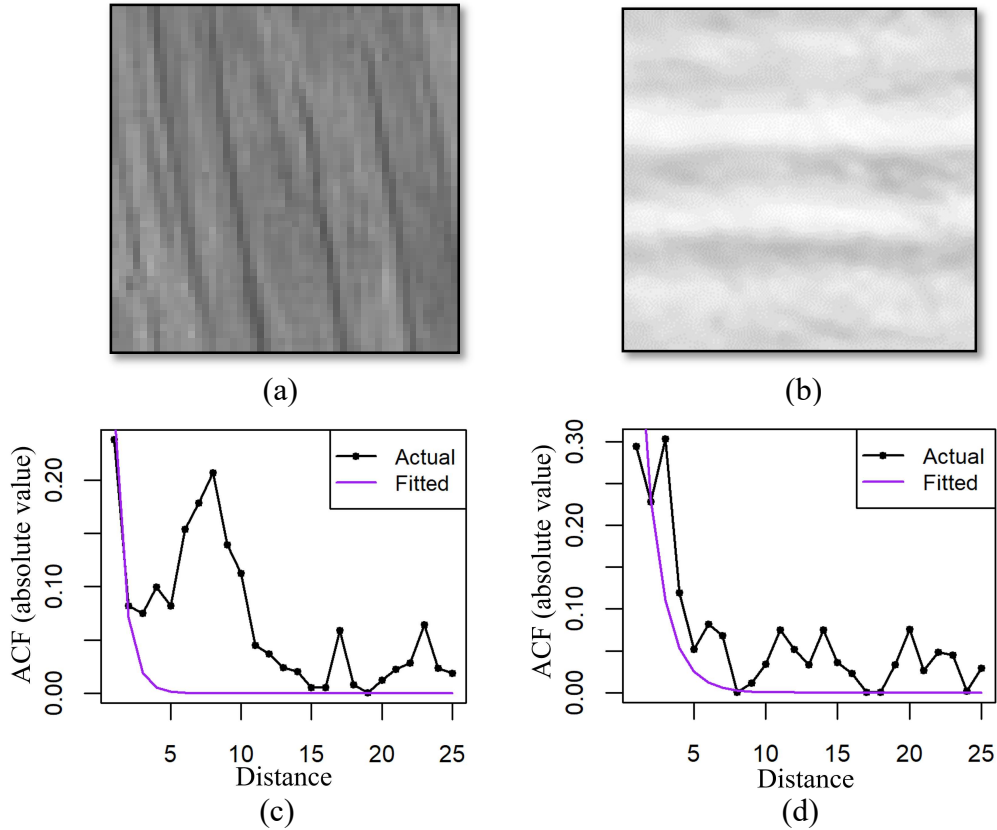


Figure 4.1. (a) A wood surface with the LRD effect along the vertical direction; (b) A silver surface with the LRD effect along the horizontal direction; (c) Autocorrelation (absolute value) function of the wood surface in the vertical direction, along with the fitted exponential curve; (d) Autocorrelation (absolute value) function of the silver surface in the horizontal direction, along with the fitted exponential curve.

4.1.2 Related Literature Review

For quality control of material surfaces, various image-based monitoring approaches have been proposed without considering the LRD effect. These approaches often first build a spatial model to characterize the surface distribution and extract a set of features (such as model parameters) from the surfaces. Subsequently, a quality control chart is developed to monitor the feature/parameter shift [26, 99]. When the parameter shift exceeds a control limit, anomalies of the surfaces can be detected. Therefore, in the following contexts a literature review is conducted on: (1) current spatial modeling approaches; and (2) major surface monitoring methods.

For spatial modeling of material surfaces, existing models can be broadly classified into three categories, i.e., physical models, statistical models, and artificial intelligence (AI) models.

(1) For physical models, Glaessgen, et al. [100] proposed a geometrical model integrated with a finite element method to characterize the surface structure of textile composites. Wang, et al. [101] developed a partial differential equation model to describe the microstructure of materials. Ran, et al. [102] developed a modified finite element approach to analyze the roughness of surfaces generated by multiple laser shock peening. For more physical models, one can refer to Xu, et al. [103], Matthews, et al. [104], Lu, et al. [105], etc. Although these physical models can characterize the complex structures and shapes of material surfaces to a certain degree, they usually require comprehensive physical/chemical information of the material formation, and they cannot well capture the random variation of material surfaces. (2) To further characterize the random variation and uncertainty, numerous statistical models have been proposed, among which the Kriging models are commonly used to describe material surfaces. For example, Mera [106] proposed an isotropic Kriging model to detect the size and location of subsurface cavities. To further capture spatial heterogeneities of material surfaces, Jin, et al. [107] developed an anisotropic Kriging model to characterize the geometric profile of wafers. Besides the Kriging models, Zhang and Yang [108] proposed a random effect autologistic regression model to characterize the microstructure images of dual-phase high-strength steel. Si, et al. [109] developed a distribution-based functional linear model for microstructure image modeling and reliability analysis. Valette and Rémy [110] proposed a wavelet-based multiresolution analysis method to model surfaces of 3D objects. Liu, et al. [111] developed an augmented layer-wise spatial log Gaussian Cox model to quantify the spatial distribution of pores in additively manufactured parts. However, these studies characterize the random variation of material surfaces with a correlation structure of limited orders, which can capture only the short-range dependence (SRD) with summable autocovariances. It should be mentioned that Zhang and Apley [112] developed a spatial model that can incorporate

an isotropic LRD effect for response surface interpolation. However, their model cannot capture the anisotropic spatial LRD effect, and they did not develop quality control analysis of material surfaces that incorporates the LRD effect. (3) In addition to the physical and statistical models, some AI approaches have also been developed to model material surfaces with a reduction of model assumptions and an improvement of the computational efficiency. For instance, Jia, et al. [113] developed a real-time visual inspection system for material surfaces based on a support vector machine. Huang, et al. [114] designed a real-time and multi-module neural network model called MCuePush U-Net for surface defect detection of magnetic tile. To classify surfaces of different materials, Zheng, et al. [115] proposed a convolutional neural network scheme with hybrid inputs. Mujeeb, et al. [116] developed a deep autoencoder network to detect surface defects of the hot-rolled steel. However, these AI-based studies typically lack statistical rigor and cannot be used to develop statistically efficient monitoring methods. As a result, although various Markovian and non-Markovian (SRD-based) methods have been proposed to describe material surfaces, most existing studies have not yet considered the spatial LRD effect, which could result in a biased surface characterization and eventually lead to surface anomaly misdetection.

For material surface monitoring, parametric, semi-parametric and non-parametric methods have been developed in the literature. In parametric methods, researchers commonly develop a specific parametric spatial model to characterize material surface measurements and reduce the data dimension to a small set of model parameters, based on which a multivariate control chart is established for monitoring purposes. For example, Colosimo [24] detected metal surface defects using a spatial autoregressive model with exogenous variables. Baek, et al. [25] developed a multimode nearest neighbor method for monitoring multimode surfaces based on a nonlinear spatial model. Wang, et al. [99] monitored the profiles of wafer thickness on the basis of

estimated model parameters of a spatial Gaussian-Kriging model. For semi-parametric methods, Bui and Apley [26] developed a semi-parametric autoregressive model to detect anomaly on textile surfaces. Lyu and Chen [27] constructed an automated vision inspection system to inspect anomalies using Hotelling's T^2 control chart. In addition to the parametric and semi-parametric methods, some non-parametric methods have also been proposed to monitor material surfaces. For instance, Qiu, et al. [28] proposed a nonparametric mixed-effect model to capture the spatial variance structure of materials and develop a quality control analysis based on the estimated variance structure. Ulker [29] conducted a surface quality control of fiber sandwich boards using surface roughness as a quality tool. For more surface quality control methods, one can refer to Jia, et al. [113], Yue, et al. [117], Du, et al. [118], etc. However, all the aforementioned monitoring methods ignore the LRD effect, which can result in poor surface anomaly detection if the spatial LRD actually presents.

4.1.3 Overview of the Proposed Work

To overcome the aforementioned challenges, in this chapter we propose a novel image-based spatial modeling and monitoring approach integrating the LRD effect. Specifically, both isotropic and anisotropic scenarios of the LRD-integrated spatial model are developed to handle various types of material surfaces on the basis of Lévy fractional Brownian random field (LFBRF) and fractional Brownian sheet (FBS), respectively. Based on the LRD-integrated spatial model, we develop a quality monitoring scheme of material surfaces that integrates the LRD effect using the generalized likelihood ratio test. Simulation studies and a real case study using wood surface images are conducted to illustrate the proposed model and demonstrate its superiority over conventional methods.

The remainder of this chapter is summarized as follows. In Section 4.2, a novel spatial model that integrates LRD is proposed, for both isotropic and anisotropic surface scenarios. In

Section 4.3, an LRD-integrated surface monitoring method is developed on the basis of the proposed spatial model. In Section 4.4, a simulation study is implemented to verify the proposed model. In Section 4.5, a real case study is conducted to demonstrate the performance and superiority of the proposed approach. Section 4.6 provides the conclusion and discusses future research topics.

4.2 An LRD-Integrated Spatial Model

As the preliminary step for material surface monitoring, in this section we propose a novel LRD-integrated spatial model to characterize the surface distribution while capturing the spatial LRD. In Section 4.2.1, we introduce the spatial LRD effect and its mathematical definition. In Sections 4.2.2 and 2.3.2.3, we propose the LRD-integrated spatial model under isotropic and anisotropic scenarios based on the LFBRF and FBS, respectively.

4.2.1 Preliminaries on the LRD Effect

The LRD effect, also referred to as the long-term memory or long memory, has been detected in both one-dimensional temporal data and two-dimensional spatial data. For the temporal data, LRD implies a slow decay of autocovariance/autocorrelation with heavy tails over the time lag so that temporal measurements are highly correlated across a long period of time. Mathematically, the LRD effect is defined as follows. Consider a stationary stochastic process $\{X(t)|t \geq 0\}$. The expectation of $X(t)$ is constant and satisfies $E(X(t)) = E(X(0))$. The autocovariance function of $X(t)$ satisfies:

$$\gamma_X(\tau) = Cov(X(t+\tau), X(t)) = Cov(X(\tau), X(0)); \tau \geq 0 \quad (55)$$

where $\gamma_X(\tau)$ only depends on the time lag τ between two measurements. $X(t)$ has the LRD effect if its autocovariance function satisfies $\sum_{u=0}^{+\infty} |\gamma_X(u)| = +\infty$, which indicates that the autocovariances are non-summable [84], and the ACF plot commonly demonstrates a heavy tail.

Note that when the autocovariances are summable, i.e., $\sum_{u=0}^{+\infty} |\gamma_X(u)| < +\infty$, $X(t)$ has the short-range dependence (SRD) effect. Equivalently, the temporal LRD effect can also be defined using the spectral density of $X(t)$ as follows:

$$s_X(\omega) = \frac{1}{2\pi} \int_{-\infty}^{+\infty} e^{-i\omega k} \gamma_X(k) dk; \quad \omega \in (-\pi, \pi] \quad (56)$$

where $i = \sqrt{-1}$ is the imaginary unit; and ω is the angular frequency. $X(t)$ exhibits the LRD effect if its spectral density $s_X(\omega)$ satisfies [84]:

$$s_X(\omega) \sim C_s |\omega|^\lambda, \quad \text{as } \omega \rightarrow 0 \quad (57)$$

where $C_s \in \mathbb{R}_+$ and $\lambda \in (-1, 0)$ are two constants. A common example of stochastic processes that exhibits the LRD is the fractional Brownian motion with a Hurst parameter $H \in (0.5, 1)$ [48].

For spatial or image data, the spatial LRD effect refers to the slowly decaying autocovariance over spatial distance such that measurements are highly correlated across long spatial distances. Specifically, the spatial LRD can be classified into two cases, i.e., isotropic and anisotropic spatial LRD. Consider a stationary random field defined on a two-dimensional space, $\{Y(x_1, x_2) | (x_1, x_2) \in \mathbb{R}^2\}$, where (x_1, x_2) denotes the coordinate on the two-dimensional space \mathbb{R}^2 . The expectation of $Y(x_1, x_2)$ satisfies $E(Y(x_1, x_2)) = E(Y(0, 0))$, and the autocovariance function of $Y(x_1, x_2)$ satisfies:

$$\gamma_Y(u_1, u_2) = \text{Cov}(Y(x_1 + u_1, x_2 + u_2), Y(x_1, x_2)) = \text{Cov}(Y(u_1, u_2), Y(0, 0)); u_1, u_2 \in R \quad (58)$$

In Equation (58), $\gamma_Y(u_1, u_2)$ only depends on the spatial lags u_1 and u_2 . Based on $\gamma_Y(u_1, u_2)$, the spectral density of $Y(x_1, x_2)$ can be calculated as:

$$s_Y(\omega_1, \omega_2) = \left(\frac{1}{2\pi}\right)^2 \int_{-\infty}^{+\infty} \int_{-\infty}^{+\infty} e^{-i\omega_1 k - i\omega_2 l} \gamma_Y(k, l) dk dl; \omega_1, \omega_2 \in (-\pi, \pi] \quad (59)$$

where ω_1 and ω_2 are angular frequencies along the directions of x_1 and x_2 , respectively. Specifically, $Y(x_1, x_2)$ possesses an isotropic LRD effect if its spectral density satisfies [119]:

$$s_Y(\omega_1, \omega_2) \sim D \sqrt{\omega_1^2 + \omega_2^2}^\rho, \text{ as } \omega_1, \omega_2 \rightarrow 0 \quad (60)$$

where $D \in R_+$ and $\rho \in (-2, 0)$ are constants. In Equation (60), the spectral density $s_Y(\omega_1, \omega_2)$ only depends on the magnitude of the vector (ω_1, ω_2) , and the direction of the vector (ω_1, ω_2) does not have any effect on $s_Y(\omega_1, \omega_2)$. Therefore, this type of spatial LRD is called the isotropic LRD.

Besides the isotropic LRD, the random field $Y(x_1, x_2)$ is called to be anisotropic long-range dependent if its spectral density satisfies [119]:

$$s_Y(\omega_1, \omega_2) \sim C_1 |\omega_1|^{\lambda_1} C_2 |\omega_2|^{\lambda_2}, \text{ as } \omega_1, \omega_2 \rightarrow 0 \quad (61)$$

where $C_1, C_2 \in R_+$ and $\lambda_1, \lambda_2 \in (-1, 0)$ are constants. Compared to the isotropic LRD, in Equation (61) it can be observed that the spectral density $s_Y(\omega_1, \omega_2)$ not only depends on the magnitude of vector (ω_1, ω_2) but also relates to the direction of vector (ω_1, ω_2) . For example, vectors (1,2) and (2,1) share a common magnitude but demonstrate two different directions. Their corresponding spectral density values are $C_1 C_2 2^{\lambda_2}$ and $C_1 C_2 2^{\lambda_1}$, respectively, which are different when $\lambda_1 \neq \lambda_2$.

Therefore, this type of spatial LRD is termed as the anisotropic LRD.

4.2.2 The Isotropic LRD-Integrated Spatial Model

For many real-life cases, material surfaces demonstrate an isotropic topology that is independent of the directions [120]. To model such material surfaces, we propose an isotropic LRD-integrated spatial model on the basis of the LFBRF [121]. Specifically, we decompose a material surface structure into a deterministic component that models the fixed spatial trend/pattern and a stochastic component that captures the random variation embedded with LRD. Consider a spatial measurement collection on N locations/points of a surface, denoted as $\{(x_i, y_i) \in R^2 | i \in 1, 2, \dots, N\}$, where (x_i, y_i) is the coordinate of the i th measurement point. We propose an isotropic LRD-integrated spatial model for a material surface as follows:

$$z(x_i, y_i) = \alpha f(x_i, y_i | \boldsymbol{\theta}_f) + \sigma B_H(x_i, y_i); i \in 1, 2, \dots, N \quad (62)$$

In model (62), $z(x_i, y_i)$ is a response variable of interest that is measured at location (x_i, y_i) . For example, it can be the height of a surface point if the goal is to model surface roughness, and it can be the material density of a surface location if the goal is to study surface density distribution. $\alpha f(x, y | \boldsymbol{\theta}_f)$ is a spatial trend component to model the tendency of the material surface with parameters α and $\boldsymbol{\theta}_f$. Examples of isotropic trend structures include a constant used for homogeneous surfaces with uniform properties and periodic trends for certain textures. $\sigma B_H(x, y)$ models the random variation component of material surfaces. σ is a diffusion parameter and controls the scale of the surface variation. $B_H(x, y)$ is called an LFBRF with a Hurst parameter $H \in (0, 1)$.

More specifically, in the proposed model (62) the LFBRF term, $B_H(x, y)$, can capture the LRD effect within isotropic surfaces. $B_H(x, y)$ is defined in a two-dimensional stochastic integral form as follows [121]:

$$B_H(x, y) = \int_{\mathbb{R}^2} \left(\|(x, y) - (k, l)\|^{H-1} - \|(k, l)\|^{H-1} \right) dW(k, l) \quad (63)$$

where $\|(x, y)\| = \sqrt{x^2 + y^2}$ represents the L₂ norm of vector (x, y) ; and $W(k, l)$ is a white noise process defined in a two-dimensional space. The LFBRF is a type of Gaussian random field with a mean of zero and a covariance function as:

$$\text{Cov}(B_H(x_i, y_i), B_H(x_j, y_j)) = \frac{1}{2} \left((x_i^2 + y_i^2)^H + (x_j^2 + y_j^2)^H - ((x_i - x_j)^2 + (y_i - y_j)^2)^H \right) \quad (64)$$

In $B_H(x, y)$, the Hurst parameter H controls the spatial dependence structure. When $H \in (0.5, 1)$, the increments of $B_H(x, y)$ exhibit the LRD effect [122]; and when $H = 0.5$, $B_H(x, y)$ degenerates to the Lévy Brownian random field. Besides the LRD effect, $B_H(x, y)$ also exhibits the following properties [121]: i) $B_H(0, 0) = 0$; ii) $B_H(x, y)$ has stationary increments, i.e.,

$B_H(x + \Delta x, y + \Delta y) - B_H(x, y) \stackrel{d}{=} B_H(\Delta x, \Delta y)$, where $\stackrel{d}{=}$ denotes equivalence in distribution;

iii) $B_H(x, y)$ is operator self-similar, which indicates $B_H(ax, ay) \stackrel{d}{=} a^H B_H(x, y)$ for $a > 0$; and

iv) the variance of $B_H(x, y)$ satisfies $\text{Var}(B_H(x, y)) = (x^2 + y^2)^H$.

4.2.3 The Anisotropic LRD-Integrated Spatial Model

Besides the isotropic scenario, the surfaces of numerous manufactured parts are more complex and exhibit an anisotropic property [123]. For example, the surface profile of a metal part

may demonstrate different patterns in the rolling direction and the transverse direction. The wood surface structure as depicted in Figure 4.1 (a) demonstrates a texture along the vertical direction. Under such circumstances, we propose an anisotropic LRD-integrated model that can capture the heterogeneity of the spatial LRD effect at different directions. Specifically, we propose an FBS-based spatial model for anisotropic material surfaces as follows:

$$z(x_i, y_i) = \alpha f(x_i, y_i | \boldsymbol{\theta}_f) + \sigma B_{H_x, H_y}(x_i, y_i); i \in 1, 2, 3, \dots, N \quad (65)$$

where $B_{H_x, H_y}(x, y)$ is the standard FBS [121] defined in a two-dimensional space with horizontal and vertical Hurst parameters $H_x, H_y \in (0, 1)$. Other terms are similar to those defined in model (62).

In model (65), $B_{H_x, H_y}(x, y)$ captures the anisotropic LRD effect and can be represented in a stochastic integral form as [121]:

$$B_{H_x, H_y}(x, y) = \int_{\mathbf{R}^2} \left(|x-k|^{H_x-1/2} - |k|^{H_x-1/2} \right) \left(|y-l|^{H_y-1/2} - |l|^{H_y-1/2} \right) dW(k, l) \quad (66)$$

$B_{H_x, H_y}(x, y)$ is a special type of Gaussian random fields. It has a mean of zero and a covariance function as follows:

$$\text{Cov}\left(B_{H_x, H_y}(x_i, y_i), B_{H_x, H_y}(x_j, y_j)\right) = \frac{1}{4} \left(x_i^{2H_x} + x_j^{2H_x} - |x_i - x_j|^{2H_x} \right) \left(y_i^{2H_y} + y_j^{2H_y} - |y_i - y_j|^{2H_y} \right) \quad (67)$$

where the Hurst parameters H_x and H_y determine the anisotropic dependence structure of the proposed spatial model along the two directions. In Appendix A5, we show that when $H_x \in (0.5, 1)$ or $H_y \in (0.5, 1)$, the proposed spatial model can capture the anisotropic spatial LRD effect for the x or y direction, respectively. In addition to the LRD effect, $B_{H_x, H_y}(x, y)$ holds the following

properties: i) $B_{H_x, H_y}(x, 0) = B_{H_x, H_y}(0, y) = 0$; ii) B_{H_x, H_y} has stationary increments, i.e.,

$$B_{H_x, H_y}(x + \Delta x, y + \Delta y) - B_{H_x, H_y}(x, y) \stackrel{d}{=} B_{H_x, H_y}(\Delta x, \Delta y);$$

iii) $B_{H_x, H_y}(x, y)$ is operator self-similar, which indicates $B_{H_x, H_y}(ax, ay) \stackrel{d}{=} a^{H_x + H_y} B_{H_x, H_y}(x, y)$ for $a > 0$; and iv) the variance of

$$B_{H_x, H_y}(x, y) \text{ can be calculated as } \text{Var}(B_{H_x, H_y}(x, y)) = x^{2H_x} y^{2H_y}.$$

4.3 LRD-Integrated Surface Monitoring

Based on the proposed spatial model, we develop an LRD-integrated surface monitoring method using the framework of the generalized likelihood ratio test (GLRT). The GLRT principle has been widely applied to develop quality control charts of various products [26, 124, 125]. Specifically, we first apply the proposed LRD-integrated spatial model to characterize material surface measurements and extract surface features (i.e., model parameters). Using the features as inputs, a GLRT-based monitoring method is established. In Section 4.3.1, we develop a maximum likelihood estimation (MLE) approach to estimate in-control surface parameters as features. In Section 4.3.2, we establish a GLRT-based monitoring framework to monitor material surface change.

4.3.1 In-Control Surface Parameters Identification

To detect the anomaly/change on material surfaces, the features of the surfaces need to be extracted to construct a monitoring statistic. We apply the proposed LRD-integrated spatial model to obtain the surface features, as represented by the estimated model parameters. The model parameters are summarized as $\{(H, \sigma^2, \alpha, \boldsymbol{\eta}_f)\}^T$ for isotropic scenario; $\{(H_x, H_y, \sigma^2, \alpha, \boldsymbol{\eta}_f)\}^T$ for anisotropic scenario}. Herein, H and $\{H_x, H_y\}$ characterize the LRD structure under the isotropic and anisotropic scenarios, respectively; σ^2 characterizes the

magnitude of surface variation; α characterizes the magnitude of the surface trend; and $\boldsymbol{\eta}_f$ relates to the global pattern of the surface trend. Therefore, a material surface change can be characterized by the change of $\boldsymbol{\theta}$.

To estimate $\boldsymbol{\theta}$, we develop an MLE approach. Given the measurement collection of a material surface denoted as $\mathbf{z} = (z(x_1, y_1), z(x_2, y_2), \dots, z(x_N, y_N))$, based on the proposed isotropic model (62) and the anisotropic model (65) the log-likelihood function is constructed as follows:

$$l(\boldsymbol{\theta}|\mathbf{z}) = -\frac{N}{2}\ln(2\pi) - \frac{N}{2}\ln(\sigma^2) - \frac{1}{2}\ln|\mathbf{C}| - \frac{(\mathbf{z} - \alpha\mathbf{f})^T \mathbf{C}^{-1}(\mathbf{z} - \alpha\mathbf{f})}{2\sigma^2} \quad (68)$$

where $\mathbf{f} = (f(x_1, y_1), f(x_2, y_2), \dots, f(x_N, y_N))$; \mathbf{C} is the covariance matrix that is calculated via Equation (64) for the isotropic model and Equation (67) for the anisotropic model, respectively. Using M in-control images $\{\mathbf{z}_1, \mathbf{z}_2, \dots, \mathbf{z}_M\}$, the log-likelihood function with respect to $\boldsymbol{\theta}$ is constructed based on (68) as follows:

$$l(\boldsymbol{\theta}|\{\mathbf{z}_1, \mathbf{z}_2, \dots, \mathbf{z}_M\}) = -\frac{MN}{2}\ln(2\pi) - \frac{MN}{2}\ln(\sigma^2) - \frac{M}{2}\ln|\mathbf{C}| - \frac{\sum_{i=1}^{i=M} (\mathbf{z}_i - \alpha\mathbf{f})^T \mathbf{C}^{-1}(\mathbf{z}_i - \alpha\mathbf{f})}{2\sigma^2} \quad (69)$$

$\boldsymbol{\theta}$ can be obtained via maximizing the log-likelihood function (69) with respect to $\boldsymbol{\theta}$, i.e.,

$$\hat{\boldsymbol{\theta}} = \arg \max_{\boldsymbol{\theta}} \{l(\boldsymbol{\theta}|\{\mathbf{z}_1, \mathbf{z}_2, \dots, \mathbf{z}_M\})\} \quad (70)$$

Let $\boldsymbol{\theta}^*$ denote the collection of parameters in addition to α and σ^2 , i.e., $\boldsymbol{\theta}^* = (H, \boldsymbol{\eta}_f)$ for the isotropic scenario and $\boldsymbol{\theta}^* = (H_x, H_y, \boldsymbol{\eta}_f)$ for the anisotropic scenario. To maximizing the log-likelihood function (69), we derive the closed-form MLE estimators of parameters α and σ^2 conditional on $\boldsymbol{\theta}^*$, by taking the partial derivatives of $l(\boldsymbol{\theta}|\{\mathbf{z}_1, \mathbf{z}_2, \dots, \mathbf{z}_M\})$ with respect to α and σ^2 , respectively, and then setting the partial derivatives to zero. The results are summarized in

Proposition 4.1.

Proposition 4.1. The closed-form MLE estimators of α and σ^2 are as follows:

$$\hat{\alpha} = \frac{\sum_{i=1}^{i=M} \mathbf{z}_i^T \mathbf{C}^{-1} \mathbf{f}}{M \mathbf{f}^T \mathbf{C}^{-1} \mathbf{f}}; \quad \hat{\sigma}^2 = \frac{\sum_{i=1}^{i=M} \mathbf{z}_i^T \mathbf{C}^{-1} \mathbf{z}_i}{MN} - \frac{\left(\sum_{i=1}^{i=M} \mathbf{z}_i^T \mathbf{C}^{-1} \mathbf{f} \right)^2}{M^2 \mathbf{f}^T \mathbf{C}^{-1} \mathbf{f}} \quad (71)$$

Substituting Equation (71) into the log-likelihood function (69), we obtain the profile log-likelihood function as

$$l(\boldsymbol{\theta}^* | \{\mathbf{z}_1, \mathbf{z}_2, \dots, \mathbf{z}_M\}) = \frac{MN}{2} (-\ln(2\pi) - 1) - \frac{M}{2} \ln |\mathbf{C}| - \frac{MN}{2} \ln \left(\frac{\sum_{i=1}^{i=M} \mathbf{z}_i^T \mathbf{C}^{-1} \mathbf{z}_i}{MN} - \frac{\left(\sum_{i=1}^{i=M} \mathbf{z}_i^T \mathbf{C}^{-1} \mathbf{f} \right)^2}{M^2 \mathbf{f}^T \mathbf{C}^{-1} \mathbf{f}} \right) \quad (72)$$

The parameters $\boldsymbol{\theta}^*$ are estimated via maximizing the profile log-likelihood function with respect to $\boldsymbol{\theta}^*$, i.e., $\hat{\boldsymbol{\theta}}^* = \arg \max_{\boldsymbol{\theta}^*} \{l(\boldsymbol{\theta}^* | \{\mathbf{z}_1, \mathbf{z}_2, \dots, \mathbf{z}_M\})\}$. Based on the point estimates of parameters $\boldsymbol{\theta}^*$, the point estimates of parameters α_0 and σ_0^2 can be estimated via Equation (71). Note that the profile log-likelihood function (72) involves the calculation of the inverse and determinant of matrix \mathbf{C} , and the computational complexity becomes high when the sample size N becomes large. To handle this issue, an efficient method based on Cholesky decomposition is used to calculate \mathbf{C}^{-1} and $|\mathbf{C}|$ [126]. In addition to the point estimation of $\boldsymbol{\theta}$, we also develop an interval estimation approach of $\boldsymbol{\theta}$ that can characterize the uncertainty of parameter estimation, which is summarized in Appendix A6.

4.3.2 A GLRT-based Surface Monitoring Framework

Given a sample of in-control surface data $\{\mathbf{z}_1, \mathbf{z}_2, \dots, \mathbf{z}_M\}$ collected in Phase I, the in-control parameters are estimated using the developed MLE approach in Section 4.3.1. In Phase II, we determine whether a new surface K is in-control or out-of-control using the GLRT. Let $\boldsymbol{\theta}_K$ and

$\boldsymbol{\theta}_0$ denote the model parameters of surface K and in-control parameters, respectively. Herein, $\boldsymbol{\theta}_0 = (H_0, \sigma_0^2, \alpha_0^2, \boldsymbol{\eta}_{f0})$ for the isotropic scenario, and $\boldsymbol{\theta}_0 = (H_{x0}, H_{y0}, \sigma_0^2, \alpha_0^2, \boldsymbol{\eta}_{f0})$ for the anisotropic scenario. If $\boldsymbol{\theta}_K$ deviates from the in-control parameters $\boldsymbol{\theta}_0$, then surface K will be considered as out-of-control. Therefore, to monitor material surface change the following null and alternative hypotheses are constructed:

$$H_0: \boldsymbol{\theta}_K = \boldsymbol{\theta}_0 \quad H_1: \boldsymbol{\theta}_K \neq \boldsymbol{\theta}_0 \quad (73)$$

In the GLRT framework, using the estimated parameters as inputs, a monitoring statistic W is constructed as follows:

$$W = 2 \left(l_K(\widehat{\boldsymbol{\theta}}_K | \mathbf{z}_K) - l_0(\widehat{\boldsymbol{\theta}}_0 | \mathbf{z}_K) \right) / N_K \quad (74)$$

where \mathbf{z}_K is the collection of measurements on surface K ; N_K is the number of measurements on surface K ; $l_K(\widehat{\boldsymbol{\theta}}_K | \mathbf{z}_K)$ is the maximum likelihood value given \mathbf{z}_K ; and $l_0(\widehat{\boldsymbol{\theta}}_0 | \mathbf{z}_K)$ denotes the likelihood value evaluated at $\widehat{\boldsymbol{\theta}}_0$ given \mathbf{z}_K . By substituting $\widehat{\boldsymbol{\theta}}_0$ and $\widehat{\boldsymbol{\theta}}_K$ into Equation (74), we obtain the monitoring statistic W for material surfaces as

$$W = \ln \left(\frac{\widehat{\sigma}_0^2}{\widehat{\sigma}_K^2} \right) + \frac{1}{N_K} \ln \frac{|\mathbf{C}_0|}{|\mathbf{C}_K|} + \frac{(\mathbf{z} - \widehat{\alpha}_0 \mathbf{f})^T \mathbf{C}_0^{-1} (\mathbf{z} - \widehat{\alpha}_0 \mathbf{f})}{2N_K \widehat{\sigma}_0^2} - \frac{(\mathbf{z} - \widehat{\alpha}_K \mathbf{f})^T \mathbf{C}_K^{-1} (\mathbf{z} - \widehat{\alpha}_K \mathbf{f})}{2N_K \widehat{\sigma}_K^2} \quad (75)$$

where \mathbf{C}_0 and \mathbf{C}_K are the covariance matrices given $\widehat{\boldsymbol{\theta}}_0$ and $\widehat{\boldsymbol{\theta}}_K$, respectively.

To monitor changes in material surface, both the upper control limit (UCL) and lower control limit (LCL) of the monitoring statistic W need to be determined. Given the distribution of W , denoted as $F(w)$, the UCL and LCL under a significance level of q are constructed as follows:

$$UCL = Q_{1-q}(F(w)); \quad LCL = 0 \quad (76)$$

where $Q_p(F(w))$ denotes the p -quantile of $F(w)$. In most real cases, the theoretical distribution of W is difficult to derive due to model complexity. Therefore, we approximate the theoretical distribution of W by the empirical distribution based on the monitoring statistics of n in-control surfaces $\{W_1, W_2, \dots, W_n\}$, which can result in a good approximation when the sample size is large, i.e., $n \gg q^{-1}$.

In some practical scenarios, the sample size of images may not be sufficiently large due to expensive and time-consuming experiments. To handle this issue, we can approximate the monitoring statistic using $W = t + r\chi_k^2$, where χ_k^2 represents a chi-squared random variable with k degrees of freedom; and t and r are two constants. Herein, k , t and r can be estimated using the method of moments described in Bui and Apley [26]. Therefore, the control limits at the significance level of q can be constructed as follows:

$$\text{UCL} = \hat{t} + \hat{r}Q_{1-q}(\chi_{\hat{k}}^2); \quad \text{LCL} = 0 \quad (77)$$

where $Q_{1-q}(\chi_{\hat{k}}^2)$ denotes the x -quantile of a chi-squared distribution with k degrees of freedom.

Note that the GLRT framework is selected in this chapter to construct an LRD-integrated quality control charts for illustration purposes. Other commonly used quality control frameworks, such as the multivariate EWMA charts [127], the kernel-distance based control charts [128] and the multivariate CUMSUM charts [129], can also be adapted to the proposed LRD-integrated spatial model in a similar way to construct various types of LRD-integrated quality control charts.

4.4 Simulation Study

To evaluate the performance of the proposed LRD-integrated spatial model and the surface monitoring framework, we conduct simulation studies under both isotropic and anisotropic scenarios, as presented in Section 4.4.1 and Section 4.4.2, respectively.

4.4.1 Isotropic Scenario

4.4.1.1 Data Simulation

To assess the proposed isotropic spatial model and surface monitoring performance, a set of isotropic material surfaces with LRD are simulated. For illustration purposes, an isotropic trend term $\alpha(x^2 + y^2)$ is selected, and the surfaces are simulated using the following model (termed as M_1):

$$M_1: z(x, y) = \alpha(x^2 + y^2) + \sigma B_H(x, y) \quad (78)$$

The model parameters are $\theta = (H, \sigma^2, \alpha)$. In the simulation, for the in-control surfaces we set $\theta = (H, \sigma^2, \alpha) = (0.7, 1, 0.1)$. For the out-of-control surfaces we consider three settings with slight shifts of the in-control parameters and two settings with contraction of the in-control surface images to test the sensitivity of the proposed monitoring method. These settings are listed in Table 4-1. These parameter shifting and image contraction schemes have been widely adopted in SPC literature to generate out-of-control images [26, 99].

Table 4-1. Five Settings of Out-of-control Surfaces

Parameters	Setting 1	Setting 2	Setting 3	Setting 4	Setting 5
H	0.75	0.7	0.7	Contracted	Contracted
σ^2	1	1.1	1	vertically by	horizontally
α	0.1	0.1	0.11	10%	by 10%

Using the specified model parameters, 600 in-control surface images with a size of 30×30 pixels are simulated via Algorithm 4.1, and 500 images of out-of-control surfaces are simulated under each out-of-control setting in Table 4-1. For illustration purposes, we show an in-control surface and two out-of-control surfaces of Settings 1 and 4 in Figure 4.1. It can be observed that these surfaces demonstrate an isotropic effect with respect to the origin $(0,0)$, and it is visually difficult to distinguish those changes.

Algorithm 4.1. An LFBRF-based surface simulation method with isotropic LRD

Step 1. Simulate the trend term $\alpha \mathbf{f}$ based on trend function $\alpha f(x, y) = \alpha(x^2 + y^2)$.

Step 2. Simulate the LFBRF, i.e., \mathbf{B}_H , using the specified model parameters

$$\boldsymbol{\theta} = (H, \sigma, \alpha).$$

2.1. Calculate the covariance matrix \mathbf{Q} on N measurement points

$\{(x_1, y_1), (x_2, y_2), \dots, (x_N, y_N)\}$ via Equation (64) as follows:

$$\mathbf{Q} = \begin{pmatrix} \text{Cov}((x_1, y_1), (x_1, y_1)) & \dots & \text{Cov}((x_1, y_1), (x_N, y_N)) \\ \vdots & \ddots & \vdots \\ \text{Cov}((x_N, y_N), (x_1, y_1)) & \dots & \text{Cov}((x_N, y_N), (x_N, y_N)) \end{pmatrix}$$

2.2 Perform the Cholesky decomposition to covariance matrix \mathbf{Q} , denoted as

$$\mathbf{Q} = \mathbf{L}\mathbf{L}^T, \text{ where } \mathbf{L} \text{ is a lower triangular matrix.}$$

2.3 Simulate the response value of LFBRF \mathbf{B}_H on

$\{(x_1, y_1), (x_2, y_2), \dots, (x_N, y_N)\}$:

2.3.1 Generate an N -dimensional Gaussian white noise \mathbf{b} , via

$$\mathbf{b} \sim \text{MVN}(\mathbf{0}, \mathbf{I}_N)$$

2.3.2 Calculate the response value of LFBRF \mathbf{B}_H following

$$\mathbf{B}_H = \mathbf{L}\mathbf{b}.$$

Step 3. Obtain the simulated surface with isotropic LRD effect as $\mathbf{z} = \alpha \mathbf{f} + \sigma \mathbf{B}_H$.

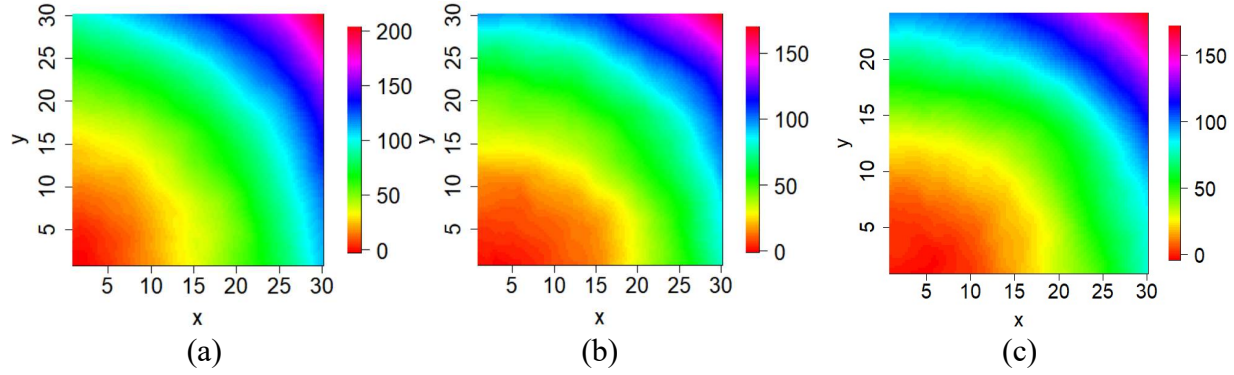


Figure 4.2. (a) In-control surface; (b) Out-of-control surface under Setting 1; (c) Out-of-control surface under Setting 4

4.4.1.2 Parameter Estimation

The simulated material surface images are then analyzed using the proposed isotropic model M_1 . The model parameters and corresponding standard errors are estimated via the MLE approach developed in Section 4.3.1. For illustration purposes, we show the estimation results for the first five samples of in-control surfaces in Table 4-2. It can be seen that the estimated model parameters are all close to the pre-specified values, which demonstrates a good performance of the MLE approach under the current image size.

Table 4-2. The Point Estimates and Standard Errors of M_1 Parameters

Setting	Parameters	Actual Value	1st Sample	2nd Sample	3rd Sample	4th Sample	5th Sample
in-control	H	0.7	0.695	0.723	0.731	0.703	0.697
	$se(H)$	—	0.0346	0.0338	0.0350	0.0334	0.0337
	σ^2	1	1.11	1.02	1.06	0.949	0.990
	$se(\sigma^2)$	—	0.0917	0.0951	0.107	0.789	0.0810
	α	0.1	0.0993	0.101	0.0994	0.0981	0.102
	$se(\alpha)$	—	0.000880	0.000593	0.000104	0.000113	0.000116

To further evaluate the performance of the MLE approach, we repeat the simulation process of isotropic in-control surfaces for 500 iterations under different surface image sizes (P), i.e., $P = 20 \times 20$, 30×30 and 40×40 . The root mean square errors (RMSEs) of parameter estimates are computed under each surface size. The RMSE of a parameter $\theta_i \in \boldsymbol{\theta}$ is calculated as

$$RMSE(\hat{\theta}_i) = \text{sqr}t\left(\sum_{q=1}^M (\theta_i - \hat{\theta}_{i,q})^2 / M\right), \text{ where } \hat{\theta}_{i,q} \text{ denotes the estimate of } \theta_i \text{ in the } q\text{th iteration.}$$

Table 4-3 lists the RMSEs under different image sizes, which shows that the RMSEs decrease as the sample size increases for all the parameters. This implies that a larger surface contains more information and therefore results in more accurate parameter estimation. The results further demonstrate the good performance of the developed MLE approach.

Table 4-3. RMSEs of Parameter Estimation of M_1 under Different Image Sizes

Sample Size	$RMSE(\hat{H})$	$RMSE(\hat{\sigma}^2)$	$RMSE(\hat{\alpha})$
20×20	0.0498	0.133	0.00892
30×30	0.0353	0.0955	0.00533
40×40	0.0278	0.0781	0.00378

4.4.1.3 Surface Anomaly Detection

Based on the estimated model parameters, a quality control analysis on surface change detection is conducted using the GLRT-based control chart developed in Section 4.3. To evaluate the performance of the LRD-integrated surface monitoring method, the average run length (ARL) is calculated. The ARL (including ARL_0 and ARL_1) is define as follows:

$$\begin{cases} ARL_0 = E(\text{number of samples until a control chart signals} | \text{the process is in-control}) \\ ARL_1 = E(\text{number of samples until a control chart signals} | \text{the process is out-of-control}) \end{cases} \quad (79)$$

Since the GLRT chart is a Shewhart type control chart, ARL_1 is calculated as the reciprocal of the detection power in this chapter.

Specifically, 100 in-control surfaces are selected to estimate the in-control model parameters, which are $\hat{\theta}_0 = (\hat{H}_0, \hat{\sigma}_0^2, \hat{\alpha}_0) = (0.698, 0.992, 0.0998)$. Based on the in-control parameters, the remaining 500 in-control surfaces are chosen to obtain the UCL and LCL of the monitoring statistic under a significance level of $q = 0.0027$, which corresponds to a nominal ARL_0 of 370. We apply the approximation method of the monitoring statistic illustrated in Section

4.3.3, and the constants (t, r, k) are estimated as $(-8.09 \times 10^{-4}, 7.67 \times 10^{-4}, 5.17)$. For each of the five out-of-control parameter settings, 500 surfaces are used to study the surface quality control performance.

The ARL_1 for model M_1 under the five out-of-control settings are computed and listed in Table 4-4. Results show that the proposed model achieves small ARL_1 under all out-of-control parameter settings, which indicates that the proposed model and monitoring method can detect surface change quickly when the surface is out-of-control at the current shift size of model parameters.

Table 4-4. Detection Power and ARL_1 for Model M_1 under Five Out-of-control Settings at $q = 0.0027$

Model	Metric	Setting 1	Setting 2	Setting 3	Setting 4	Setting 5
M_1	ARL_1	1.961	6.097	7.042	1.002	1.000

4.4.1.4 Model Comparison

To illustrate the superiority of the proposed model, we compare M_1 with three models from the literature that do not consider LRD, i.e., an isotropic Kriging model [130], a Lévy Brownian random field-based spatial model [131], and a nonlinear autoregressive model [26], which are respectively presented as follows:

$$\begin{cases} M_2 : z(x, y) = \alpha(x^2 + y^2) + \sigma G_I(x, y) \\ M_3 : z(x, y) = \alpha(x^2 + y^2) + \sigma B_L(x, y) \\ M_4 : z(x, y) = f(\mathbf{z}^{(x,y)}) + \varepsilon; \varepsilon \sim N(0, d^2) \end{cases} \quad (80)$$

Specifically, in model M_2 , $G_I(x, y)$ represents an isotropic Gaussian random field with a mean of zero and a covariance function $Cov(G_I(x_i, y_i), G_I(x_j, y_j))_{uv} = \exp\left(-s\left(\left(x_i - x_j\right)^2 + \left(y_i - y_j\right)^2\right)\right)$,

where s is a scale parameter. In model M_3 , $B_L(x, y)$ is the Lévy Brownian random field (LBRF),

which is a special case of the Lévy fractional Brownian random field when $H=0.5$. Model M_4 is a nonlinear autoregressive model developed by Bui and Apley [26], where $\mathbf{z}^{(x,y)}$ are the neighboring measurements of (x, y) ; and ε is the measurement error of a normal distribution with the mean of zero and the standard deviation of d^2 . Since Model M_4 only considers the correlation between neighboring measurements to a limited order, it cannot capture the LRD effect. We then apply $M_2 \sim M_4$ to analyze the simulated surfaces and conduct surface anomaly detection under the significant level $q = 0.0027$. Table 4-5 lists values of ARL_1 calculated using models $M_1 \sim M_3$ under five settings of out-of-control surfaces. It is observed that the proposed M_1 model achieves the lowest ARL_1 under all five out-of-control settings. Model M_3 performs the second best as a special scenario of M_1 . Model M_4 has the lowest performance since it only considers the neighborhood dependency, while the LRD actually presents. These results imply that the proposed model and monitoring method can much more promptly detect surface anomaly when the process goes out-of-control than the conventional models $M_2 \sim M_4$. Therefore, integrating the LRD effect significantly improves the performance of surface anomaly detection.

Table 4-5. ARL_1 of $M_1 \sim M_4$ under Five Out-of-control Settings at $q = 0.0027$

Model	Metric	Setting 1	Setting 2	Setting 3	Setting 4	Setting 5
M_1	ARL_1	1.961	6.097	7.042	1.002	1.000
M_2	ARL_1	100.0	83.33	50.00	25.00	27.78
M_3	ARL_1	16.13	31.25	7.813	1.859	1.901
M_4	ARL_1	166.67	166.67	250	125.0	166.7

4.4.2 Anisotropic Scenario

4.4.2.1 Data Simulation

Besides the isotropic scenario, a simulation study using anisotropic surfaces is conducted to assess the proposed anisotropic model and monitoring framework. We apply the following anisotropic model to simulate material surfaces:

$$M_5 : z(x, y) = \alpha(x + y) + \sigma B_{H_x, H_y}(x, y) \quad (81)$$

In M_5 , a linear term $\alpha(x + y)$ is used to impose an anisotropy of the trend on surfaces for illustration purposes. The model parameters are specified as $\boldsymbol{\theta} = (H_x, H_y, \sigma^2, \alpha) = (0.7, 0.8, 0.1, 10)$ in the simulation of in-control surfaces. For out-of-control surfaces, six different settings are set and summarized in Table 4-6.

Table 4-6. Six Settings of Out-of-control Surfaces

Parameters	Setting 1	Setting 2	Setting 3	Setting 4	Setting 5	Setting 6
H_x	0.75	0.7	0.7	0.7		
H_y	0.8	0.85	0.8	0.8	Contracted vertically by 10%	Contracted horizontally by 10%
σ^2	0.1	0.1	0.11	0.1		
α	10	10	10	10.2		

Based on the specified model parameters, we simulate 600 in-control surfaces and 500 out-of-control surfaces under each setting via Algorithm 4.2. The size of simulated surface images is 30×30 pixels. For illustration purposes, we show one in-control surface and two out-of-control surfaces under Settings 1 and 5 in Figure 4.3. These surfaces clearly demonstrate an anisotropic effect.

Algorithm 4.2. An FBS-based surface simulation approach with anisotropic LRD

Step 1. Calculate the trend term αf following $\alpha f(x, y) = \alpha(x + y)$.

Step 2. Simulate \mathbf{B}_{H_x, H_y} using the specified $\boldsymbol{\theta} = (H_x, H_y, \sigma^2, \alpha)$.

2.1. Compute the covariance matrix $\boldsymbol{\Sigma}$ on N measurement points

$\{(x_1, y_1), (x_2, y_2), \dots, (x_N, y_N)\}$ using Equation (65) as:

$$\boldsymbol{\Sigma} = \begin{pmatrix} \text{Cov}((x_1, y_1), (x_1, y_1)) & \dots & \text{Cov}((x_1, y_1), (x_N, y_N)) \\ \vdots & \ddots & \vdots \\ \text{Cov}((x_N, y_N), (x_1, y_1)) & \dots & \text{Cov}((x_N, y_N), (x_N, y_N)) \end{pmatrix}.$$

2.2 Implement the Cholesky decomposition on Σ and obtain $\Sigma = \mathbf{D}\mathbf{D}^T$,

where \mathbf{D} is a lower triangular matrix.

2.3 Calculate the response value on $\{(x_1, y_1), (x_2, y_2), \dots, (x_N, y_N)\}$:

2.3.1 Generate a N -dimensional Gaussian white noise

$$\mathbf{c} \sim \text{MVN}(\mathbf{0}, \mathbf{I}_N).$$

2.3.2 Obtain the response value of \mathbf{B}_{H_x, H_y} via $\mathbf{B}_{H_x, H_y} = \mathbf{D}\mathbf{c}$.

Step 3. Compute the simulated surface with anisotropic LRD effect as

$$\mathbf{z} = \alpha\mathbf{f} + \sigma\mathbf{B}_{H_x, H_y}.$$

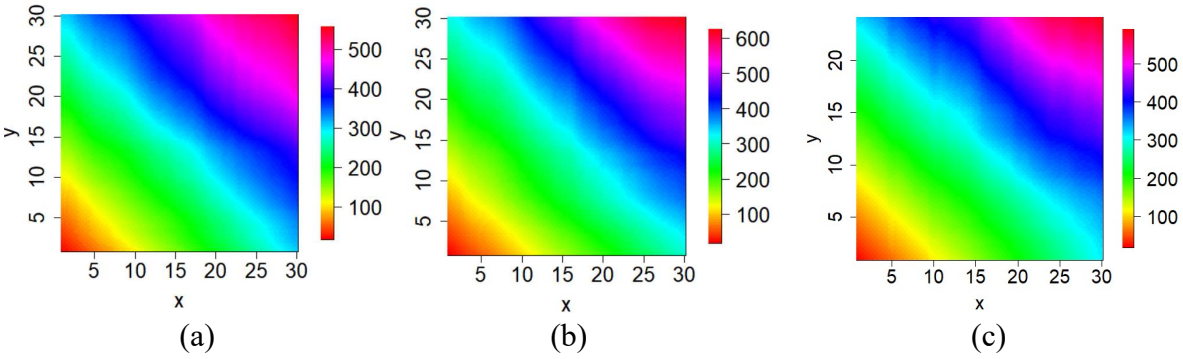


Figure 4.3. (a) In-control surface; (b) Out-of-control surface under Setting 1; (c) Out-of-control surface under Setting 5

4.4.2.2 Parameter Estimation

We apply the proposed anisotropic model to analyzing the simulated surfaces in Section 4.4.2.1. The point estimates and the corresponding standard errors are calculated using the MLE approach developed in Section 4.3.1. For illustration purposes, Table 4-7 lists the estimation results of the first five samples of in-control surfaces. For all samples, the estimated model parameters are close to the pre-specified model parameters, which demonstrates that the MLE approach achieves a good performance under the current image size.

Table 4-7. Point Estimates and Standard Errors of M_5 Parameters

Setting	Parameters	Actual Value	1st Sample	2nd Sample	3rd Sample	4th Sample	5th Sample
in-control	H_x	0.7	0.692	0.705	0.721	0.683	0.676
	$se(H_x)$	—	0.0206	0.0211	0.0196	0.0206	0.0202
	H_y	0.8	0.794	0.826	0.799	0.798	0.801
	$se(H_y)$	—	0.0183	0.0180	0.0187	0.0195	0.0186
	σ^2	0.1	0.0997	0.110	0.106	0.0922	0.0954
	$se(\sigma^2)$	—	0.00616	0.00853	0.00715	0.00610	0.00609
	α	10	10.1	10.1	9.96	9.97	9.913
	$se(\alpha)$	—	0.00151	0.00684	0.00363	0.0171	0.0137

To further assess the MLE performance of model M_5 , we repeat the simulation and estimation processes for 500 times and calculate the RMSEs of M_5 parameters under different image sizes, i.e., $P = 20 \times 20$, 30×30 and 40×40 . The results of RMSEs are summarized in Table 4-8, and it can be seen that as the sample size increases, the RMSEs of the parameter estimation decrease for all parameters. This result is consistent with that in Section 4.4.1.2 and further demonstrates the good performance of the MLE approach.

Table 4-8. RMSEs of Parameter Estimation of M_5 under Different Image Sizes

Sample Size (P)	$RMSE(\widehat{H}_x)$	$RMSE(\widehat{H}_y)$	$RMSE(\widehat{\sigma}^2)$	$RMSE(\widehat{\alpha})$
20×20	0.0316	0.0274	0.0121	0.0870
30×30	0.0205	0.0189	0.00833	0.0847
40×40	0.0152	0.0138	0.00635	0.0727

4.4.2.3 Surface Anomaly Detection

Using the estimated model parameters of M_5 , we conduct surface quality control via the control chart developed in Section 4.3. Specifically, 100 in-control surfaces are selected to estimate the in-control model parameters as $\widehat{\theta}_0 = (\widehat{H}_{x0}, \widehat{H}_{y0}, \widehat{\sigma}_0^2, \widehat{\alpha}_0) = (0.702, 0.798, 0.100, 9.99)$. The other 500 in-control surfaces are applied to calculate the UCL and LCL of the monitoring statistic under the significance level $q = 0.0027 / \text{nominal ARL}_0 = 370$. We also apply the approximation method of the monitoring statistic, and the constants (t, r, k) are estimated as

$(-2.55 \times 10^{-4}, 9.40 \times 10^{-4}, 5.07)$. For each out-of-control setting, 500 out-of-control surfaces of that setting are selected to calculate the ARL_1 . The results using M_5 under the six out-of-control settings are listed in Table 4-9. Results show that the proposed model achieves small ARL_1 , which indicates that the proposed anisotropic spatial model M_5 and surface monitoring method can rapidly detect surface anomaly in all settings.

Table 4-9. ARL_1 of M_5 under Six Out-of-control Settings at $q = 0.0027$

Model	Metric	Setting 1	Setting 2	Setting 3	Setting 4	Setting 5	Setting 6
M_5	ARL_1	3.012	1.094	12.50	1.493	1.000	1.000

4.4.2.4 Model Comparison

To demonstrate the advantage of the proposed model, we compare the proposed anisotropic spatial model with three conventional models that ignore LRD, i.e., an anisotropic Kriging model [99], a Brownian sheet-based spatial model [132], and an autoregressive model, which are respectively termed as $M_6 \sim M_8$ as follows:

$$\begin{cases} M_6 : z(x, y) = \alpha(x + y) + \sigma G_A(x, y) \\ M_7 : z(x, y) = \alpha(x + y) + \sigma B_s(x, y) \\ M_8 : z(x, y) = f(\mathbf{z}^{(x, y)}) + \varepsilon; \varepsilon \sim N(0, d^2) \end{cases} \quad (82)$$

Specifically, in model M_6 , $G_A(x, y)$ denotes an anisotropic Gaussian random field with a mean of

zero and a covariance function as

$$Cov(G_A(x_i, y_i), G_A(x_j, y_j)) = \exp\left(-s_x(x_i - x_j)^2 - s_y(y_i - y_j)^2\right),$$

where s_x and s_y are the scale parameters for x and y directions, respectively. In model M_7 , $B_s(x, y)$ represents a Brownian sheet,

i.e., a standard fractional Brownian sheet with $H_x = 0.5$ and $H_y = 0.5$. In model M_8 , the

dependency structure is only considered up to a few neighborhood pixels. Models $M_6 \sim M_8$ are then

applied to analyzing the simulated surfaces in Section 4.4.2.1 and conduct surface anomaly

detections at the significance level $q = 0.0027$. The values of ARL_1 using $M_6 \sim M_8$ are summarized in Table 4-10, along with the result of M_5 . It is observed that the proposed model M_5 results in significantly smaller ARL_1 than the conventional models $M_6 \sim M_8$. Model M_7 as a special case of M_5 generally performs the second best. Model M_8 that only considers the neighborhood dependency performs the worst. These results reveal that the proposed model, by integrating the anisotropic LRD effect, can detect surface anomaly much faster when the process goes out-of-control.

Table 4-10. ARL_1 of $M_5 \sim M_8$ under Six Settings of Out-of-control Surfaces at $q = 0.0027$

Model	Setting 1	Setting 2	Setting 3	Setting 4	Setting 5	Setting 6
M_5	3.012	1.094	12.50	1.493	1.000	1.000
M_6	29.42	31.25	50.00	22.73	23.81	23.81
M_7	31.25	33.33	33.33	3.521	1.004	1.004
M_8	33.3	45.45	45.45	55.55	250	250

4.5 Case Study

To further validate the proposed LRD-integrated spatial model and surface monitoring approach, we conduct a case study based on real images of wood surfaces. A brief description of the dataset is presented in Section 4.5.1. In Section 4.5.2, we apply the proposed model to analyze the wood surface images and estimate model parameters. A surface anomaly detection is performed in Section 4.5.3. To show the advantages of the proposed models, Section 4.5.4 conducts multiple model comparisons.

4.5.1 Data Description

A publicly available dataset of wood surface images is selected in the case study [133]. The wood surfaces clearly demonstrate textures along the vertical direction as shown in Figure 4.4. Specifically, 600 wood surface images with a discretized size of 30×30 pixels are applied as the in-control surfaces. We obtain the out-of-control surfaces by contracting the original wood surface

images both vertically and horizontally. This contraction method to obtain the out-of-control surfaces has been well adopted in the surface monitoring literature [26]. Specifically, four out-of-control settings are created in the case study, which are summarized in Table 4-11. Figure 4.4 illustrates one example of in-control wood surfaces and two examples of out-of-control surfaces under Settings 2 and 3. It can be seen that these images are visually challenging to distinguish.

Table 4-11. Four Settings of Out-of-control Surfaces

Setting 1	Setting 2	Setting 3	Setting 4
Contracted vertically by 10%	Contracted vertically by 20%	Contracted horizontally by 10%	Contracted horizontally by 20%

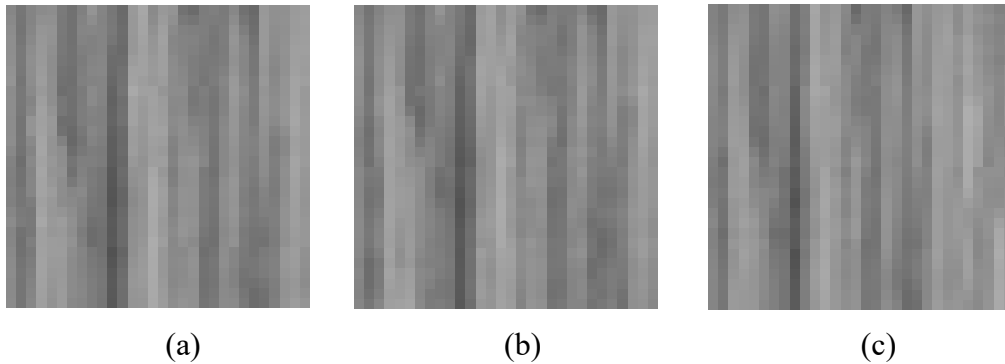


Figure 4.4. (a) In-control wood surface; (b) Out-of-control wood surface under Setting 2; (c) Out-of-control wood surface under Setting 3

4.5.2 Parameter Estimation

We apply both the proposed isotropic and anisotropic LRD-integrated spatial models to characterize the wood surface images. For simplicity purposes, a constant trend term is selected since there is no significant baseline trend on the wood surface as shown in Figure 4.4. The proposed models with a constant trend term under these two scenarios, respectively, are as follows:

$$\begin{cases} M_9 : z(x, y) = \alpha + \sigma B_H(x, y) \\ M_{10} : z(x, y) = \alpha + \sigma B_{H_x, H_y}(x, y) \end{cases} \quad (83)$$

The parameters of the isotropic model M_9 and the anisotropic model M_{10} are $\theta = (H, \sigma^2, \alpha)$ and $\theta = (H_x, H_y, \sigma^2, \alpha)$, respectively. The point estimates and standard errors of the model parameters

are obtained using the developed MLE approach and listed in Table 4-12. We present the estimation results of the first five samples of in-control surfaces for illustration purposes. It can be seen that for M_9 the estimated Hurst parameter \widehat{H} is generally greater than 0.5, which demonstrates the existence of overall LRD in the in-control images. For M_{10} , \widehat{H}_y is higher than 0.5, while \widehat{H}_x is lower than 0.5, which implies that the LRD exists along the vertical direction. From Figure 4.3, it is observed that the wood surface images are clearly anisotropic with textures along the vertical direction. Therefore, the dependence structure revealed by the anisotropic model is more reliable.

Table 4-12. Point Estimates and Standard Errors of M_9 and M_{10} Parameters

Model	Parameters	1st sample	2nd sample	3rd sample	4th sample	5th sample
M_9	H	0.714	0.722	0.765	0.841	0.816
	$se(H)$	0.0528	0.0497	0.0513	0.0539	0.0604
	σ^2	0.195	0.161	0.172	0.257	0.316
	$se(\sigma^2)$	0.0271	0.0219	0.0304	0.0775	0.0895
	α	0.625	0.149	-0.630	0.252	0.266
	$se(\alpha)$	0.0190	0.0640	0.0221	0.0198	0.0261
M_{10}	H_x	0.0662	0.0352	0.0485	0.0508	0.0369
	$se(H_x)$	0.0153	0.0113	0.0129	0.0119	0.0124
	H_y	0.607	0.585	0.556	0.582	0.594
	$se(H_y)$	0.0273	0.0277	0.0276	0.0285	0.279
	σ^2	0.0478	0.0484	0.0428	0.0457	0.0379
	$se(\sigma^2)$	0.00176	0.00158	0.00135	0.00135	0.00127
	α	0.225	0.291	-0.0577	0.362	0.0217
	$se(\alpha)$	0.0174	0.0205	0.00414	0.0276	0.00521

4.5.3 Surface Anomaly Detection

Based on the estimated parameters of models M_9 and M_{10} , we conduct surface anomaly detection using the LRD-integrated surface monitoring approach. Specifically, 100 in-control wood surfaces are selected to calculate the in-control model parameters as

$$\widehat{\theta} = \left(\widehat{H}_0, \widehat{\sigma}_0^2, \widehat{\alpha}_0 \right) = (0.849, 0.441, -0.0397) \quad \text{and}$$

$$\widehat{\theta} = \left(\widehat{H}_{x_0}, \widehat{H}_{y_0}, \widehat{\sigma}_0^2, \widehat{\alpha}_0 \right) = (0.0294, 0.559, 0.0550, 0.00153) \quad \text{for models } M_9 \text{ and } M_{10}, \text{ respectively.}$$

The other 500 in-control surfaces are chosen to calculate the UCL and the LCL of the monitoring statistic under significance level $q = 0.0027$. Due to the limited sample size, we apply the approximation method of monitoring statistic, and the constants (r, t, k) are estimated as $(-2.79 \times 10^{-3}, 0.0559, 1.97)$ and $(-0.0179, 0.0169, 3.81)$ for models M_9 and M_{10} , respectively. The remaining 500 out-of-control surfaces are then applied to evaluating the detection performance. Table 4-13 lists the values of ARL_1 of both models M_9 and M_{10} . It can be seen that the anisotropic model M_{10} achieves a smaller ARL_1 . Therefore, the proposed anisotropic model M_{10} significantly outperforms the isotropic model M_9 . This is because the images of wood surfaces clearly demonstrate anisotropy as illustrated in Figure 4.4.

Table 4-13. ARL_1 of Models M_9 and M_{10} on Surface Anomaly Detection at $q = 0.0027$.

Model	Metric	Setting 1	Setting 2	Setting 3	Setting 4
M_9	Power	0.006	0.010	0.008	0.012
	ARL_1	166.7	100.0	125.0	83.33
M_{10}	Power	0.062	0.070	0.090	0.142
	ARL_1	16.12	14.29	11.11	7.042

4.5.4 Model Comparison

To demonstrate the advantages of the proposed models, we compare them with five models from the literature that ignore the LRD effect, i.e., an isotropic Kriging model (M_{11}), an anisotropic Kriging model (M_{12}), a Lévy Brownian random field-based model (M_{13}), a Brownian sheet-based model (M_{14}), and a nonlinear autoregressive model (M_{15}) respectively. $M_{11} \sim M_{15}$ are listed as follows:

$$\left\{ \begin{array}{l} M_{11} : z(x, y) = \alpha + \sigma G_I(x, y) \\ M_{12} : z(x, y) = \alpha + \sigma G_A(x, y) \\ M_{13} : z(x, y) = \alpha + \sigma B_L(x, y) \\ M_{14} : z(x, y) = \alpha + \sigma B_S(x, y) \\ M_{15} : z(x, y) = f(\mathbf{z}^{(x,y)}) + \varepsilon; \varepsilon \sim N(0, d^2) \end{array} \right. \quad (84)$$

Based on the images of wood surfaces, surface anomaly detections are conducted under a significance level of $q = 0.0027$. The ARL_1 of $M_{11} \sim M_{15}$ are listed in Table 4-14, along with the results of M_9 and M_{10} for comparisons. It can be observed that the proposed isotropic model M_9 , by considering the LRD effect, significantly outperforms the conventional isotropic models M_{11} and M_{13} in terms of ARL_1 . Meanwhile, the proposed anisotropic LRD-integrated model M_{10} performs considerably better than the anisotropic models M_{12} and M_{14} . Among all the models, the proposed anisotropic model M_{10} , by simultaneously considering the LRD effect and wood surface anisotropy, achieves the lowest ARL_1 and fastest anomaly detection.

Table 4-14. ARL_1 of Models $M_9 \sim M_{15}$ at $q = 0.0027$

Model	Setting 1	Setting 2	Setting 3	Setting 4
M_9	166.7	100.0	125.0	83.33
M_{10}	16.12	14.29	11.11	7.042
M_{11}	166.7	166.7	166.7	125.0
M_{12}	100.0	100.0	55.56	45.45
M_{13}	166.7	125.0	166.7	125.0
M_{14}	25.00	23.81	16.67	10.20
M_{15}	62.50	50.00	71.42	55.56

4.6 Conclusion

The LRD effect has been recently detected in spatial data of various material surfaces. Most existing spatial models and surface monitoring methods ignore the spatial LRD effect, which could lead to inefficient surface data characterization and in turn incur erroneous surface anomaly

detection and low product quality. To overcome this challenge, in this chapter we first propose a novel spatial model that considers the spatial LRD to characterize material surfaces. Both isotropic and anisotropic scenarios of the proposed model are established based on the Lévy fractional Brownian random field and fractional Brownian sheet, respectively. Next, based on the proposed spatial model an LRD-integrated surface monitoring framework is developed to monitor surface quality. Simulation studies are implemented to verify the performance of the proposed model, and a case study using real-world wood surface images is conducted to validate the proposed approach. Results show that the proposed spatial modeling and monitoring framework, by considering the spatial LRD effect, significantly outperforms existing approaches in terms of detection power and ARL_1 .

CHAPTER 5

LRD-INTEGRATED STATISTICAL MONITORING USING 3D STRUCTURE INFORMATION

5.1 Introduction

5.1.1 Background and Motivation

Statistical process control on material/product anomaly detection are crucial in many manufacturing fields [134, 135]. Anomalies/defects on material can considerably increase the probability of causing risks, hazards, and failure, and finally result in serious consequences [136]. Most existing studies on anomaly detection used one-dimensional and two-dimensional information, i.e., multiple characters [137] and images [26]. Recently, by virtue of sensor technology, such as computerized tomography (CT) scan, some three-dimensional information is available [138]. Due to the significance of 3D monitoring, it is indispensable to establish an efficient approach to extract features from 3D information and build a corresponding control chart to detect these anomalies based on the features.

Recently, with the recent advancement of metrology technology, a long-range dependence has been detected in various data from one-dimensional to three-dimensional. In mathematics, the LRD effect refers to non-summable auto-correlation functions so that the correlation of two arbitrary measurements is high even across a long Euclidean distance. For one-dimensional data, usually the temporal data, Si, et al. [5] illustrated that the performance degradation of photocatalyst holds the LRD effect on the temporal domain. Another example on the one-dimensional LRD is in finance field, Aslam, et al. [139] investigated the LRD effect within emerging stock markets using a multifractal detrended fluctuation analysis. In addition to one-

dimensional cases, the existence of LRD effect has also been demonstrated in several two-dimensional spatial cases. For example, Kohli [140] discovered that the distribution of ozone levels in Europe and Mediterranean demonstrates the spatial LRD. Richard [94] illustrated that the image texture of photographic prints exhibits the LRD effect. Beyond one and two-dimensional scenarios, the LRD effect has already been mathematically defined in three-dimensional space. Taqqu [85] provided the mathematical definition for three-dimensional LRD effect as well as some critical properties. Moreover, in this chapter, we present a real example of the 3D LRD effect, the spatial LRD in 3D printed carbon composites, in the case study. Since the 3D spatial LRD exists in some materials, it is critical to build an LRD-integrated 3D spatial model to efficiently characterize these materials.

5.1.2 Literature Review

In the literature, various monitoring methods have been proposed to monitor anomalies in materials. Based on the information used for anomaly detection, most existing methods can be divided into two major classifications, including anomaly detection using one-dimensional information, i.e., multi-sensors/multi-parameters anomaly detection, and anomaly detection using two-dimensional information, i.e., image-based anomaly detection. For multi-sensors anomaly detection, Jiang, et al. [141] conducted anomaly detection on magnetic flux using industrial multi-sensor signals. Chen, et al. [142] developed an isolation forest to detect anomalies on a wind turbine using multiple critical attributes. Boud and Gindy [143] monitored broached surfaces anomalies based on multi-sensor signal. For more multi-character anomaly detection, one can refer to [144-146]. However, these multi-parameters approach only obtain limited information from

materials, which could result in inaccurate anomaly detection. To overcome this challenge, some image-based anomaly detection approaches are developed. These models can be majorly separated into two types, including statistical methods and artificial intelligence methods. For the first type, He, et al. [125] developed a multivariate generalized linear regression method to detect multiple faults in manufactured products. Lu and Tsai [147] proposed a singular value decomposition approach to automatic detect inspection. Bui and Apley [26] proposed a non-linear auto-regressive model to extract features form textile surface. Lu and Tsai [147] developed a singular value decomposition approach to automatic detect inspection. For the second type, Imani, et al. [148] developed a deep learning neural network for additive manufacturing quality control using layer-wise images. Zuo, et al. [149] proposed a region growing-based control chart to monitor quality of products. Bisheh, et al. [150] extracted material layer features using a gradient boosting classifier and constructed an exponentially weighted moving average chart to detect anomalies within each layer of baskets. For more method on anomaly detection using two-dimensional information, one can refer to [107, 109, 151]. Since these models only utilize two-dimensional information, they are limited to capture whole characteristics within monitoring parts.

Recently, some researchers established anomaly detection models using three-dimensional structure information. For example, Tao, et al. [152] developed a Bayesian network that can model unstructured 3D point cloud data for anomaly detection of 3D morphology of steel surface. Bergmann and Sattlegger [153] proposed a deep geometric descriptor to detect anomalies in ten categories of manufactured products using 4000 high-resolution 3D scans. Masuda, et al.

[154] conducted 3D point cloud anomaly detection based on a deep variational autoencoder. However, all existing 3D anomaly detection models cannot consider the LRD effect, which could result in inaccurate anomaly detection.

5.1.3 Outline of the Proposed Model

To overcome these challenges, in this chapter, we proposed a novel FBS-based 3D spatial model that can capture the LRD effect within 3D structure information. A maximum likelihood estimation approach is developed to estimate model parameters. Based on the proposed model, we construct two LRD-integrated quality control charts to conduct 3D anomaly detection based on Hotelling T^2 and generalized likelihood ratio test frameworks. A simulation study is implemented to verify the proposed method. To further validate the proposed model, we conduct a 3D printing experiment on Carbon composites. Based on experiment results, i.e., the image sequences of 3D printed parts, we perform a case study to demonstrate the superiority of our proposed model over conventional models. Results show that the proposed model performs significantly good in terms of anomaly detection power.

The remainder of this chapter is summarized as follows. In Section 5.2, we propose an FBS-based 3D model that can quantitatively capture the 3D LRD effect. Based on the proposed model, we develop two LRD-integrated quality charts to detect anomalies in 3D parts in Section 5.3. In Section 5.4, a simulation study to verify the proposed model is implemented. In Section 5.5, we conduct an experiment on 3D printed parts, and a case study is performed to further validate the proposed model using the experiment results. Conclusions and potential future studies are summarized in Section 5.6.

5.2 The Proposed model

5.2.1 The Long-Range Dependence in 3D Space

The LRD effect, also referred to as the long-term memory or long memory effect, has been detected in one-dimensional, two-dimensional and three-dimensional data. It refers to non-summable auto-correlation functions so that correlation of two arbitrary measurements is high even across a long Euclidean distance.

For one-dimensional data, usually temporal data, the LRD implies a slow decay of autocovariance/autocorrelation with heavy tails over so that temporal measurements are highly correlated across a long period of time. Mathematically, the LRD effect is defined as follows. Consider a stationary stochastic process $\{X(t)|t \geq 0\}$. The expectation of $X(t)$ is constant and satisfies $E(X(t)) = E(X(0))$. The autocovariance function of $X(t)$ satisfies:

$$\gamma_X(\tau) = Cov(X(t+\tau), X(t)) = Cov(X(\tau), X(0)); \tau \geq 0 \quad (85)$$

where $\gamma_X(\tau)$ only depends on the time lag τ between two measurements. $X(t)$ has the LRD effect if its autocovariance function satisfies $\sum_{u=0}^{+\infty} |\gamma_X(u)| = +\infty$, which indicates that the autocovariances are non-summable [84], and the ACF plot commonly demonstrates a heavy tail.

Note that when the autocovariances are summable, i.e., $\sum_{u=0}^{+\infty} |\gamma_X(u)| < +\infty$, $X(t)$ has the short-range dependence (SRD) effect. Equivalently, the temporal LRD effect can also be defined using the spectral density of $X(t)$ as follows:

$$s_X(\omega) = \frac{1}{2\pi} \int_{-\infty}^{+\infty} e^{-i\omega k} \gamma_X(k) dk; \omega \in (-\pi, \pi] \quad (86)$$

where $i = \sqrt{-1}$ is the imaginary unit; and ω is the angular frequency. $X(t)$ exhibits the LRD effect if its spectral density $s_X(\omega)$ satisfies [84]:

$$s_X(\omega) \sim C_s |\omega|^\lambda, \text{ as } \omega \rightarrow 0 \quad (87)$$

where $C_s \in R_+$ and $\lambda \in (-1, 0)$ are two constants. A common example of stochastic processes that exhibits the LRD is the fractional Brownian motion with a Hurst parameter $H \in (0.5, 1)$ [48].

For two-dimensional and three-dimensional spatial data, the spatial LRD effect refers to the slowly decaying autocovariance over spatial distance such that measurements are highly correlated across long spatial distances. Consider a stationary random field defined on a two-dimensional space, $\{Y(x_1, x_2) | (x_1, x_2) \in R^2\}$. Similarly, the spectral density of $Y(x_1, x_2)$ is denoted as $s_Y(\omega_1, \omega_2)$, where ω_1 and ω_2 are angular frequencies along the directions of x_1 and x_2 , respectively. Specifically, the random field $Y(x_1, x_2)$ is called to be long-range dependent if its spectral density satisfies [119]:

$$s_Y(\omega_1, \omega_2) \sim C_1 |\omega_1|^{\lambda_1} C_2 |\omega_2|^{\lambda_2}, \text{ as } \omega_1, \omega_2 \rightarrow 0 \quad (88)$$

where $C_1, C_2 \in R_+$ and $\lambda_1, \lambda_2 \in (-1, 0)$ are constants.

For three-dimensional LRD, we consider a stationary random field defined on a three-dimensional space, $\{Z(x_1, x_2, x_3) | (x_1, x_2, x_3) \in R^3\}$, where (x_1, x_2, x_3) denotes the coordinate on the three-dimensional space R^3 . The expectation of $Z(x_1, x_2, x_3)$ satisfies $E(Z(x_1, x_2, x_3)) = E(Z(0, 0, 0))$. The autocovariance function of $Z(x_1, x_2, x_3)$ satisfies:

$$\begin{aligned}\gamma_Z(u_1, u_2, u_3) &= \text{Cov}(Z(x_1 + u_1, x_2 + u_2, x_3 + u_3), Z(x_1, x_2, x_3)) \\ &= \text{Cov}(Z(u_1, u_2, u_3), Z(0, 0, 0)); u_1, u_2, u_3 \in R\end{aligned}\quad (89)$$

In Equation (89), $\gamma_Z(u_1, u_2, u_3)$ only depends on the spatial lags u_1 , u_2 and u_3 . Based on $\gamma_Z(u_1, u_2, u_3)$, the spectral density of $Z(x_1, x_2, x_3)$ can be calculated as:

$$s_Z(\omega_1, \omega_2, \omega_3) = \left(\frac{1}{2\pi}\right)^3 \int_{-\infty}^{+\infty} \int_{-\infty}^{+\infty} \int_{-\infty}^{+\infty} e^{-i\omega_1 k - i\omega_2 l - i\omega_3 q} \gamma_Z(k, l, q) dk dl dq; \omega_1, \omega_2, \omega_3 \in (-\pi, \pi] \quad (90)$$

where ω_1 , ω_2 and ω_3 are angular frequencies along the directions of x_1 , x_2 and x_3 , respectively. Specifically, the random field $Z(x_1, x_2, x_3)$ is called to be long-range dependent if its spectral density satisfies [119]:

$$s_Y(\omega_1, \omega_2, \omega_3) \sim C_1 |\omega_1|^{\lambda_1} C_2 |\omega_2|^{\lambda_2} C_3 |\omega_3|^{\lambda_3}, \text{ as } \omega_1, \omega_2, \omega_3 \rightarrow 0 \quad (91)$$

where $C_1, C_2, C_3 \in R_+$ and $\lambda_1, \lambda_2, \lambda_3 \in (-1, 0)$ are constants.

5.2.2 The LRD-Integrated 3D Model

By virtue of recent advancements in metrology technology, the LRD effect has already been detected in some 3D parts, such as 3D printed carbon composites. To model such 3D parts, we proposed an LRD-integrated 3D model using 3D Fractional Brownian Sheet as follows:

$$m(x_i, y_i, z_i) = \alpha f(x_i, y_i, z_i | \boldsymbol{\theta}_f) + \sigma B_H(x_i, y_i, z_i); i \in 1, 2, 3, \dots, N \quad (92)$$

where $m(x_i, y_i, z_i)$ denotes the measure of interest at the coordinate (x_i, y_i, z_i) ; $\alpha f(x_i, y_i, z_i | \boldsymbol{\theta}_f)$ is the trend term to model the trend of 3D parts with parameters α and $\boldsymbol{\theta}_f$; σ is diffusion parameter that controls the magnitude of variations of the proposed model; $B_H(x_i, y_i, z_i)$ represents a standard 3D FBS that is to capture the 3D LRD with hurst parameters H_x , H_y and H_z

for x , y and z directions, respectively.

Specifically, the $B_H(x_i, y_i, z_i)$ is mathematically defined using an integral form as follows:

$$B_H(x, y, z) = \int_{\mathbb{R}^3} \left(|x-k|^{H_x-1/2} - |k|^{H_x-1/2} \right) \left(|y-l|^{H_y-1/2} - |l|^{H_y-1/2} \right) \left(|z-r|^{H_z-1/2} - |r|^{H_z-1/2} \right) dW(k, l, r) \quad (93)$$

where the $W(k, l, r)$ represents a white noise in a 3D space. Specifically, the 3D FBS is a Gaussian random field with a mean of zero and a covariance function as:

$$\begin{aligned} & Cov\left(B_{H_x, H_y, H_z}(x_i, y_i, z_i), B_{H_x, H_y, H_z}(x_j, y_j, z_j)\right) \\ &= \frac{1}{8} \left(x_i^{2H_x} + x_j^{2H_x} - |x_i - x_j|^{2H_x} \right) \left(y_i^{2H_y} + y_j^{2H_y} - |y_i - y_j|^{2H_y} \right) \left(z_i^{2H_z} + z_j^{2H_z} - |z_i - z_j|^{2H_z} \right) \end{aligned} \quad (94)$$

It can be aware from the covariance function (94) that the dependence structure of $B_H(x, y, z)$ is determined by its hurst parameters H_x , H_y and H_z . Specifically, Proposition 5.1 illustrates that the FBS can capture the 3D LRD effect. The proof of Proposition 5.1 is summarized in Appendix A7.

Proposition 5.1: The FBS holds the LRD effect if H_x, H_y and $H_z \in (0.5, 1)$

In addition to the LRD effect, $B_H(x, y, z)$ also exhibits the following properties [121]: i)

$B_H(x, y, 0) = B_H(0, y, z) = B_H(x, 0, z) = 0$; ii) $B_H(x, y, z)$ has stationary increments, i.e.,

$B_H(x + \Delta x, y + \Delta y, z + \Delta z) - B_H(x, y, z) \stackrel{d}{=} B_H(\Delta x, \Delta y, \Delta z)$, where $\stackrel{d}{=}$ denotes equivalence

in distribution; iii) $B_H(x, y, z)$ is operator self-similar, which indicates

$B_H(ax, ay, az) \stackrel{d}{=} a^{H_x + H_y + H_z} B_H(x, y, z)$ for all $a > 0$; and iv) the variance of $B_H(x, y, z)$ satisfies

$$\text{Var}(B_H(x, y, z)) = x^{2H_x} y^{2H_y} z^{2H_z} .$$

5.3 LRD-Integrated Material Monitoring using 3D Structure Information

In this Section, based on the proposed LRD-integrated 3D model, we developed two LRD-integrated quality control charts based on a Hotelling T^2 (HT) frameworks and a generalized likelihood ratio test (GLRT), which have been widely applied to develop quality control for product/material quality monitoring. Specifically, in Section 5.3.1, we develop a maximum likelihood estimation (MLE) approach to identify model parameters of products. Therefore, the features of 3D products can be represented by estimated model parameters. In Sections 5.3.2 and 5.3.3, the Hotelling T^2 -type and GLRT-based LRD-integrated control charts are constructed, respectively.

5.3.1 An MLE Approach for model parameter estimation

It can be seen that the proposed model (92) is determined by model parameters $\boldsymbol{\theta} = (H_x, H_y, H_z, \sigma^2, \alpha, \boldsymbol{\eta}_f)$. To estimate $\boldsymbol{\theta}$, we develop an MLE approach given a set of N measurements of a 3D part $\mathbf{m} = (m(x_1, y_1, z_1), m(x_2, y_2, z_2), \dots, m(x_N, y_N, z_N))$. Via denoting $\mathbf{f} = (f(x_1, y_1, z_1), f(x_2, y_2, z_2), \dots, f(x_N, y_N, z_N))$ and $\mathbf{B}_H = (B_H(x_1, y_1, z_1), B_H(x_2, y_2, z_2), \dots, B_H(x_N, y_N, z_N))$ as two N -dimensional vectors, we obtain a vector form of the proposed model (92) as follows:

$$\mathbf{m} = \alpha \mathbf{f} + \sigma \mathbf{B}_H \quad (95)$$

In Equation (95), \mathbf{B}_H follow a multivariate normal distribution since the FBS is a Gaussian random field. Specifically, the mean of \mathbf{B}_H is zero, and the covariance matrix is \mathbf{Q} , i.e., $\mathbf{B}_H \sim MVN(\mathbf{0}, \mathbf{Q})$, where (i, j) th entry of matrix \mathbf{Q} is calculated using Equation (94). Therefore,

the distribution of \mathbf{m} is then derived as a multivariate normal distribution with a mean vector of $\alpha\mathbf{f}$ and a covariance matrix of $\sigma^2\mathbf{Q}$, i.e., $\mathbf{m} \sim N(\alpha\mathbf{f}, \sigma^2\mathbf{Q})$. Based on the measurement data \mathbf{m} , the log-likelihood function of a single 3D part is obtained as follows:

$$l(\boldsymbol{\theta}|\mathbf{m}) = -\frac{N}{2}\ln(2\pi) - \frac{N}{2}\ln(\sigma^2) - \frac{1}{2}\ln|\mathbf{Q}| - \frac{(\mathbf{m} - \alpha\mathbf{f})^T \mathbf{Q}^{-1} (\mathbf{m} - \alpha\mathbf{f})}{2\sigma^2} \quad (96)$$

By summing the Equation (96) of different 3D parts, we can then obtain the overall log-likelihood function of multiple 3D parts. Given a collection of measurements of K 3D parts $\{\mathbf{m}_1, \mathbf{m}_2, \dots, \mathbf{m}_K\}$, the overall log-likelihood function is derived as:

$$\begin{aligned} & l(\boldsymbol{\theta}|\{\mathbf{m}_1, \mathbf{m}_2, \dots, \mathbf{m}_K\}) \\ &= -\frac{KN}{2}\ln(2\pi) - \frac{KN}{2}\ln(\sigma^2) - \frac{K}{2}\ln|\mathbf{Q}| - \frac{\sum_{i=1}^{i=K} (\mathbf{m}_i - \alpha\mathbf{f})^T \mathbf{Q}^{-1} (\mathbf{m}_i - \alpha\mathbf{f})}{2\sigma^2} \end{aligned} \quad (97)$$

The model parameters $\boldsymbol{\theta}$ can be obtained by maximizing the log-likelihood function (97) with respect to $\boldsymbol{\theta}$, i.e.,

$$\hat{\boldsymbol{\theta}} = \arg \max_{\boldsymbol{\theta}} \{l(\boldsymbol{\theta}|\{\mathbf{m}_1, \mathbf{m}_2, \dots, \mathbf{m}_K\})\} \quad (98)$$

To maximizing the log-likelihood function (98), the closed-form estimators of parameters α and σ^2 are constructed conditional on other parameters, $\boldsymbol{\theta}' = (H_x, H_y, H_z, \boldsymbol{\eta}_f)$. We first taking partial derivatives of (98) with respect to α and σ^2 , respectively, and then set the partial derivatives to zero. The closed-form MLE estimators are summarized in Proposition 5.2.

Proposition 5.2. The closed-form MLE estimators of α and σ^2 :

$$\hat{\alpha} = \frac{\sum_{i=1}^{i=K} \mathbf{m}_i^T \mathbf{Q}^{-1} \mathbf{f}}{K\mathbf{f}^T \mathbf{Q}^{-1} \mathbf{f}}; \quad \hat{\sigma}^2 = \frac{\sum_{i=1}^{i=K} \mathbf{m}_i^T \mathbf{Q}^{-1} \mathbf{m}_i}{KN} - \frac{\left(\sum_{i=1}^{i=K} \mathbf{m}_i^T \mathbf{Q}^{-1} \mathbf{f}\right)^2}{K^2 \mathbf{f}^T \mathbf{Q}^{-1} \mathbf{f}} \quad (99)$$

Based on Proposition 5.2, we derive the profile log-likelihood function via substituting The closed-form MLE estimators of α and σ^2 into the log-likelihood function (97) as follows:

$$\begin{aligned}
& l(\boldsymbol{\theta}'|\{\mathbf{m}_1, \mathbf{m}_2, \dots, \mathbf{m}_K\}) \\
&= \frac{KN}{2}(-\ln(2\pi)-1) - \frac{K}{2}\ln|\mathbf{Q}| - \frac{KN}{2}\ln\left(\frac{\sum_{i=1}^{i=K}\mathbf{m}_i^T\mathbf{Q}^{-1}\mathbf{m}_i}{KN} - \frac{\left(\sum_{i=1}^{i=K}\mathbf{m}_i^T\mathbf{Q}^{-1}\mathbf{f}\right)^2}{K^2\mathbf{Nf}^T\mathbf{Q}^{-1}\mathbf{f}}\right) \quad (100)
\end{aligned}$$

The parameters $\boldsymbol{\theta}'$ can then be estimated by maximizing the profile log-likelihood function with respect to $\boldsymbol{\theta}'$, i.e., $\widehat{\boldsymbol{\theta}}' = \arg \max_{\boldsymbol{\theta}'} \{l(\boldsymbol{\theta}'|\{\mathbf{z}_1, \mathbf{z}_2, \dots, \mathbf{z}_M\})\}$. In addition to parameters $\boldsymbol{\theta}'$, the point estimates of parameters α_0 and σ_0^2 can be estimated via substituting the point estimates $\widehat{\boldsymbol{\theta}}'$ into Equation (99).

5.3.2 A Multivariate HT-type Control Chart

To develop a multivariate HT-type control chart, in Phase I, given n historical in-control product data $\{\mathbf{m}_1, \mathbf{m}_2, \dots, \mathbf{m}_n\}$, the in-control parameters are estimated individually using the developed MLE method in Section 5.3.3, denoted as $\{\widehat{\boldsymbol{\theta}}_1, \widehat{\boldsymbol{\theta}}_2, \dots, \widehat{\boldsymbol{\theta}}_n\}$. In Phase II, we determine whether a new product P is in-control or out-of-control using the multivariate HT-type chart. Let $\boldsymbol{\theta}_P$ and $\boldsymbol{\theta}_0$ denote the model parameters of product P and in-control model parameters. Specifically, the hurst parameters H_x, H_y and H_z in $\boldsymbol{\theta}_P$ and $\boldsymbol{\theta}_0$ holds the LRD effect. To conduct the quality control on anomaly detection, we assume that $\boldsymbol{\theta}_0$ follow a v -dimensional multivariate normal distribution with a mean of $\boldsymbol{\mu}_0$ and a covariance matrix of $\boldsymbol{\Sigma}$. This normality assumption has been widely applied in multivariate quality control literature [155]. Therefore, to monitor products using three-dimensional information, the following hypothesis test are developed:

$$H_0 : \text{Surface } P \text{ is in-control, i.e., } \widehat{\boldsymbol{\theta}}_P \sim N_v(\boldsymbol{\mu}_0, \boldsymbol{\Sigma}) \quad H_1 : \text{Surface } P \text{ is out-of-control} \quad (101)$$

Based on the framework of Hotelling's T^2 -type chart [155], a monitoring statistic J to determine whether a new product is in-control or out-of-control is constructed as follows:

$$J = \left(\widehat{\boldsymbol{\theta}}_P - \widehat{\boldsymbol{\mu}}_0\right)^T \mathbf{S}^{-1} \left(\widehat{\boldsymbol{\theta}}_P - \widehat{\boldsymbol{\mu}}_0\right) \sim \frac{v(n-1)(n+1)}{n(n-v)} F_{v, n-v} \quad (102)$$

where $\widehat{\boldsymbol{\theta}}_P$ is the estimated model parameters of the new surface P ; $\widehat{\boldsymbol{\mu}}_0 = \left(\widehat{\boldsymbol{\theta}}_1 + \widehat{\boldsymbol{\theta}}_2 + \dots + \widehat{\boldsymbol{\theta}}_n\right) / n$;

$\mathbf{S} = \sum_{i=1}^n \left(\widehat{\boldsymbol{\theta}}_i - \widehat{\boldsymbol{\mu}}_0\right) \left(\widehat{\boldsymbol{\theta}}_i - \widehat{\boldsymbol{\mu}}_0\right)^T / (n-1)$; and $F_{m,n}$ denotes a F -distribution with degrees of freedom of

m and n . In Equation (102), the monitoring statistic J follows a scaled F -distribution [155].

Therefore, both the upper control limit (UCL) and the lower control limit (LCL) under a significance level of q can be calculated as follows:

$$UCL = \frac{v(n-1)(n+1)}{n(n-v)} QF_{v, n-v} (1-q/2); \quad LCL = 0 \quad (103)$$

where $QF_{m,n}(x)$ denotes the x -quantile of a F -distribution with degrees of freedom m and n .

5.3.3 A GLRT-based Control Chart

In Section 5.3.2, we assume that the in-control model parameters follow a multivariate normal distribution and then build a multivariate HT chart. However, this normality assumption may not be applicable for some real cases. To overcome this challenge, in addition to the multivariate HT-type chart, we further develop an LRD-integrated quality control chart using GLRT framework without the normality assumption.

To develop a GLRT-based control chart, in Phase I, given M historical in-control product data $\{\mathbf{m}_1, \mathbf{m}_2, \dots, \mathbf{m}_M\}$, the in-control parameters are estimated integrally using the developed MLE method in Section 5.3.1, denoted as $\widehat{\boldsymbol{\theta}}_0$. In Phase II, we determine whether a new product P is in-control or out-of-control using a GLRT. Let $\boldsymbol{\theta}_P$ and $\boldsymbol{\theta}_0$ denote the model parameters of product P and in-control model parameters. The product P will be considered as out-of-control if $\boldsymbol{\theta}_P$ deviates from the in-control parameters $\boldsymbol{\theta}_0$. Therefore, to monitor products using three-dimensional

information, the following hypothesis test are developed:

$$H_0: \boldsymbol{\theta}_P = \boldsymbol{\theta}_0 \quad H_1: \boldsymbol{\theta}_P \neq \boldsymbol{\theta}_0 \quad (104)$$

Specifically, in the GLRT framework, using the estimated parameters as inputs, a monitoring statistic W is constructed as follows:

$$W = 2 \left(l_P \left(\widehat{\boldsymbol{\theta}}_P \mid \mathbf{m}_P \right) - l_0 \left(\widehat{\boldsymbol{\theta}}_0 \mid \mathbf{m}_P \right) \right) / N_P \quad (105)$$

where \mathbf{m}_P is the set of all measurements of product P , i.e., the three-dimensional information;

N_P is the number of measurements on product P ; $l_P \left(\widehat{\boldsymbol{\theta}}_P \mid \mathbf{m}_P \right)$ is the likelihood value calculated

using $\widehat{\boldsymbol{\theta}}_P$ given \mathbf{m}_P ; and $l_0 \left(\widehat{\boldsymbol{\theta}}_0 \mid \mathbf{m}_P \right)$ denotes the likelihood value evaluated at $\widehat{\boldsymbol{\theta}}_0$ given \mathbf{m}_P .

By substituting $\widehat{\boldsymbol{\theta}}_0$ and $\widehat{\boldsymbol{\theta}}_P$ into Equation (74), we obtain the monitoring statistic W for material surfaces as

$$W = \ln \left(\frac{\widehat{\sigma}_0^2}{\widehat{\sigma}_P^2} \right) + \frac{1}{N_P} \ln \frac{|\mathbf{Q}_0|}{|\mathbf{Q}_P|} + \frac{\left(\mathbf{m}_P - \widehat{\alpha}_0 \mathbf{f} \right)^T \mathbf{Q}_0^{-1} \left(\mathbf{m}_P - \widehat{\alpha}_0 \mathbf{f} \right)}{2N_P \widehat{\sigma}_0^2} - \frac{\left(\mathbf{m}_P - \widehat{\alpha}_P \mathbf{f} \right)^T \mathbf{Q}_P^{-1} \left(\mathbf{m}_P - \widehat{\alpha}_P \mathbf{f} \right)}{2N_P \widehat{\sigma}_P^2} \quad (106)$$

where \mathbf{Q}_0 and \mathbf{Q}_P are the covariance matrices given $\widehat{\boldsymbol{\theta}}_0$ and $\widehat{\boldsymbol{\theta}}_P$, respectively.

To monitor anomalies in products, both an upper control limit (UCL) and a lower control limit (LCL) of the monitoring statistic W need to be determined. Given the cumulative distribution function of the distribution of W , denoted as $T(w)$, the UCL and LCL under a significance level of q are constructed as follows:

$$UCL = QT(1-q); \quad LCL = 0 \quad (107)$$

where $QT(x)$ denotes the x -quantile of $T(w)$. In most real-world applications, the close-form distribution of W is difficult to derive due to the model complexity. Therefore, we approximate the theoretical distribution of W via the empirical distribution using the monitoring statistics of n in-control surfaces $\{W_1, W_2, \dots, W_n\}$, which can provide a good approximation when the sample size is sufficiently large, i.e., $n \gg q^{-1}$.

In some actual situations, the sample sizes of in-control products are not sufficiently large because of expensive and time-consuming experiments. To handle this challenge, the monitoring statistic can be approximated using $W = t + l\chi_k^2$, where χ_k^2 represents a chi-squared random variable with k degrees of freedom; and t and l are two constants. Herein, k , t and l can be estimated using the method of moments illustrated in Bui and Apley [26]. Therefore, the control limits at the significance level of q can be calculated as follows:

$$\text{UCL} = \hat{t} + \hat{l}Q\chi_{\hat{k}}^2(1-q); \quad \text{LCL} = 0 \quad (108)$$

where $Q\chi_{\hat{k}}^2(x)$ denotes the x -quantile of a chi-squared distribution with \hat{k} degrees of freedom.

5.4 Simulation Study

To verify the proposed model, in this section we perform a simulation study. Specifically, the three-dimensional structures are simulated via the proposed LRD-integrated spatial model in Section 5.4.1. In Section 5.4.2, the simulated structures are then analyzed using the proposed model. Based on the estimated model parameters, we then apply the proposed LRD-integrated charts to monitor the simulated structures.

5.4.1 3D Structure Simulation

To evaluate the performance of the proposed spatial model and quality control charts, a collection of the three-dimensional structures with the LRD effect is simulated. Specifically, a

constant trend term α is selected for illustration purpose since many actual structures do not demonstrate a trend, and the structures are then simulated using the following proposed model (termed as P_1):

$$P_1 : m(x, y, z) = \alpha + \sigma B_{H_x, H_y, H_z}(x, y, z) \quad (109)$$

In P_1 , the model parameters are $\theta = (H_x, H_y, H_z, \sigma^2, \alpha)$. To generate the in-control structures, the model parameters are specified as $\theta = (0.6, 0.7, 0.8, 0.1, 1)$. For out-control structures, we specify five different settings through slightly model parameter shifting to further assess the performance and sensitivity of the proposed method. These five out-of-control settings along with the in-control setting are summarized in Table 5-1.

Table 5-1. Five Settings of Out-of-control Structures along with the In-control Setting

Parameters	In-control	Setting 1	Setting 2	Setting 3	Setting 4	Setting 5
H_x	0.6	0.65	0.6	0.6	0.6	0.6
H_y	0.7	0.7	0.75	0.7	0.7	0.7
H_z	0.8	0.8	0.8	0.85	0.8	0.8
σ^2	0.1	0.1	0.1	0.1	0.11	0.1
α	1	1	1	1	1	1.1

Under the specified model parameters, 600 in-control structures and 100 out-of-control structures under each out-of-control setting with a size of $10 \times 10 \times 10$ measurements are simulated using model P_1 via Algorithm 5.1. Figure 5.1 shows the first simulated in-control structure that holds the 3D spatial LRD effect using an image sequence (each image represents a layer). For illustration, Figures 5.1 and 5.2 show the 1st, 3rd, 5th, 7th and 9th layers of the first simulated sample under both the in-control setting and the out-of-control setting 1, respectively.

Algorithm 5.1. An LRD-integrated 3D structure simulation method

Step 1. Simulate the 3D FBS, i.e., \mathbf{B}_H , using the specified model

parameters $\boldsymbol{\theta} = (H_x, H_y, H_z, \sigma^2, \alpha)$.

1.1. Calculate the covariance matrix \mathbf{Q} on N measurement points

$\{(x_1, y_1, z_1), (x_2, y_2, z_2), \dots, (x_N, y_N, z_N)\}$ via Equation (94) as follows:

$$\mathbf{Q} = \begin{pmatrix} \text{Cov}((x_1, y_1, z_1), (x_1, y_1, z_1)) & \dots & \text{Cov}((x_1, y_1, z_1), (x_N, y_N, z_N)) \\ \vdots & \ddots & \vdots \\ \text{Cov}((x_N, y_N, z_N), (x_1, y_1, z_1)) & \dots & \text{Cov}((x_N, y_N, z_N), (x_N, y_N, z_N)) \end{pmatrix}$$

1.2 Perform the Cholesky decomposition to covariance matrix \mathbf{Q} ,

denoted as $\mathbf{Q} = \mathbf{L}\mathbf{L}^T$, where \mathbf{L} is a lower triangular matrix.

1.3 Simulate the response value of 3D FBS \mathbf{B}_H on

$\{(x_1, y_1, z_1), (x_2, y_2, z_2), \dots, (x_N, y_N, z_N)\}$:

1.3.1 Generate an N -dimensional Gaussian white noise \mathbf{e} , via

$$\mathbf{e} \sim \text{MVN}(\mathbf{0}, \mathbf{I}_N)$$

1.3.2 Calculate the response value of \mathbf{B}_H following $\mathbf{B}_H = \mathbf{L}\mathbf{e}$.

Step 2. Obtain the simulated surface with 3D LRD effect as

$$\mathbf{m} = \alpha \mathbf{1}_N + \sigma \mathbf{B}_H, \text{ where } \mathbf{1}_N = (1, 1, \dots, 1)^T.$$

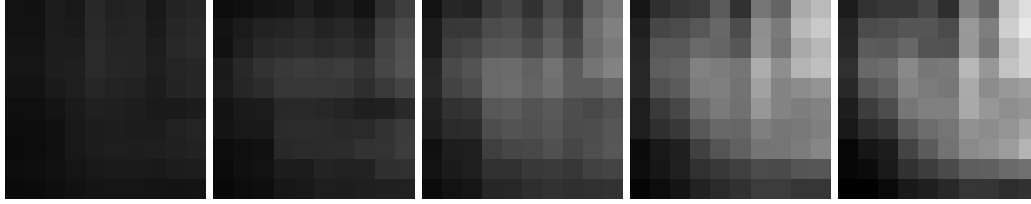


Figure 5.1. 1st, 3rd, 5th, 7th and 9th images of the first sample of in-control setting

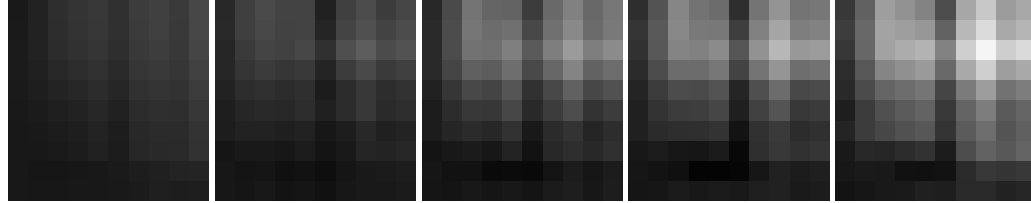


Figure 5.2. 1st, 3rd, 5th, 7th and 9th images of the first sample of out-of-control setting

5.4.2 Model Parameter Estimation and Product Monitoring

The simulated material 3D structures are then analyzed using the proposed LRD-integrated spatial model P_1 . The model parameters and corresponding standard errors are estimated by the MLE approach developed in Section 5.3.1. For illustration purposes, the estimation results for the first five samples of in-control structures are summarized in Table 5-2. From Table 5-2, It can be observed that all the estimated model parameters are close to the pre-specified values, which demonstrates the developed MLE approach achieves a good performance under the current image sequence size.

Table 5-2. The Point Estimates and Standard Errors of P_1 Parameters of In-control Samples

Setting	Parameters	Actual Value	1st Sample	2nd Sample	3rd Sample	4th Sample	5th Sample
in-control	H_x	0.6	0.639	0.601	0.616	0.607	0.644
	$se(H_x)$	—	0.0202	0.0215	0.0209	0.0205	0.0201
	H_y	0.7	0.660	0.695	0.7117	0.733	0.690
	$se(H_y)$	—	0.0199	0.0190	0.0187	0.0180	0.0188
	H_z	0.8	0.817	0.775	0.793	0.800	0.797
	$se(H_z)$	—	0.0151	0.0168	0.0159	0.0160	0.0160
	σ^2	0.1	0.0996	0.0894	0.104	0.113	0.0958
	$se(\sigma^2)$	—	0.00689	0.00503	0.00661	0.00760	0.00582
	α	1	0.683	1.03	0.892	0.765	0.819
	$se(\alpha)$	—	0.0132	0.0100	0.0115	0.00430	0.00903

Based on the estimated model parameters, we then conduct anomaly detection for 3D

structures using both the HT-type and GLRT-based control charts. Specifically, for the HT-type chart, all the 600 in-control structures are selected to estimate the in-control model parameters and calculate both the UCL and LCL under a significance level of $q = 0.0027$, which corresponds to a nominal ARL_0 of 370. For, GLRT-based chart, 100 in-control structures are selected to estimate the in-control model parameters first. The other 500 in-control are then applied to calculating the UCL and LCL under a nominal ARL_0 of 370.

For each of the five out-of-control structure settings, 500 structures are used to evaluate the performance of 3D structure anomaly detection. The ARL_1 of all the out-of-control settings calculated using model P_1 under HT-type and GLRT-based charts are summarized in Table 5-3. From Table 5-3, it can be observed that both the HT-type chart and the GLRT-based chart result in small ARL_{1S} for most of the out-of-control settings. Specifically, the GLRT-based chart provides smaller ARL_{1S} than the HT-type chart for all the out-of-control settings. It indicates that the GLRT-based chart can detect anomalies within 3D structure faster. This is because compared to the HT-type chart, the GLRT-based chart does not require the normality assumption.

Table 5-3. ARL_1 of P_1 under Five Out-of-control Settings at Nominal $ARL_0 = 370$

Setting	Setting 1	Setting 2	Setting 3	Setting 4	Setting 5
ARL_1 -GLRT	5.61	2.84	1.11	9.43	83.33
ARL_1 -HT	10.00	4.81	1.26	9.61	100.00

5.5 Case Study

To validate the proposed 3D anomaly detection method, we further perform a physical experiment regarding 3D carbon composite printing and utilize results to conduct a real-world case study. Section 5.5.1 illustrates the experiment and the data collection process. In Section 5.5.2, a

generative adversarial network is developed to generate more 3D samples. In Section 5.5.3, we apply the proposed model to analyze the 3D carbon composites to obtain the estimated model parameters. Using the estimated model parameters, we conduct anomaly detection on 3D carbon composites using the developed HT-type and GLRT-based control charts.

5.5.1 Experiment and Data Collection Process

We conduct a 3D printing experiment on 3D printing of continuous carbon fiber reinforced thermoplastic (CFRTP) composites. The printing process includes the following steps. It starts with the laser cutting of prepreg sheets following the sliced CAD geometry. Each processed prepreg layer is then stacked on top of the previous layer and bonded by a collimated laser beam and a consolidation roller [138]. Using this printing technique, we obtain an in-control and an out-of-control CFRTP samples. The out-of-control sample contains some voids between prepreg layers, which can significantly reduce the strength and stiffness of the printed CFRTP sample. Specifically, the microstructure of these two 3D printed CFRTPs are then studied through micro computed tomography (micro-CT) scans with an ultrahigh resolution of $1\mu\text{m}$. Using the micro-CT scans of the original two samples, we obtain 20 in-control and 20 out-of-control subsamples by segmenting the original micro-CT scans into 20 subsamples for both the in-control sample and the out-of-control sample. Each sample is a 10-image sequence with an image size of 100×100 pixels, where each image represents a cross-sectional slice of the CT scan. Figures 5.3 and 4 present the first sample of both the in-control sample and the out-of-control sample. For illustration purposes, we only show the 1st, 3rd, 5th, 7th and 9th cross sectional slices of the micro-CT scans of the first samples. As can be seen from Figures 5.3 and 5.4, the in-control sample is

smooth, while the out-of-control sample holds significant voids.

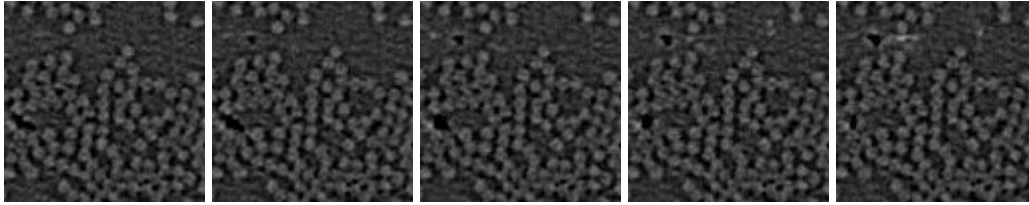


Figure 5.3. 1st, 3rd, 5th, 7th and 9th cross-sectional slices of the first sample of in-control samples

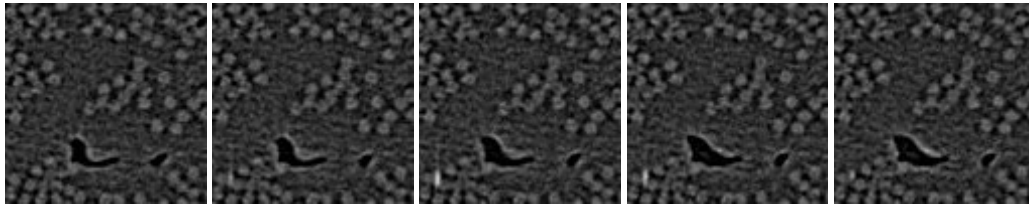


Figure 5.4. 1st, 3rd, 5th, 7th and 9th cross-sectional slices of the first sample of out-of-control samples

5.5.2 A Generative Adversarial Network

To conduct anomaly detection on 3D samples, 20 in-control and 20 out-of-control samples may not be sufficient to calculate UCL and LCL. To overcome this challenge, we developed a Generative Adversarial Network (GAN) using fully connected neural networks [156]. The GAN model has been widely applied to image generation. Specifically, the generator of the trained GAN model contains four layers, the input layer holds 100 nodes, the first hidden layer holds 256 nodes, the second hidden layer holds 512 nodes, the third hidden layer holds 1024 nodes, and the output layer holds 10000 nodes (i.e., 100×100 , the size of cross-sectional slices). Based on the generator, we generate 600 in-control and 500 out-of-control samples using the original 20 in-control and 20 out-of-control samples. For illustration purposes, in Figures 5.5 and 5.6, we show the 1st, 3rd, 5th, 7th and 9th cross sectional slices of two samples generated based on the original samples presented in Figures 3 and 4, respectively. From Figures 5.3~5.6, it can be seen that the

generated samples are similar to the original samples, which indicates that the developed GAN model performs good.

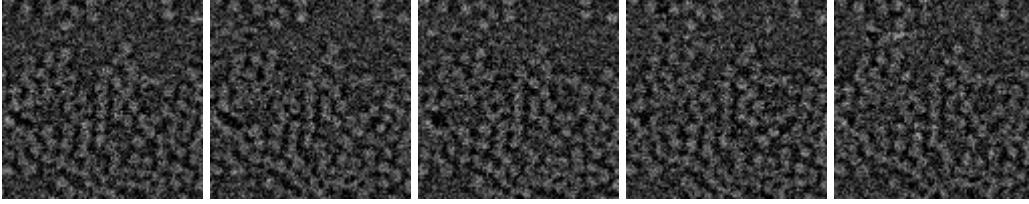


Figure 5.5. 1st, 3rd, 5th, 7th and 9th cross-sectional slices of a generated in-control sample

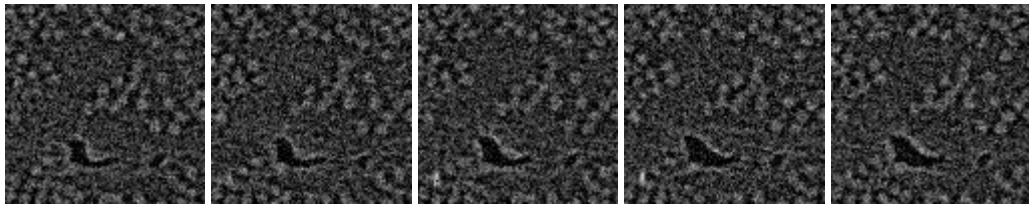


Figure 5.6. 1st, 3rd, 5th, 7th and 9th cross-sectional slices of a generated out-of-control sample

5.5.3 Parameter Estimation and Composite Monitoring

We apply the proposed spatial models to characterize the micro-CT scan of carbon fiber composite.

A constant trend term is selected since there is no significant baseline trend on carbon fiber composite micro-CT scan as shown in Figure 5.3~5.6. Therefore, the proposed models with a constant trend term are as follows:

$$P_2 : m(x, y, z) = \alpha + \sigma B_H(x, y, z) \quad (110)$$

The parameters of the model P_2 are $\boldsymbol{\theta} = (H_x, H_y, H_z, \sigma^2, \alpha)$. The point estimates and corresponding standard errors of the model parameters are estimated using the developed MLE approach and listed in Table 5-4. We show the estimation results of the first five samples of in-control composites for illustration purposes. From Table 5-4, it can be observed that the H_z is higher than 0.5, while H_x and H_y is lower than 0.5, which implies that the LRD exists along the carbon fiber direction.

Table 5-4. The point Estimates and Standard Errors of P_1 Parameters of In-control Samples

Setting	Parameters	1st Sample	2nd Sample	3rd Sample	4th Sample	5th Sample
in-control	H_x	0.00978	0.0117	0.00534	0.0119	0.00530
	$se(H_x)$	0.0118	0.0119	0.0114	0.0120	0.0112
	H_y	0.0776	0.0790	0.0692	0.0855	0.0768
	$se(H_y)$	0.0180	0.0183	0.0175	0.0186	0.0178
	H_z	0.552	0.560	0.570	0.561	0.531
	$se(H_z)$	0.0325	0.0320	0.0312	0.0311	0.0307
	σ^2	0.00495	0.00452	0.00451	0.004575	0.00488
	$se(\sigma^2)$	0.000139	0.000129	0.000128	0.000128	0.000136
	α	0.395	0.367	0.359	0.393194	0.377406
	$se(\alpha)$	0.00236	0.00260	0.00207	0.00242	0.00221

Using the estimated model parameters, anomaly detection on 3D structure is conducted based on the developed HT-type and GLRT-based charts under a nominal $ARL_0 = 370$. Specifically, for the HT-type chart, all the 600 in-control structures are applied to estimating the in-control model parameters and calculating both the UCL and LCL. For GLRT-based chart, 100 in-control structures are used to estimate the in-control model parameters, and the other 500 in-control are applied to obtaining the UCL and LCL. 500 out-of-control structures are selected to calculate the ARL_{1s} and anomaly detection powers, which are summarized in Table 5-5. From Table 5-5, the GLRT-based chart outperforms the HT-type chart in terms of ARL_1 , which is consistent with the result in Table 5-3. The GLRT-based chart, without the normality assumption, is more accurate for the anomaly detection on 3D printed carbon composites.

Table 5-5. ARL_{1s} and Detection Power of P_2 using HT-type and GLRT-based charts at Nominal $ARL_0 = 370$

Control Chart	GLRT	HT
ARL_1	1.55	1.61
Detection Power	0.645	0.621

5.6 Conclusion

By virtue of the recent advancement of metrology, the LRD effect has been observed in some 3D structures, and existing conventional 3D spatial models ignore the LRD effect within the 3D structures. Driven by this fact, in this chapter, we proposed a novel 3D spatial model that can capture the LRD effect. An MLE approach is developed to estimate model parameters. Based on the proposed 3D model, we construct two LRD-integrated quality control charts to conduct 3D anomaly detection based on the HT-type and GLRT-based control charts. A simulation study is implemented to verify the proposed method. To further validate the proposed model, a 3D printing experiment on Carbon composites is conducted to perform a real-world case study. The results in both the simulation study and case study show that the proposed method performs significantly good in terms of ARL_1 . Furthermore, the GLRT-based chart, without the normality assumption, is more accurate for anomaly detection in terms of ARL_1 .

CHAPTER 6

CONCLUSIONS AND FUTURE WORKS

The LRD effect has been recently detected in reliability and quality data of various assets and materials. Most existing reliability analysis and anomaly detection methods ignore the LRD effect, which could lead to a biased lifetime distribution or an inaccurate anomaly detection and low product quality. To overcome these challenges, we propose reliability analysis and anomaly detection with considering LRD effects. Specifically, four studies have been conducted.

In Chapter 2, we conduct a reliability analysis considering the LRD effect and measurement errors simultaneously under normal operating conditions. An MLE approach is developed for the model parameter estimation. Based on the model and estimated parameters, a reliability analysis is developed to compute the lifetime distribution of assets. Simulation studies are implemented to evaluate the performance of the proposed model, and a real case study using the capacity degradation of lithium-ion pouch cells is conducted to validate the proposed model. Results reveal that the traditional LRD-integrated models, which ignore the measurement errors, significantly misestimate lifetime uncertainty, while the proposed model provides more accurate life estimations.

In Chapter 3, we predict lifetime distribution conduct reliability analysis integrating the LRD effect under accelerated conditions. An MLE approach is developed for the parameter estimation. A likelihood-ratio hypothesis test is developed based on the proposed model to quantitatively test whether the long-range dependence exists or not. Simulation studies are implemented to verify the performance of the developed methods. Physical experiments are conducted on the degradation of Pt/black TiO₂ to further demonstrate the proposed model. Both simulation and case study results

show that the proposed ADT model, via integrating the LRD effects, fundamentally improves the life testing accuracy, while conventional ADT methods significantly underestimate the lifetime uncertainty.

In Chapter 4, we develop quality control analysis on surface anomaly detection considering LRD. Simulation studies are implemented to investigate the performance of the proposed model, and a case study using real-world wood surface images is conducted to demonstrate the proposed approach. Results show that the proposed spatial modeling and monitoring framework, by considering the two-dimensional spatial LRD effect, significantly outperforms existing surface anomaly detection approaches in terms of detection power and ARL_1 .

In Chapter 5, we propose an LRD-integrated statistical monitoring using 3D composite structure information. A simulation study is implemented to verify the proposed 3D anomaly detection method. To further validate the proposed method, a 3D printing experiment on Carbon composites is conducted to further perform a real case study. The results in both the simulation study and case study show that the proposed method, by considering three-dimensional spatial LRD effect, performs significantly good in terms of ARL_1 . Furthermore, the GLRT-based chart, without the normality assumption, is more accurate than the HT-type chart for anomaly detection in terms of ARL_1 .

In conclusion, for reliability analysis, we discover that ignoring the LRD effect significantly underestimates the uncertainty of the lifetime distribution of assets; For anomaly detection of materials, we find that ignoring the LRD effect will cause an inaccurate feature characterization. In the proposed research, via considering the LRD effect, we achieve high accuracy of both the

reliability analysis and the anomaly detection. Meanwhile, our proposed models significantly outperform multiple existing benchmark approaches.

In this dissertation, for Chapter 2, the random effect of the trend term has been considered in the degradation modeling as widely adopted in the literature. In the future, it would be an interesting topic to further consider the heterogeneity of the Hurst parameter among various degradation paths. Moreover, measurement errors are assumed to be independently and identically distributed (i.i.d.) across degradation signals in the proposed model. Another future topic would be to apply non-identical or correlated distributions to model measurement errors. In Chapter 3, the structure of long-range dependence effects in the proposed ADT model is treated as constant across different accelerating stress levels. An interesting future research topic is to develop an ADT model in which the long-range dependence structure varies over different accelerating stresses when prior physical or empirical information is available. Moreover, in the proposed ADT model the degradations of assets tested at the same stress level are assumed to be statistically independent with a common fixed degradation trend. In the future, to further consider the asset-to-asset variation in the degradation trend using a random-effect method would be another interesting research topic. In Chapter 4, the parameters of the proposed LRD-integrated spatial model are assumed to be constant. In the future, it would be a meaningful study to investigate the random effect of the model parameters and develop a random-effect LRD-integrated spatial model for material surface characterization and quality control. Moreover, in this chapter we develop an LRD-integrated control chart based on the generalized likelihood ratio test. Another interesting future topic would be to develop LRD-integrated quality control charts via other types of quality

control principles, such as EWMA charts and CUSUM charts, on the basis of the proposed LRD-integrated spatial model. In Chapter 5, the 3D samples are assumed to be independent. In the future, it would be a meaningful topic to further consider the dependence among 3D samples. Moreover, in this chapter, the model parameters are assumed to be constant. Another interesting future topic would be to further investigate the random effect of the model parameters and propose a random-effect LRD-integrated 3D model for anomaly detection on 3D materials.

REFERENCES

REFERENCES

- [1] Z. Xu, Y. Hong, and R. Jin, "Nonlinear general path models for degradation data with dynamic covariates," *Applied Stochastic Models in Business Industry*, vol. 32, no. 2, pp. 153-167, 2016.
- [2] Z. Ye, Y. Wang, K. Tsui, and M. Pecht, "Degradation data analysis using Wiener processes with measurement errors," *IEEE Transactions on Reliability*, vol. 62, no. 4, pp. 772-780, 2013.
- [3] X. Fang, N. Z. Gebraeel, and K. Paynabar, "Scalable prognostic models for large-scale condition monitoring applications," *IIEE Transactions*, vol. 49, no. 7, pp. 698-710, 2017.
- [4] X. Xi, M. Chen, and D. Zhou, "Remaining useful life prediction for degradation processes with memory effects," *IEEE Transactions on Reliability*, vol. 66, no. 3, pp. 751-760, 2017.
- [5] W. Si, Y. Shao, and W. Wei, "Accelerated degradation testing with long-term memory effects," *IEEE Transactions on Reliability*, vol. 69, no. 4, pp. 1254-1266, 2020.
- [6] H. Zhang, Z. Mo, J. Wang, and Q. Miao, "Nonlinear-drifted fractional Brownian motion with multiple hidden state variables for remaining useful life prediction of lithium-ion batteries," *IEEE Transactions on Reliability*, vol. 69, no. 2, pp. 768-780, 2020.
- [7] H. Zhang, M. Chen, X. Xi, and D. Zhou, "Remaining useful life prediction for degradation processes with long-range dependence," *IEEE Transactions on Reliability*, vol. 66, no. 4, pp. 1368-1379, 2017.
- [8] T. Sottinen, "Fractional Brownian motion, random walks and binary market models," *Finance Stochastics*, vol. 5, no. 3, pp. 343-355, 2001.
- [9] A. Montanari, "Long-range dependence in hydrology," *Theory and Applications of Long-Range Dependence*, pp. 461-472, 2003.
- [10] K. Burnecki, E. Kepten, J. Janczura, I. Bronshtein, Y. Garini, and A. Weron, "Universal algorithm for identification of fractional Brownian motion. A case of telomere subdiffusion," *Biophysical Journal*, vol. 103, no. 9, pp. 1839-1847, 2012.

- [11] C. J. Lu and W. Meeker, "Using degradation measures to estimate a time-to-failure distribution," *Technometrics*, vol. 35, no. 2, pp. 161-174, 1993.
- [12] Y. Ding, Q. Yang, C. B. King, and Y. Hong, "A General Accelerated Destructive Degradation Testing Model for Reliability Analysis," *IEEE Transactions on Reliability*, 2019.
- [13] S. K. Tse, C. Yang, and H.-K. Yuen, "Statistical analysis of Weibull distributed lifetime data under Type II progressive censoring with binomial removals," *Journal of Applied Statistics*, vol. 27, no. 8, pp. 1033-1043, 2000.
- [14] M. Hack, A. G. Lewis, and I.-W. Wu, "Physical models for degradation effects in polysilicon thin-film transistors," *IEEE transactions on electron devices*, vol. 40, no. 5, pp. 890-897, 1993.
- [15] L. Vichard, N. Y. Steiner, N. Zerhouni, and D. Hissel, "Hybrid fuel cell system degradation modeling methods: A comprehensive review," *Journal of Power Sources*, vol. 506, p. 230071, 2021.
- [16] C.-H. Hu, M.-Y. Lee, and J. Tang, "Optimum step-stress accelerated degradation test for Wiener degradation process under constraints," *European Journal of Operational Research*, vol. 241, no. 2, pp. 412-421, 2015.
- [17] C. Park and W. Padgett, "Accelerated degradation models for failure based on geometric Brownian motion and gamma processes," *Lifetime Data Analysis*, vol. 11, no. 4, pp. 511-527, 2005.
- [18] M. H. Ling, K. L. Tsui, and N. Balakrishnan, "Accelerated degradation analysis for the quality of a system based on the gamma process," *IEEE Transactions on Reliability*, vol. 64, no. 1, pp. 463-472, 2014.
- [19] M. Kim, C. Song, and K. Liu, "A generic health index approach for multisensor degradation modeling and sensor selection," *IEEE Transactions on Automation Science Engineering*, vol. 16, no. 3, pp. 1426-1437, 2019.
- [20] J. Zhu, N. Chen, and W. Peng, "Estimation of bearing remaining useful life based on multiscale convolutional neural network," *IEEE Transactions on Industrial Electronics*, vol. 66, no. 4, pp. 3208-3216, 2018.

- [21] F. Wang, J. Du, Y. Zhao, T. Tang, and J. Shi, "A deep learning based data fusion method for degradation modeling and prognostics," *IEEE Transactions on Reliability*, 2020, DOI: 10.1109/TR.2020.3011500.
- [22] Z.-S. Ye, L.-P. Chen, L. C. Tang, and M. Xie, "Accelerated degradation test planning using the inverse Gaussian process," *IEEE Transactions on Reliability*, vol. 63, no. 3, pp. 750-763, 2014.
- [23] H. Zhang, D. Zhou, M. Chen, and J. Shang, "FBM-based remaining useful life prediction for degradation processes with long-range dependence and multiple modes," *IEEE Transactions on Reliability*, vol. 68, no. 3, pp. 1021-1033, 2018.
- [24] B. M. Colosimo, "Modeling and monitoring methods for spatial and image data," *Quality Engineering*, vol. 30, no. 1, pp. 94-111, 2018.
- [25] J. Baek, M. K. Jeong, and E. A. Elsayed, "Monitoring variations in multimode surface topography," *International Journal of Production Research*, pp. 1-17, 2022.
- [26] A. T. Bui and D. W. Apley, "Monitoring for changes in the nature of stochastic textured surfaces," *Journal of Quality Technology*, vol. 50, no. 4, pp. 363-378, 2018.
- [27] J. Lyu and M. Chen, "Automated visual inspection expert system for multivariate statistical process control chart," *Expert Systems with Applications*, vol. 36, no. 3, pp. 5113-5118, 2009.
- [28] P. Qiu, C. Zou, and Z. Wang, "Nonparametric profile monitoring by mixed effects modeling," *Technometrics*, vol. 52, no. 3, pp. 265-277, 2010.
- [29] O. Ulker, "Surface roughness of composite panels as a quality control tool," *Materials*, vol. 11, no. 3, p. 407, 2018.
- [30] H. Zhang, D. Zhou, M. Chen, and X. Xi, "Predicting remaining useful life based on a generalized degradation with fractional Brownian motion," *Mechanical Systems and Signal Processing*, vol. 115, pp. 736-752, 2019.

- [31] W. Song, X. Chen, C. Cattani, and E. Zio, "Multifractional Brownian motion and quantum-behaved partial swarm optimization for bearing degradation forecasting," *Complexity*, vol. 2020, 2020.
- [32] H. Wang, W. Song, E. Zio, A. Kudreyko, and Y. Zhang, "Remaining useful life prediction for Lithium-ion batteries using fractional Brownian motion and fruit-fly optimization algorithm," *Measurement*, vol. 161, p. 107904, 2020.
- [33] F. L. Schmidt and J. E. Hunter, "Measurement error in psychological research: Lessons from 26 research scenarios," *Psychological Methods*, vol. 1, no. 2, pp. 199-223, 1996.
- [34] D. M. Rocke and B. Durbin, "A model for measurement error for gene expression arrays," *Journal of Computational Biology*, vol. 8, no. 6, pp. 557-569, 2001.
- [35] J. A. Hutcheon, A. Chiolero, and J. A. Hanley, "Random measurement error and regression dilution bias," *British Medical Journal*, vol. 340, 2010.
- [36] J. Miller and J. C. Miller, *Statistics and Chemometrics for Analytical Chemistry*, 6th ed. Pearson education, 2010.
- [37] D. Liu and S. Wang, "Reliability estimation from lifetime testing data and degradation testing data with measurement error based on evidential variable and Wiener process," *Reliability Engineering System Safety*, vol. 205, p. 107231, 2021.
- [38] W. Si, Q. Yang, X. Wu, and Y. Chen, "Reliability analysis considering dynamic material local deformation," *Journal of Quality Technology*, vol. 50, no. 2, pp. 183-197, 2018.
- [39] W. Q. Meeker, L. A. Escobar, and C. J. Lu, "Accelerated degradation tests: Modeling and analysis," *Technometrics*, vol. 40, no. 2, pp. 89-99, 1998.
- [40] L. Lu, B. Wang, Y. Hong, and Z. Ye, "General path models for degradation data with multiple characteristics and covariates," *Technometrics*, 2020, DOI:10.1080/00401706.2020.1796814.
- [41] Z. Ye, M. Xie, L. Tang, and N. Chen, "Semiparametric estimation of gamma processes for deteriorating products," *Technometrics*, vol. 56, no. 4, pp. 504-513, 2014.

- [42] X. Wang and D. Xu, "An inverse Gaussian process model for degradation data," *Technometrics*, vol. 52, no. 2, pp. 188-197, 2010.
- [43] Z. Ye and N. Chen, "The inverse Gaussian process as a degradation model," *Technometrics*, vol. 56, no. 3, pp. 302-311, 2014.
- [44] Z. Ye, Nan Chen, and Yan Shen, "A new class of Wiener process models for degradation analysis," *Reliability Engineering System Safety*, vol. 139, pp. 58-67, 2015.
- [45] Z. Zhang, X. Si, C. Hu, and Y. Lei, "Degradation data analysis and remaining useful life estimation: A review on Wiener-process-based methods," *European Journal of Operational Research*, vol. 271, no. 3, pp. 775-796, 2018.
- [46] G. Whitmore, "Estimating degradation by a Wiener diffusion process subject to measurement error," *Lifetime Data Analysis*, vol. 1, no. 3, pp. 307-319, 1995.
- [47] Y. Zhou and M. Huang, "Lithium-ion batteries remaining useful life prediction based on a mixture of empirical mode decomposition and ARIMA model," *Microelectronics Reliability*, vol. 65, pp. 265-273, 2016.
- [48] B. B. Mandelbrot and J. W. Van Ness, "Fractional Brownian motions, fractional noises and applications," *SIAM Review*, vol. 10, no. 4, pp. 422-437, 1968.
- [49] X. Xi, D. Zhou, and M. Chen, "Prognostics of non-Markovian degradation processes with fractal property and measurement uncertainty," in *2018 3rd International Conference on System Reliability and Safety (ICSRS)*, Barcelona, Spain, 2018, pp. 235-243.
- [50] E. Alòs and D. Nualart, "Stochastic integration with respect to the fractional Brownian motion," *Stochastics and Stochastics Reports*, vol. 75, no. 3, pp. 129-152, 2003.
- [51] G. Casella and R. L. Berger, *Statistical Inference*. Duxbury Pacific Grove, CA, USA, 2002.
- [52] V. Schmidt, *Stochastic Geometry, Spatial Statistics and Random Fields*. Springer, Germany, 2014.

- [53] J. R. Hosking, "Modeling persistence in hydrological time series using fractional differencing," *Water Resources Research*, vol. 20, no. 12, pp. 1898-1908, 1984.
- [54] S. Asmussen, *Stochastic Simulation with a View Towards Stochastic Processes*. Centre for Mathematical Physics and Stochastics, University of Aarhus, Denmark, 1998.
- [55] A. B. Dieker and M. Mandjes, "On spectral simulation of fractional Brownian motion," *Probability in the Engineering and Informational Sciences*, vol. 17, no. 3, pp. 417-434, 2003.
- [56] H. Guo and H. Liao, "Practical approaches for reliability evaluation using degradation data," in *Annual Reliability and Maintainability Symposium*, Palm Harbor, Florida, USA, 2015, vol. 7.
- [57] C. Birkl and D. Howey. *Oxford Battery Degradation Dataset 1-Long term battery ageing tests of 8 Kokam (SLPB533459H4) 740 mAh lithium-ion pouch cells*, 2015-08-01 - 2016-12-31, doi: 10.5287/bodleian:KO2kdmYGg.
- [58] W. B. Nelson, *Accelerated testing: statistical models, test plans, and data analysis*. John Wiley & Sons, 2009.
- [59] L. A. Escobar and W. Q. Meeker, "A review of accelerated test models," *Statistical Science*, vol. 21, no. 4, pp. 552-577, 2006.
- [60] W. Si, Q. Yang, and X. Wu, "A physical–statistical model of overload retardation for crack propagation and application in reliability estimation," *IIE Transactions*, vol. 48, no. 4, pp. 347-358, 2016.
- [61] W. Q. Meeker, L. A. Escobar, and Y. Hong, "Using accelerated life tests results to predict product field reliability," *Technometrics*, vol. 51, no. 2, pp. 146-161, 2009.
- [62] W. Si and Q. Yang, "Accelerated life testing with semiparametric modeling of stress effects," *IEEE Transactions on Reliability*, vol. 66, no. 4, pp. 989-996, 2017.
- [63] H. Liao and E. A. Elsayed, "Reliability inference for field conditions from accelerated degradation testing," *Naval Research Logistics*, vol. 53, no. 6, pp. 576-587, 2006.

- [64] Z. Yang, Y. Chen, Y.-F. Li, E. Zio, and R. Kang, "Smart electricity meter reliability prediction based on accelerated degradation testing and modeling," *International Journal of Electrical Power & Energy Systems*, vol. 56, pp. 209-219, 2014.
- [65] Y. Hong and W. Q. Meeker, "Field-failure predictions based on failure-time data with dynamic covariate information," *Technometrics*, vol. 55, no. 2, pp. 135-149, 2013.
- [66] Y. Chen and J. Jin, "Quality-reliability chain modeling for system-reliability analysis of complex manufacturing processes," *IEEE Transactions on Reliability*, vol. 54, no. 3, pp. 475-488, 2005.
- [67] S. Limon, O. P. Yadav, and H. Liao, "A literature review on planning and analysis of accelerated testing for reliability assessment," *Quality and Reliability Engineering International*, vol. 33, no. 8, pp. 2361-2383, 2017.
- [68] H. Zhang, Z. Mo, J. Wang, and Q. Miao, "Nonlinear-Drifted Fractional Brownian Motion With Multiple Hidden State Variables for Remaining Useful Life Prediction of Lithium-Ion Batteries," *IEEE Transactions on Reliability*, 2019.
- [69] H. Zhang, D. Zhou, M. Chen, and J. Shang, "FBM-Based Remaining Useful Life Prediction for Degradation Processes With Long-Range Dependence and Multiple Modes," *IEEE Transactions on Reliability*, vol. 68, no. 3, 2019.
- [70] X. Xi, M. Chen, H. Zhang, and D. Zhou, "An improved non-Markovian degradation model with long-term dependency and item-to-item uncertainty," *Mechanical Systems and Signal Processing*, vol. 105, pp. 467-480, 2018.
- [71] B. Mo, J. Yu, D. Tang, and H. Liu, "A remaining useful life prediction approach for lithium-ion batteries using Kalman filter and an improved particle filter," in *2016 IEEE international conference on Prognostics and Health Management (ICPHM)*, 2016: IEEE, pp. 1-5.
- [72] W. Willinger, M. S. Taqqu, and V. Teverovsky, "Stock market prices and long-range dependence," *Finance and Stochastics*, vol. 3, no. 1, pp. 1-13, 1999.

- [73] A. Witt and B. D. Malamud, "Quantification of long-range persistence in geophysical time series: conventional and benchmark-based improvement techniques," *Surveys in Geophysics*, vol. 34, no. 5, pp. 541-651, 2013.
- [74] A. Krishnamachari, "Sequence variability and long-range dependence in DNA: An information theoretic perspective," in *International Conference on Neural Information Processing*, 2004: Springer, pp. 1354-1361.
- [75] T. Karagiannis, M. Molle, and M. Faloutsos, "Long-range dependence ten years of Internet traffic modeling," *IEEE Internet Computing*, vol. 8, no. 5, pp. 57-64, 2004.
- [76] Y. Xie, Z. Jin, Y. Hong, and J. H. Van Mullekom, "Statistical methods for thermal index estimation based on accelerated destructive degradation test data," in *Statistical modeling for degradation data*: Springer, 2017, pp. 231-251.
- [77] H. Endicott, B. Hatch, and R. Sohmer, "Application of the Eyring model to capacitor aging data," *IEEE Transactions on Component Parts*, vol. 12, no. 1, pp. 34-41, 1965.
- [78] E. Redondo-Iglesias, P. Venet, and S. Pelissier, "Global model for self-discharge and capacity fade in lithium-ion batteries based on the generalized Eyring relationship," *IEEE Transactions on Vehicular Technology*, vol. 67, no. 1, pp. 104-113, 2018.
- [79] D. Kececioglu and J. A. Jacks, "The Arrhenius, Eyring, inverse power law and combination models in accelerated life testing," *Reliability Engineering*, vol. 8, no. 1, pp. 1-9, 1984.
- [80] Y. Ding, Q. Yang, C. B. King, and Y. Hong, "A General Accelerated Destructive Degradation Testing Model for Reliability Analysis," *IEEE Transactions on Reliability*, vol. 68, no. 4, 2019.
- [81] J.-J. H. Shiau and H.-H. Lin, "Analyzing accelerated degradation data by nonparametric regression," *IEEE Transactions on Reliability*, vol. 48, no. 2, pp. 149-158, 1999.
- [82] P. M. Robinson, *Time series with long memory*. Advanced Texts in Econometrics, 2003.
- [83] J. R. M. Hosking, "Fractional Differencing," *Biometrika*, vol. 68, no. 1, pp. 165-176, 1981, doi: 10.2307/2335817.

- [84] J. Beran, Y. Feng, S. Ghosh, and R. Kulik, *Long-Memory Processes*. Springer, 2016.
- [85] M. S. Taqqu, *Theory and Applications of Long-range Dependence*. Birkhäuser Basel, 2003, pp. 5-38.
- [86] O. Lepskii, "On a problem of adaptive estimation in Gaussian white noise," *Theory of Probability & Its Applications*, vol. 35, no. 3, pp. 454-466, 1991.
- [87] O. O. Aalen and H. K. Gjessing, "Survival models based on the Ornstein-Uhlenbeck process," *Lifetime Data Analysis*, vol. 10, no. 4, pp. 407-423, 2004.
- [88] M. Peiris and B. Perera, "On prediction with fractionally differenced ARIMA models," *Journal of Time Series Analysis*, vol. 9, no. 3, pp. 215-220, 1988.
- [89] I. Norros, "On the use of fractional Brownian motion in the theory of connectionless networks," *IEEE Journal on Selected Areas in Communications*, vol. 13, no. 6, pp. 953-962, 1995.
- [90] T. Szabados, "Strong approximation of fractional Brownian motion by moving averages of simple random walks," *Stochastic Processes and Their Applications*, vol. 92, no. 1, pp. 31-60, 2001.
- [91] A. T. Wood and G. Chan, "Simulation of stationary Gaussian processes in $[0, 1]^d$," *Journal of Computational and Graphical statistics*, vol. 3, no. 4, pp. 409-432, 1994.
- [92] J. A. Nelder and R. J. T. c. j. Mead, "A simplex method for function minimization," vol. 7, no. 4, pp. 308-313, 1965.
- [93] J. Fan, C. Zhang, and J. Zhang, "Generalized likelihood ratio statistics and Wilks phenomenon," *The Annals of Statistics*, vol. 29, no. 1, pp. 153-193, 2001.
- [94] F. J. Richard, "Anisotropy of Hölder Gaussian random fields: characterization, estimation, and application to image textures," *Statistics and Computing*, vol. 28, no. 6, pp. 1155-1168, 2018.

- [95] M. Lee, M. G. Genton, and M. Jun, "Testing self-similarity through Lamperti transformations," *Journal of agricultural, biological, environmental statistics*, vol. 21, no. 3, pp. 426-447, 2016.
- [96] H. Rabiei, O. Coulon, J. Lefèvre, and F. J. Richard, "Surface regularity via the estimation of fractional Brownian motion index," *IEEE Transactions on Image Processing*, vol. 30, pp. 1453-1460, 2020.
- [97] S. Lahmiri, S. Bekiros, and A. Salvi, "Long-range memory, distributional variation and randomness of bitcoin volatility," *Chaos, Solitons Fractals*, vol. 107, pp. 43-48, 2018.
- [98] T. Iliopoulou, S. M. Papalexiou, Y. Markonis, and D. Koutsoyiannis, "Revisiting long-range dependence in annual precipitation," *Journal of Hydrology*, vol. 556, pp. 891-900, 2018.
- [99] A. Wang, K. Wang, and F. Tsung, "Statistical surface monitoring by spatial-structure modeling," *Journal of Quality Technology*, vol. 46, no. 4, pp. 359-376, 2014.
- [100] E. H. Glaessgen, C. M. Pastore, O. H. Griffin, and A. Birger, "Geometrical and finite element modelling of textile composites," *Composites Part B: Engineering*, vol. 27, no. 1, pp. 43-50, 1996.
- [101] Z. Wang, X. Huan, and K. Garikipati, "Variational system identification of the partial differential equations governing microstructure evolution in materials: Inference over sparse and spatially unrelated data," *Computer Methods in Applied Mechanics Engineering*, vol. 377, p. 113706, 2021.
- [102] Z. Ran, Z. Yongkang, S. Guifang, S. Xuting, and L. Pu, "Finite element analysis of surface roughness generated by multiple laser shock peening," *Rare metal materials and engineering*, vol. 47, no. 1, pp. 33-38, 2018.
- [103] G. Xu, Q. Pan, and C. L. Bajaj, "Discrete surface modelling using partial differential equations," *Computer Aided Geometric Design*, vol. 23, no. 2, pp. 125-145, 2006.
- [104] F. L. Matthews, G. Davies, D. Hitchings, and C. Soutis, *Finite element modelling of composite materials and structures*. Elsevier, 2000.

- [105] X. Lu *et al.*, "Finite element analysis and experimental validation of the thermomechanical behavior in laser solid forming of Ti-6Al-4V," *Additive Manufacturing*, vol. 21, pp. 30-40, 2018.
- [106] N. Mera, "Efficient optimization processes using kriging approximation models in electrical impedance tomography," *International journal for numerical methods in engineering*, vol. 69, no. 1, pp. 202-220, 2007.
- [107] R. Jin, C.-J. Chang, and J. Shi, "Sequential measurement strategy for wafer geometric profile estimation," *IIE Transactions*, vol. 44, no. 1, pp. 1-12, 2012.
- [108] N. Zhang and Q. Yang, "A random effect autologistic regression model with application to the characterization of multiple microstructure samples," *IIE Transactions*, vol. 48, no. 1, pp. 34-42, 2016, doi: 10.1080/0740817X.2015.1047069.
- [109] W. Si, Q. Yang, and X. Wu, "A distribution-based functional linear model for reliability analysis of advanced high-strength dual-phase steels by utilizing material microstructure images," *IIE Transactions*, vol. 49, no. 9, pp. 863-873, 2017.
- [110] S. Valette and P. Rémy, "Wavelet-based multiresolution analysis of irregular surface meshes," *IEEE Transactions on Visualization Computer Graphics*, vol. 10, no. 2, pp. 113-122, 2004.
- [111] J. Liu, C. Liu, Y. Bai, P. Rao, C. B. Williams, and Z. Kong, "Layer-wise spatial modeling of porosity in additive manufacturing," *IIE Transactions*, vol. 51, no. 2, pp. 109-123, 2019.
- [112] N. Zhang and D. W. Apley, "Fractional Brownian fields for response surface metamodeling," *Journal of Quality Technology*, vol. 46, no. 4, pp. 285-301, 2014.
- [113] H. Jia, Y. L. Murphey, J. Shi, and T.-S. Chang, "An intelligent real-time vision system for surface defect detection," in *Proceedings of the 17th International Conference on Pattern Recognition, 2004. ICPR 2004.*, 2004, vol. 3: IEEE, pp. 239-242.
- [114] Y. Huang, C. Qiu, and K. Yuan, "Surface defect saliency of magnetic tile," *The Visual Computer*, vol. 36, no. 1, pp. 85-96, 2020.

- [115] H. Zheng, L. Fang, M. Ji, M. Strese, Y. Özer, and E. Steinbach, "Deep learning for surface material classification using haptic and visual information," *IEEE Transactions on Multimedia*, vol. 18, no. 12, pp. 2407-2416, 2016.
- [116] A. Mujeeb, W. Dai, M. Erdt, and A. Sourin, "Unsupervised surface defect detection using deep autoencoders and data augmentation," in *2018 International Conference on Cyberworlds (CW)*, 2018: IEEE, pp. 391-398.
- [117] X. Yue, J. G. Park, Z. Liang, and J. Shi, "Tensor mixed effects model with application to nanomanufacturing inspection," *Technometrics*, vol. 62, no. 1, pp. 116-129, 2020.
- [118] J. Du, H. Yan, T.-S. Chang, and J. Shi, "A Tensor Voting-Based Surface Anomaly Classification Approach by Using 3D Point Cloud Data," *Journal of Manufacturing Science and Engineering*, vol. 144, no. 5, p. 051005, 2021.
- [119] V. Pipiras and M. S. Taqqu, *Long-range dependence and self-similarity*. Cambridge university press, 2017.
- [120] E. Karapetian and S. V. Kalinin, "Point force and generalized point source on the surface of semi-infinite transversely isotropic material," *Journal of Applied Physics*, vol. 110, no. 5, p. 052020, 2011.
- [121] E. Herbin, "From N parameter fractional Brownian motions to N parameter multifractional Brownian motions," *The Rocky Mountain Journal of Mathematics*, pp. 1249-1284, 2006.
- [122] D. T. Hristopulos, "Permissibility of fractal exponents and models of band-limited two-point functions for fGn and fBm random fields," *Stochastic Environmental Research and Risk Assessment*, vol. 17, no. 3, pp. 191-216, 2003.
- [123] S. H. Yoo *et al.*, "Foldecture as a core material with anisotropic surface characteristics," *Journal of the American Chemical Society*, vol. 137, no. 6, pp. 2159-2162, 2015.
- [124] Y. Liu, J. Zhu, and D. K. Lin, "A generalized likelihood ratio test for monitoring profile data," *Journal of Applied Statistics*, vol. 48, no. 8, pp. 1402-1415, 2021.

- [125] Z. He, L. Zuo, M. Zhang, and F. M. Megahed, "An image-based multivariate generalized likelihood ratio control chart for detecting and diagnosing multiple faults in manufactured products," *International Journal of Production Research*, vol. 54, no. 6, pp. 1771-1784, 2016.
- [126] A. Krishnamoorthy and D. Menon, "Matrix inversion using Cholesky decomposition," in *2013 signal processing: Algorithms, architectures, arrangements, and applications (SPA)*, 2013: IEEE, pp. 70-72.
- [127] S. S. Prabhu and G. C. Runger, "Designing a multivariate EWMA control chart," *Journal of Quality Technology*, vol. 29, no. 1, pp. 8-15, 1997.
- [128] R. Sun and F. Tsung, "A kernel-distance-based multivariate control chart using support vector methods," *International Journal of Production Research*, vol. 41, no. 13, pp. 2975-2989, 2003.
- [129] H.-M. Ngai and J. Zhang, "Multivariate cumulative sum control charts based on projection pursuit," *Statistica Sinica*, pp. 747-766, 2001.
- [130] H. Rue and L. Held, *Gaussian Markov random fields: theory and applications*. Florida, USA: Chemical Rubber Company press, 2005.
- [131] H. Biermé, "Introduction to random fields and scale invariance," in *Stochastic geometry*: Springer, 2019, pp. 129-180.
- [132] D. Khoshnevisan and Y. Xiao, "Images of the Brownian sheet," *Transactions of the American Mathematical Society*, vol. 359, no. 7, pp. 3125-3151, 2007.
- [133] P. Bergmann, M. Fauser, D. Sattlegger, and C. Steger, "MVTec AD--A comprehensive real-world dataset for unsupervised anomaly detection," in *Proceedings of the IEEE/CVF conference on computer vision and pattern recognition*, 2019, pp. 9592-9600.
- [134] M. T. Guerreiro *et al.*, "Anomaly detection in automotive industry using clustering methods—A case study," *Applied Sciences*, vol. 11, no. 21, p. 9868, 2021.

- [135] S. H. Seifi, W. Tian, H. Doude, M. A. Tschopp, and L. Bian, "Layer-wise modeling and anomaly detection for laser-based additive manufacturing," *Journal of Manufacturing Science and Engineering*, vol. 141, no. 8, p. 081013, 2019.
- [136] N. Silva, J. Soares, V. Shah, M. Y. Santos, and H. Rodrigues, "Anomaly detection in roads with a data mining approach," *Procedia computer science*, vol. 121, pp. 415-422, 2017.
- [137] R. Magán-Carrión, J. Camacho, and P. García-Teodoro, "Multivariate statistical approach for anomaly detection and lost data recovery in wireless sensor networks," *International Journal of Distributed Sensor Networks*, vol. 11, no. 6, p. 672124, 2015.
- [138] P. Parandoush, C. Zhou, and D. Lin, "3D printing of ultrahigh strength continuous carbon fiber composites," *Advanced Engineering Materials*, vol. 21, no. 2, p. 1800622, 2019.
- [139] F. Aslam, S. Latif, and P. Ferreira, "Investigating long-range dependence of emerging Asian stock markets using multifractal detrended fluctuation analysis," *Symmetry*, vol. 12, no. 7, p. 1157, 2020.
- [140] P. Kohli, "Fractional bivariate exponential estimator for long-range dependent random field," *Spatial Statistics*, vol. 15, pp. 22-38, 2016.
- [141] L. Jiang, H. Xu, J. Liu, X. Shen, S. Lu, and Z. Shi, "Anomaly detection of industrial multi-sensor signals based on enhanced spatiotemporal features," *Neural Computing and Applications*, vol. 34, no. 11, pp. 8465-8477, 2022.
- [142] H. Chen, H. Ma, X. Chu, and D. Xue, "Anomaly detection and critical attributes identification for products with multiple operating conditions based on isolation forest," *Advanced Engineering Informatics*, vol. 46, p. 101139, 2020.
- [143] F. Boud and N. N. Gindy, "Application of multi-sensor signals for monitoring tool/workpiece condition in broaching," *International Journal of Computer Integrated Manufacturing*, vol. 21, no. 6, pp. 715-729, 2008.
- [144] P. Jakob, M. Madan, T. Schmid-Schirling, and A. Valada, "Multi-perspective anomaly detection," *Sensors*, vol. 21, no. 16, p. 5311, 2021.

- [145] L. Erhan *et al.*, "Smart anomaly detection in sensor systems: A multi-perspective review," *Information Fusion*, vol. 67, pp. 64-79, 2021.
- [146] Y. Zhang, Y. Chen, J. Wang, and Z. Pan, "Unsupervised deep anomaly detection for multi-sensor time-series signals," *IEEE Transactions on Knowledge and Data Engineering*, 2021.
- [147] C.-J. Lu and D.-M. J. T. I. J. o. A. M. T. Tsai, "Automatic defect inspection for LCDs using singular value decomposition," *The International Journal of Advanced Manufacturing Technology*, vol. 25, no. 1, pp. 53-61, 2005.
- [148] F. Imani, R. Chen, E. Diewald, E. Reutzel, and H. Yang, "Deep learning of variant geometry in layerwise imaging profiles for additive manufacturing quality control," *Journal of Manufacturing Science Engineering*, vol. 141, no. 11, p. 111001, 2019.
- [149] L. Zuo, Z. He, and M. Zhang, "An EWMA and region growing based control chart for monitoring image data," *Quality Technology & Quantitative Management*, vol. 17, no. 4, pp. 470-485, 2020.
- [150] M. N. Bisheh, S. I. Chang, and S. Lei, "A layer-by-layer quality monitoring framework for 3D printing," *Computers Industrial Engineering*, vol. 157, p. 107314, 2021.
- [151] L. Scime, D. Siddel, S. Baird, and V. Paquit, "Layer-wise anomaly detection and classification for powder bed additive manufacturing processes: A machine-agnostic algorithm for real-time pixel-wise semantic segmentation," *Additive Manufacturing*, vol. 36, p. 101453, 2020.
- [152] C. Tao, J. Du, and T.-S. Chang, "Anomaly Detection for Fabricated Artifact by Using Unstructured 3D Point Cloud Data," *IISE Transactions*, no. just-accepted, pp. 1-29, 2022.
- [153] P. Bergmann and D. Sattlegger, "Anomaly detection in 3d point clouds using deep geometric descriptors," in *Proceedings of the IEEE/CVF Winter Conference on Applications of Computer Vision*, 2023, pp. 2613-2623.
- [154] M. Masuda, R. Hachiuma, R. Fujii, H. Saito, and Y. Sekikawa, "Toward unsupervised 3d point cloud anomaly detection using variational autoencoder," in *2021 IEEE International Conference on Image Processing (ICIP)*, 2021: IEEE, pp. 3118-3122.

- [155] N. D. Tracy, J. C. Young, and R. L. Mason, "Multivariate control charts for individual observations," *Journal of quality technology*, vol. 24, no. 2, pp. 88-95, 1992.
- [156] I. Goodfellow *et al.*, "Generative Adversarial Networks," *Advances in neural information processing systems* 27, 2014.
- [157] C. Pozrikidis, *An Introduction to Grids, Graphs, and Networks*. Oxford University Press, UK, 2014.
- [158] W. H. Press, S. A. Teukolsky, W. T. Vetterling, and B. P. Flannery, *Numerical Recipes: The Art of Scientific Computing, 3rd edition*. Cambridge University Press, UK, 2007.
- [159] D. Puplinskaitė and D. Surgailis, "Aggregation of autoregressive random fields and anisotropic long-range dependence," *Bernoulli*, vol. 22, no. 4, pp. 2401-2441, 2016.

APPENDIXES

APPENDIXES

A1 Proof of Proposition 2.1

Using the vector denotation, the matrix \mathbf{Q} in Equation (14) can be written as

$\mathbf{Q} = s_\alpha^2 \mathbf{f} \mathbf{f}^T + \mathbf{C}$. We obtain the determinant of \mathbf{Q} as

$$\det(\mathbf{Q}) = \det(s_\alpha^2 \mathbf{f} \mathbf{f}^T + \mathbf{C}) = \det(\mathbf{C}(\mathbf{I} + \mathbf{C}^{-1} s_\alpha^2 \mathbf{f} \mathbf{f}^T)) = \det(\mathbf{C}) \det(\mathbf{I} + \mathbf{C}^{-1} s_\alpha^2 \mathbf{f} \mathbf{f}^T) \quad (111)$$

Using Sylvester's determinant theorem [157], $\det(\mathbf{Q})$ is derived as

$$\det(\mathbf{Q}) = \det(\mathbf{C}) \det(\mathbf{I} + \mathbf{C}^{-1} s_\alpha^2 \mathbf{f} \mathbf{f}^T) = \det(\mathbf{C}) (1 + s_\alpha^2 \mathbf{f}^T \mathbf{C}^{-1} \mathbf{f}) \quad (112)$$

By applying the Sherman-Morrison formula [158], the inverse matrix of \mathbf{Q} can be calculated by

$$\mathbf{Q}^{-1} = (s_\alpha^2 \mathbf{f} \mathbf{f}^T + \mathbf{C})^{-1} = \mathbf{C}^{-1} - \frac{s_\alpha^2 \mathbf{C}^{-1} \mathbf{f} \mathbf{f}^T \mathbf{C}^{-1}}{1 + s_\alpha^2 \mathbf{f}^T \mathbf{C}^{-1} \mathbf{f}} \quad (113)$$

We then substitute Equations (112) and (113) into (14), and the following log-likelihood function

is obtained:

$$\begin{aligned} l(\boldsymbol{\eta} | \mathbf{Y}) = & -\frac{KN}{2} \ln(2\pi) - \frac{K}{2} \ln(\det(\mathbf{C}) (1 + s_\alpha^2 \mathbf{f}^T \mathbf{C}^{-1} \mathbf{f})) - \\ & \frac{1}{2} \sum_{j=1}^K (\mathbf{Y}_j - \mu_\alpha \mathbf{f})^T \left(\mathbf{C}^{-1} - \frac{s_\alpha^2 \mathbf{C}^{-1} \mathbf{f} \mathbf{f}^T \mathbf{C}^{-1}}{1 + s_\alpha^2 \mathbf{f}^T \mathbf{C}^{-1} \mathbf{f}} \right) (\mathbf{Y}_j - \mu_\alpha \mathbf{f}) \end{aligned} \quad (114)$$

To maximize $l(\boldsymbol{\eta} | \mathbf{Y})$, we calculate its partial derivatives with respect to parameters μ_α

and s_α^2 , and set these two derivatives to 0. The following equations are derived:

$$\frac{\partial l(\boldsymbol{\eta} | \mathbf{Y})}{\partial \mu_\alpha} = \sum_{j=1}^K \mathbf{Y}_j^T \left(\mathbf{C}^{-1} - \frac{s_\alpha^2 \mathbf{C}^{-1} \mathbf{f} \mathbf{f}^T \mathbf{C}^{-1}}{1 + s_\alpha^2 \mathbf{f}^T \mathbf{C}^{-1} \mathbf{f}} \right) \mathbf{f} - \mu_\alpha \sum_{j=1}^K \mathbf{f}^T \left(\mathbf{C}^{-1} - \frac{s_\alpha^2 \mathbf{C}^{-1} \mathbf{f} \mathbf{f}^T \mathbf{C}^{-1}}{1 + s_\alpha^2 \mathbf{f}^T \mathbf{C}^{-1} \mathbf{f}} \right) \mathbf{f} = 0 \quad (115)$$

$$\frac{\partial l(\boldsymbol{\eta} | \mathbf{Y})}{\partial s_\alpha^2} = -K \mathbf{f}^T \mathbf{C}^{-1} \mathbf{f} (1 + s_\alpha^2 \mathbf{f}^T \mathbf{C}^{-1} \mathbf{f}) + \sum_{j=1}^K (\mathbf{f}^T \mathbf{C}^{-1} \mathbf{Y}_j)^2 + \frac{\left(\sum_{j=1}^K \mathbf{Y}_j^T \mathbf{C}^{-1} \mathbf{f} \right)^2}{K} = 0 \quad (116)$$

By solving Equations (115) and (116), we obtain the MLE estimators of μ_α and s_α^2 as in (15) and

(16), respectively. This completes the proof of Proposition 2.1.

A2 Details of $W_1 \sim W_6$

The results of $W_1 \sim W_6$ in Equations (19) and (20) are derived as follows:

$$W_1 = \frac{\sum_{j=1}^K \mathbf{Y}_j^T \mathbf{C}^{-1} \frac{\partial \mathbf{C}}{\partial \sigma^2} \mathbf{C}^{-1} \mathbf{f}}{K \mathbf{f}^T \mathbf{C}^{-1} \mathbf{f}} - \frac{K \mathbf{f}^T \mathbf{C}^{-1} \frac{\partial \mathbf{C}}{\partial \sigma^2} \mathbf{C}^{-1} \mathbf{f} \sum_{j=1}^K \mathbf{Y}_j^T \mathbf{C}^{-1} \mathbf{f}}{(K \mathbf{f}^T \mathbf{C}^{-1} \mathbf{f})^2} \quad (117)$$

$$W_2 = \frac{\sum_{j=1}^K \mathbf{Y}_j^T \mathbf{C}^{-1} \frac{\partial \mathbf{C}}{\partial H} \mathbf{C}^{-1} \mathbf{f}}{K \mathbf{f}^T \mathbf{C}^{-1} \mathbf{f}} - \frac{K \mathbf{f}^T \mathbf{C}^{-1} \frac{\partial \mathbf{C}}{\partial H} \mathbf{C}^{-1} \mathbf{f} \sum_{j=1}^K \mathbf{Y}_j^T \mathbf{C}^{-1} \mathbf{f}}{(K \mathbf{f}^T \mathbf{C}^{-1} \mathbf{f})^2} \quad (118)$$

$$W_3 = \frac{\sum_{j=1}^K \mathbf{Y}_j^T \mathbf{C}^{-1} \mathbf{C}^{-1} \mathbf{f}}{K \mathbf{f}^T \mathbf{C}^{-1} \mathbf{f}} - \frac{K \mathbf{f}^T \mathbf{C}^{-1} \mathbf{C}^{-1} \mathbf{f} \sum_{j=1}^K \mathbf{Y}_j^T \mathbf{C}^{-1} \mathbf{f}}{(K \mathbf{f}^T \mathbf{C}^{-1} \mathbf{f})^2} \quad (119)$$

$$W_4 = \frac{\mathbf{f}^T \mathbf{C}^{-1} \frac{\partial \mathbf{C}}{\partial \sigma^2} \mathbf{C}^{-1} \mathbf{f}}{(\mathbf{f}^T \mathbf{C}^{-1} \mathbf{f})^2} + \frac{\sum_{j=1}^K 2 \mathbf{Y}_j^T \mathbf{C}^{-1} \mathbf{f} \mathbf{Y}_j^T \mathbf{C}^{-1} \frac{\partial \mathbf{C}}{\partial \sigma^2} \mathbf{C}^{-1} \mathbf{f}}{K (\mathbf{f}^T \mathbf{C}^{-1} \mathbf{f})^2} - \frac{2 K \mathbf{f}^T \mathbf{C}^{-1} \mathbf{f} \mathbf{f}^T \mathbf{C}^{-1} \frac{\partial \mathbf{C}}{\partial \sigma^2} \mathbf{C}^{-1} \mathbf{f} \sum_{j=1}^K (\mathbf{Y}_j^T \mathbf{C}^{-1} \mathbf{f})^2}{K^2 (\mathbf{f}^T \mathbf{C}^{-1} \mathbf{f})^4} + \frac{2 \left(\sum_{j=1}^K \mathbf{Y}_j^T \mathbf{C}^{-1} \mathbf{f} \right) \left(\sum_{j=1}^K \mathbf{Y}_j^T \mathbf{C}^{-1} \frac{\partial \mathbf{C}}{\partial \sigma^2} \mathbf{C}^{-1} \mathbf{f} \right)}{(K \mathbf{f}^T \mathbf{C}^{-1} \mathbf{f})^2} + \frac{2 K^2 \mathbf{f}^T \mathbf{C}^{-1} \mathbf{f} \mathbf{f}^T \mathbf{C}^{-1} \frac{\partial \mathbf{C}}{\partial \sigma^2} \mathbf{C}^{-1} \mathbf{f} \left(\sum_{j=1}^K \mathbf{Y}_j^T \mathbf{C}^{-1} \mathbf{f} \right)^2}{(K \mathbf{f}^T \mathbf{C}^{-1} \mathbf{f})^4} \quad (120)$$

$$W_5 = \frac{\mathbf{f}^T \mathbf{C}^{-1} \frac{\partial \mathbf{C}}{\partial H} \mathbf{C}^{-1} \mathbf{f}}{(\mathbf{f}^T \mathbf{C}^{-1} \mathbf{f})^2} + \frac{\sum_{j=1}^K 2 \mathbf{Y}_j^T \mathbf{C}^{-1} \mathbf{f} \mathbf{Y}_j^T \mathbf{C}^{-1} \frac{\partial \mathbf{C}}{\partial H} \mathbf{C}^{-1} \mathbf{f}}{K (\mathbf{f}^T \mathbf{C}^{-1} \mathbf{f})^2} - \frac{2 K \mathbf{f}^T \mathbf{C}^{-1} \mathbf{f} \mathbf{f}^T \mathbf{C}^{-1} \frac{\partial \mathbf{C}}{\partial H} \mathbf{C}^{-1} \mathbf{f} \sum_{j=1}^K (\mathbf{Y}_j^T \mathbf{C}^{-1} \mathbf{f})^2}{K^2 (\mathbf{f}^T \mathbf{C}^{-1} \mathbf{f})^4} + \frac{2 \left(\sum_{j=1}^K \mathbf{Y}_j^T \mathbf{C}^{-1} \mathbf{f} \right) \left(\sum_{j=1}^K \mathbf{Y}_j^T \mathbf{C}^{-1} \frac{\partial \mathbf{C}}{\partial H} \mathbf{C}^{-1} \mathbf{f} \right)}{(K \mathbf{f}^T \mathbf{C}^{-1} \mathbf{f})^2} + \frac{2 K^2 \mathbf{f}^T \mathbf{C}^{-1} \mathbf{f} \mathbf{f}^T \mathbf{C}^{-1} \frac{\partial \mathbf{C}}{\partial H} \mathbf{C}^{-1} \mathbf{f} \left(\sum_{j=1}^K \mathbf{Y}_j^T \mathbf{C}^{-1} \mathbf{f} \right)^2}{(K \mathbf{f}^T \mathbf{C}^{-1} \mathbf{f})^4} \quad (121)$$

$$\begin{aligned}
W_6 = & \frac{\mathbf{f}^T \mathbf{C}^{-1} \mathbf{C}^{-1} \mathbf{f}}{(\mathbf{f}^T \mathbf{C}^{-1} \mathbf{f})^2} + \frac{\sum_{j=1}^K 2\mathbf{Y}_j^T \mathbf{C}^{-1} \mathbf{f} \mathbf{Y}_j^T \mathbf{C}^{-1} \mathbf{C}^{-1} \mathbf{f}}{K(\mathbf{f}^T \mathbf{C}^{-1} \mathbf{f})^2} - \frac{2K\mathbf{f}^T \mathbf{C}^{-1} \mathbf{f} \mathbf{f}^T \mathbf{C}^{-1} \mathbf{C}^{-1} \mathbf{f} \sum_{j=1}^K (\mathbf{Y}_j^T \mathbf{C}^{-1} \mathbf{f})^2}{K^2 (\mathbf{f}^T \mathbf{C}^{-1} \mathbf{f})^4} - \\
& \frac{2 \left(\sum_{j=1}^K \mathbf{Y}_j^T \mathbf{C}^{-1} \mathbf{f} \right) \left(\sum_{j=1}^K \mathbf{Y}_j^T \mathbf{C}^{-1} \mathbf{C}^{-1} \mathbf{f} \right)}{(K\mathbf{f}^T \mathbf{C}^{-1} \mathbf{f})^2} + \frac{2K^2 \mathbf{f}^T \mathbf{C}^{-1} \mathbf{f} \mathbf{f}^T \mathbf{C}^{-1} \mathbf{C}^{-1} \mathbf{f} \left(\sum_{j=1}^K \mathbf{Y}_j^T \mathbf{C}^{-1} \mathbf{f} \right)^2}{(K\mathbf{f}^T \mathbf{C}^{-1} \mathbf{f})^4}
\end{aligned} \tag{122}$$

and the (u,v) th entry of matrices $\frac{\partial \mathbf{C}}{\partial \sigma^2}$ and $\frac{\partial \mathbf{C}}{\partial H}$ is calculated, respectively, by

$$\left(\frac{\partial \mathbf{C}}{\partial \sigma^2} \right)_{uv} = \begin{cases} \frac{1}{2} (t_u^{2H} + t_v^{2H} - |t_u - t_v|^{2H}); & \text{for } u = v \\ \frac{1}{2} (t_u^{2H} + t_v^{2H} - |t_u - t_v|^{2H}); & \text{for } u \neq v \end{cases} \tag{123}$$

$$\left(\frac{\partial \mathbf{C}}{\partial H} \right)_{uv} = \begin{cases} \sigma^2 (t_u^{2H} \ln(t_u) + t_v^{2H} \ln(t_v)); & \text{for } u = v \\ \sigma^2 (t_u^{2H} \ln(t_u) + t_v^{2H} \ln(t_v) - |t_u - t_v|^{2H} \ln|t_u - t_v|); & \text{for } u \neq v \end{cases} \tag{124}$$

A3 Effect of Signal-to-Noise Ratio

A simulation study is conducted to verify the proposed model under various amplitude levels of measurement errors. Specifically, based on model P_3 , degradation paths are generated under three higher levels of measurement errors, i.e., $d^2 = 0.1, 0.5$ and 1.0 , while all other parameters are the same as described in Section 2.4.2. Using the MLE approach, the parameter estimation results are obtained and summarized in Table A-1.

From Table A-1, it can be seen that the point estimates of model parameters are all close to the specified values, which demonstrates the robustness of the proposed model under various levels of signal-to-noise ratio. To further verify the proposed model, reliability analyses are also conducted under a failure threshold of $y_{th} = 100$. The PDFs of lifetime along with the true lifetime histogram are illustrated in Figure A.1. It can be seen that the predicted lifetime distributions under

the three levels of measurement errors are all close to the true lifetime distribution. This further demonstrates the robustness of the proposed model under various levels of signal-to-noise ratio.

Table A-1. Point Estimates and Standard Errors of P_3 Parameters under Three Levels of Measurement Errors

$P_3 (d^2 = 0.1)$		
Parameter	Point Estimate	Standard Error
H	0.880	0.0372
σ^2	0.406	0.0787
d^2	0.103	0.00739
μ_α	5.24	0.0304
s_α^2	0.532	0.223
β	0.684	0.0159
$P_3 (d^2 = 0.5)$		
Parameter	Point Estimate	Standard Error
H	0.841	0.0531
σ^2	0.468	0.0771
d^2	0.482	0.0297
μ_α	5.09	0.0688
s_α^2	1.09	0.181
β	0.703	0.0171

Table A-1-Part 2. Point Estimates and Standard Errors of P_3 Parameters under Three Levels of Measurement Errors

$P_3 (d^2 = 1.0)$		
Parameter	Point Estimate	Standard Error
H	0.839	0.0562
σ^2	0.527	0.0832
d^2	1.03	0.0573
μ_α	5.41	0.102
s_α^2	0.585	0.192
β	0.683	0.0213

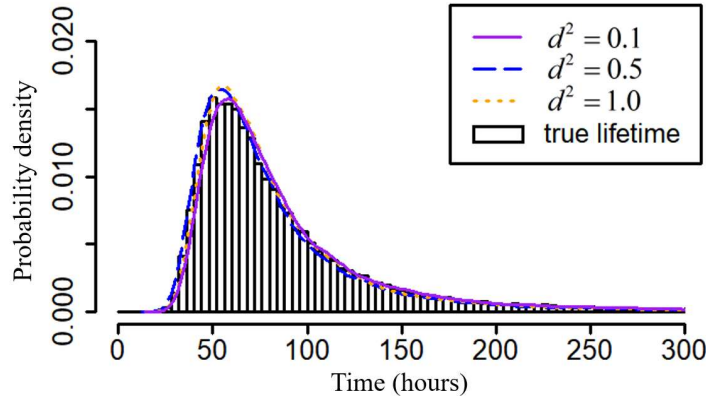


Figure A.1. PDFs of predicted lifetime using P_3 when $d^2 = 0.1, 0.5$ and 1.0

A4 A Probability Check on the proposed ADT model

For the proposed ADT model, we did a check on the probabilities that: *a*) the degradation level Y is not larger than one at relatively small time, and *b*) Y is not negative at relatively large time, in both the simulation and case studies under the normal use temperature.

Specifically, based on the theory of fractional Brownian motion the degradation observation at time t , denoted as Y_t , follows a normal distribution. That is, $Y_t \sim N\left(D_0 \exp(-R_u \times AF(temp) \times t), \sigma^2 t^{2H}\right)$. Therefore, the probabilities that the degradation is not larger than 1 or is non-negative can be calculated as follows:

$$P(Y_t \leq 1) = \Phi\left(\frac{1 - D_0 \exp(-R_u \times AF(temp) \times t)}{\sigma t^H}\right)$$

$$P(Y_t \geq 0) = 1 - \Phi\left(\frac{-D_0 \exp(-R_u \times AF(temp) \times t)}{\sigma t^H}\right)$$

where $\Phi(\bullet)$ is the cumulative distribution function of a standard normal distribution. Based on the aforementioned two equations, we computed the probabilities under situations *a*) and *b*), respectively. The results for the simulation and case studies are illustrated in Figures A.2 and A.3,

respectively. It can be seen that in all cases, the probabilities are relatively large and close to one so that the proposed model is practical for use.

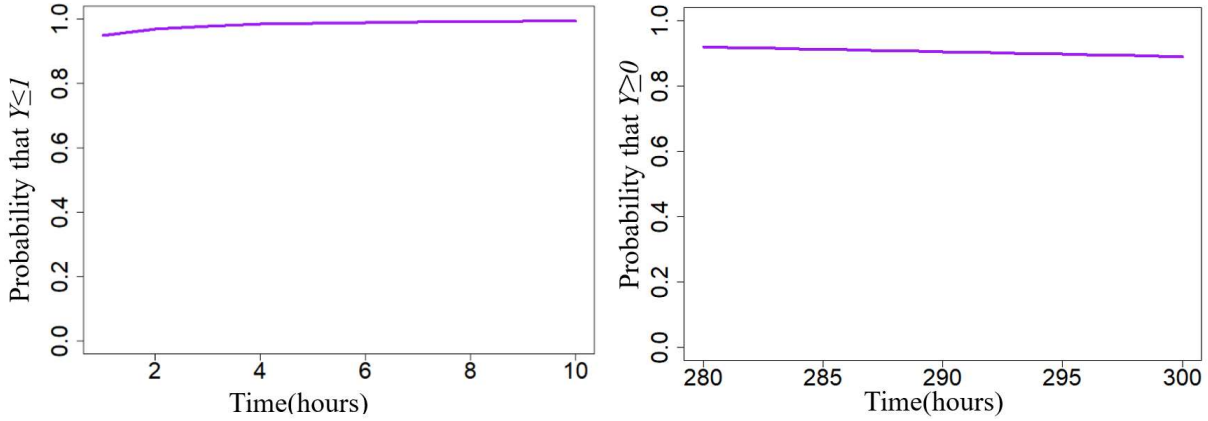


Figure A.2. $P(Y \leq 1)$ for small t (left) and $P(Y \geq 0)$ for large t (right) of the simulation study

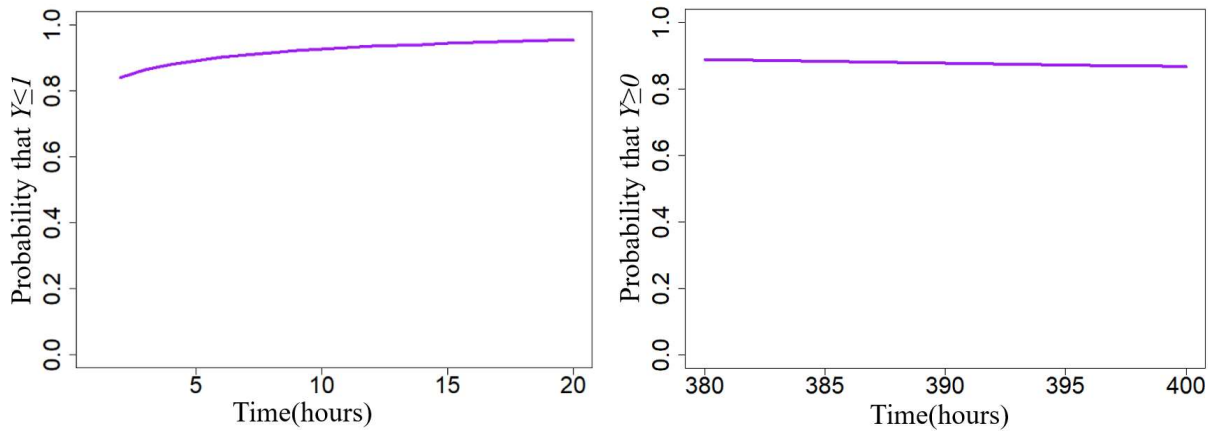


Figure A.3. $P(Y \leq 1)$ for small t (left) and $P(Y \geq 0)$ for large t (right) of the case study

A5 Proof of Spatial LRD in the Proposed Anisotropic Model

To show the existence of LRD in the proposed anisotropic spatial model, we first calculate the rectangular increments of the FBS. The FBS $\{B_{H_x, H_y}(x, y) | (x, y) \in \mathbb{R}^2\}$ is a random field with stationary rectangular increments defined as follows [159]:

$$Y_{H_x, H_y}(k, l) = B_{H_x, H_y}(k, l) - B_{H_x, H_y}(k-1, l) - B_{H_x, H_y}(k, l-1) + B_{H_x, H_y}(k-1, l-1); k, l \in \mathbb{Z}_+ \quad (125)$$

The covariance function of $Y_{H_x, H_y}(k, l)$ can be obtained as:

$$\begin{aligned}
\gamma_Y(m, n) &= \text{Cov}(Y_{H_x, H_y}(k, l), Y_{H_x, H_y}(k+m, l+n)) \\
&= \text{Cov} \left(\begin{array}{l} \left(B_{H_x, H_y}(k, l) - B_{H_x, H_y}(k-1, l) - \right. \\ \left. B_{H_x, H_y}(k, l-1) + B_{H_x, H_y}(k-1, l-1) \right) \\ \left(B_{H_x, H_y}(k+m, l+n) - B_{H_x, H_y}(k+m-1, l+n) - \right. \\ \left. B_{H_x, H_y}(k+m, l+n-1) + B_{H_x, H_y}(k+m-1, l+n-1) \right) \end{array} \right) \\
&= \frac{1}{2} \left(|m-1|^{2H_x} + |m+1|^{2H_x} - 2|m|^{2H_x} \right) \times \frac{1}{2} \left(|n-1|^{2H_y} + |n+1|^{2H_y} - 2|n|^{2H_y} \right) \\
&= E \left((B_{H_x}(k) - B_{H_x}(k-1))(B_{H_x}(k+m) - B_{H_x}(k+m-1)) \right) \times \\
&\quad E \left((B_{H_y}(l) - B_{H_y}(l-1))(B_{H_y}(l+m) - B_{H_y}(l+m-1)) \right) \\
&= \text{Cov}(X_{H_x}(k), X_{H_x}(k+m)) \text{Cov}(X_{H_y}(l), X_{H_y}(l+n))
\end{aligned} \tag{126}$$

where $X_{H_x}(k) = B_{H_x}(k) - B_{H_x}(k-1)$ and $X_{H_y}(l) = B_{H_y}(l) - B_{H_y}(l-1)$ are the incremental processes of the standard one-dimensional fractional Brownian motions $B_{H_x}(k)$ and $B_{H_y}(l)$, respectively. The standard fractional Brownian motion $\{B_H(t) | t \in R\}$ is a stochastic process with a Hurst parameter H , and the autocovariance function of its stationary incremental process $\{X_H(k) = B_H(k) - B_H(k-1) | k \in Z_+\}$ is calculated as:

$$\begin{aligned}
\gamma_{X_H}(d) &= \text{Cov}(X_H(k), X_H(k+d)) \\
&= E \left((B_H(k) - B_H(k-1))(B_H(k+d) - B_H(k+d-1)) \right) \\
&= \frac{1}{2} \left(|d-1|^{2H} + |d+1|^{2H} - 2|d|^{2H} \right)
\end{aligned} \tag{127}$$

Based on the autocovariance function, the spectral density function of $X_H(k)$ can be derived as [119]:

$$\begin{aligned}
f_{X_H}(\omega) &= \frac{1}{2\pi} \sum_{d=-\infty}^{+\infty} e^{-i\omega d} \gamma_{X_H}(d) \\
&= \frac{\Gamma(2H+1)\sin(H\pi)}{2\pi} |1 - e^{-i\omega}|^2 \sum_{d=-\infty}^{+\infty} |\omega + 2\pi d|^{-1-2H} \\
&\sim \frac{\Gamma(2H+1)\sin(H\pi)}{2\pi} |\omega|^{1-2H} \quad \text{as } \omega \rightarrow 0
\end{aligned} \tag{128}$$

Using the autocovariance $\gamma_Y(m, n)$, the spectral density function of $Y_{H_x, H_y}(k, l)$ is then calculated as:

$$\begin{aligned}
s(\omega_1, \omega_2) &= \left(\frac{1}{2\pi}\right)^2 \sum_{m=-\infty}^{+\infty} \sum_{n=-\infty}^{+\infty} e^{-i\omega_1 m - i\omega_2 n} \gamma_Y(m, n) = \left(\frac{1}{2\pi}\right)^2 \sum_{m=-\infty}^{+\infty} \sum_{n=-\infty}^{+\infty} e^{-i\omega_1 m - i\omega_2 n} \gamma_{X_{H_x}}(m) \gamma_{X_{H_y}}(n) \\
&= \left(\frac{1}{2\pi} \sum_{m=-\infty}^{+\infty} e^{-i\omega_1 m} \gamma_{X_{H_x}}(m)\right) \left(\frac{1}{2\pi} \sum_{n=-\infty}^{+\infty} e^{-i\omega_2 n} \gamma_{X_{H_y}}(n)\right)
\end{aligned} \tag{129}$$

Substituting Equation (128) in Equation (129), $s(\omega_1, \omega_2)$ can be further reduced as:

$$\begin{aligned}
s(\omega_1, \omega_2) &= \frac{\Gamma(2H_x+1)\sin(H_x\pi)}{2\pi} |1 - e^{-i\omega_1}|^2 \sum_{d=-\infty}^{+\infty} |\omega_1 + 2\pi d|^{-1-2H_x} \\
&\quad \frac{\Gamma(2H_y+1)\sin(H_y\pi)}{2\pi} |1 - e^{-i\omega_2}|^2 \sum_{d=-\infty}^{+\infty} |\omega_2 + 2\pi d|^{-1-2H_y} \\
&= f_{X_{H_x}}(\omega_1) f_{X_{H_y}}(\omega_2) \\
&\sim \frac{\Gamma(2H_x+1)\sin(H_x\pi)}{2\pi} \frac{\Gamma(2H_y+1)\sin(H_y\pi)}{2\pi} |\omega_1|^{1-2H_x} |\omega_2|^{1-2H_y} \quad \text{as } \omega_1, \omega_2 \rightarrow 0
\end{aligned} \tag{130}$$

It can be observed that when $H_x, H_y \in (0.5, 1)$, Equation (130) satisfies the condition of the anisotropic spatial LRD effect specified in Equation (61). Therefore, the proposed anisotropic spatial model can capture the anisotropic spatial LRD effect along x and y directions, respectively.

A6 Interval Estimation of the Model Parameters

A6.1 Isotropic Scenario

We first consider the proposed isotropic spatial model. By the theory of MLE, the maximum likelihood estimator of in-control model parameters $\hat{\boldsymbol{\theta}}$ follows a multivariate normal

distribution asymptotically. Its covariance matrix \mathbf{O} is calculated as the inverse of the observed Fisher's information matrix $\mathbf{I}(\hat{\boldsymbol{\theta}}')$ i.e., $\mathbf{O}=\mathbf{I}(\hat{\boldsymbol{\theta}}')^{-1}$, and $\mathbf{I}(\hat{\boldsymbol{\theta}}')$ can be computed via the log-likelihood function (72) as [51]:

$$\mathbf{I}(\hat{\boldsymbol{\theta}}') = - \left. \frac{\partial^2 l(\boldsymbol{\theta}' | \mathbf{z})}{\partial \boldsymbol{\theta}'^2} \right|_{\boldsymbol{\theta}' = \hat{\boldsymbol{\theta}}'} \quad (131)$$

Therefore, the standard error of a parameter estimator $\hat{\theta}_i \in \hat{\boldsymbol{\theta}}'$, denoted as $se(\hat{\theta}_i)$, can be calculated as the square root of the corresponding diagonal element in \mathbf{O} , denoted as $se(\hat{\theta}_i) = \sqrt{o_{ii}}$, where o_{uv} is the (u,v) th entry of matrix \mathbf{O} . As $\hat{\theta}_i$ follows a normal distribution asymptotically, the $100(1-\alpha)\%$ confidence interval of θ_i can be constructed as $(\hat{\theta}_i - z_{1-\alpha/2} \times se(\hat{\theta}_i), \hat{\theta}_i + z_{1-\alpha/2} \times se(\hat{\theta}_i))$, where z_p represents the p -quantile of a standard normal distribution. In addition to estimators $\hat{\boldsymbol{\theta}}'$, for model parameters α and σ^2 , the standard errors of their estimators can be computed through Equation (71) using the Delta rule as follows:

$$se(\hat{\alpha}) = \text{sqrt} \left(\left(\frac{\sum_{i=1}^{i=M} \left(\mathbf{z}_i^T \mathbf{C}^{-1} \mathbf{f} \mathbf{f}^T \mathbf{C}^{-1} \frac{\partial \mathbf{C}}{\partial H} \mathbf{C}^{-1} \mathbf{f} - \mathbf{z}_i^T \mathbf{C}^{-1} \frac{\partial \mathbf{C}}{\partial H} \mathbf{C}^{-1} \mathbf{f} \mathbf{f}^T \mathbf{C}^{-1} \mathbf{f} \right)}{M(\mathbf{f}^T \mathbf{C}^{-1} \mathbf{f})^2} se(\hat{H}) \right)^2 + \left(\frac{\partial \hat{\alpha}}{\partial \theta_{f1}} se(\hat{\theta}_{f1}) \right)^2 + \left(\frac{\partial \hat{\alpha}}{\partial \theta_{f2}} se(\hat{\theta}_{f2}) \right)^2 + \dots + \left(\frac{\partial \hat{\alpha}}{\partial \theta_{fn}} se(\hat{\theta}_{fn}) \right)^2 \right) \quad (132)$$

$$se(\widehat{\sigma}^2) = \text{sqr}t \left(\left(\left(\frac{\sum_{i=1}^{i=M} \mathbf{z}_i^T \mathbf{C}^{-1} \frac{\partial \mathbf{C}}{\partial H} \mathbf{C}^{-1} \mathbf{z}_i}{MN} \right) \right. \right. \\ \left. \left. \begin{array}{l} \left(\left(\sum_{i=1}^{i=M} \mathbf{z}_i^T \mathbf{C}^{-1} \mathbf{f} \right)^2 \mathbf{f}^T \mathbf{C}^{-1} \frac{\partial \mathbf{C}}{\partial H} \mathbf{C}^{-1} \mathbf{f} \\ -2 \left(\sum_{i=1}^{i=M} \mathbf{z}_i^T \mathbf{C}^{-1} \mathbf{f} \right) \left(-\sum_{i=1}^{i=M} \mathbf{z}_i^T \mathbf{C}^{-1} \frac{\partial \mathbf{C}}{\partial H} \mathbf{C}^{-1} \mathbf{f} \right) \mathbf{f}^T \mathbf{C}^{-1} \mathbf{f} \end{array} \right) se(\widehat{H}) \right. \\ \left. \left. \frac{\right)}{M^2 N (\mathbf{f}^T \mathbf{C}^{-1} \mathbf{f})^2} \right)^2 \\ + \left(\frac{\partial \widehat{\sigma}^2}{\partial \theta_{f_1}} se(\widehat{\theta}_{f_1}) \right)^2 + \left(\frac{\partial \widehat{\sigma}^2}{\partial \theta_{f_2}} se(\widehat{\theta}_{f_2}) \right)^2 + \dots + \left(\frac{\partial \widehat{\sigma}^2}{\partial \theta_{f_n}} se(\widehat{\theta}_{f_n}) \right)^2 \right) \quad (133)$$

where the (i,j) th entry of matrix $\frac{\partial \mathbf{C}}{\partial H}$ can be calculated via:

$$\left(\frac{\partial \mathbf{C}}{\partial H} \right)_{ij} = \begin{cases} \frac{1}{2} \left((x_i^2 + y_i^2)^H \ln(x_i^2 + y_i^2) + (x_j^2 + y_j^2)^H \ln(x_j^2 + y_j^2) \right); & \text{for } i = j \\ \frac{1}{2} \left((x_i^2 + y_i^2)^H \ln(x_i^2 + y_i^2) + (x_j^2 + y_j^2)^H \ln(x_j^2 + y_j^2) \right. \\ \left. - \left((x_i - x_j)^2 + (y_i - y_j)^2 \right)^H \ln \left((x_i - x_j)^2 + (y_i - y_j)^2 \right) \right); & \text{for } i \neq j \end{cases} \quad (134)$$

A6.2 Anisotropic Scenario

For the proposed anisotropic spatial model, we can first calculate the standard errors of $\widehat{\boldsymbol{\theta}}$ using the inverse of the observed Fisher information matrix based on the log-likelihood function (72). Based on the standard errors of $\widehat{\boldsymbol{\theta}}$, the standard errors of $\widehat{\alpha}$ and $\widehat{\sigma}^2$ are calculated through Equation (71) using the Delta rule, which are listed as follows:

$$se(\hat{\alpha}) = \text{sqrt} \left(\left(\frac{\sum_{i=1}^{i=M} \left(\mathbf{z}_i^T \mathbf{C}^{-1} \mathbf{f} \mathbf{f}^T \mathbf{C}^{-1} \frac{\partial \mathbf{C}}{\partial H_x} \mathbf{C}^{-1} \mathbf{f} - \mathbf{z}_i^T \mathbf{C}^{-1} \frac{\partial \mathbf{C}}{\partial H_x} \mathbf{C}^{-1} \mathbf{f} \mathbf{f}^T \mathbf{C}^{-1} \mathbf{f} \right)}{M(\mathbf{f}^T \mathbf{C}^{-1} \mathbf{f})^2} se(\widehat{H}_x) \right)^2 + \left(\frac{\sum_{i=1}^{i=M} \left(\mathbf{z}_i^T \mathbf{C}^{-1} \mathbf{f} \mathbf{f}^T \mathbf{C}^{-1} \frac{\partial \mathbf{C}}{\partial H_y} \mathbf{C}^{-1} \mathbf{f} - \mathbf{z}_i^T \mathbf{C}^{-1} \frac{\partial \mathbf{C}}{\partial H_y} \mathbf{C}^{-1} \mathbf{f} \mathbf{f}^T \mathbf{C}^{-1} \mathbf{f} \right)}{M(\mathbf{f}^T \mathbf{C}^{-1} \mathbf{f})^2} se(\widehat{H}_y) \right)^2 + \left(\frac{\partial \hat{\alpha}}{\partial \theta_{f_1}} se(\widehat{\theta}_{f_1}) \right)^2 + \left(\frac{\partial \hat{\alpha}}{\partial \theta_{f_2}} se(\widehat{\theta}_{f_2}) \right)^2 + \dots + \left(\frac{\partial \hat{\alpha}}{\partial \theta_{f_n}} se(\widehat{\theta}_{f_n}) \right)^2 \right) \quad (135)$$

$$se(\widehat{\sigma}^2) = \text{sqrt} \left(\left(\left(\frac{\sum_{i=1}^{i=M} \mathbf{z}_i^T \mathbf{C}^{-1} \frac{\partial \mathbf{C}}{\partial H_x} \mathbf{C}^{-1} \mathbf{z}_i}{MN} - \frac{\left(\sum_{i=1}^{i=M} \mathbf{z}_i^T \mathbf{C}^{-1} \mathbf{f} \right)^2 \mathbf{f}^T \mathbf{C}^{-1} \frac{\partial \mathbf{C}}{\partial H_x} \mathbf{C}^{-1} \mathbf{f}}{M^2 N (\mathbf{f}^T \mathbf{C}^{-1} \mathbf{f})^2} \right)}{M^2 N (\mathbf{f}^T \mathbf{C}^{-1} \mathbf{f})^2} se(\widehat{H}_x) \right)^2 + \left(\frac{\sum_{i=1}^{i=M} \mathbf{z}_i^T \mathbf{C}^{-1} \frac{\partial \mathbf{C}}{\partial H_y} \mathbf{C}^{-1} \mathbf{z}_i}{MN} - \frac{\left(\sum_{i=1}^{i=M} \mathbf{z}_i^T \mathbf{C}^{-1} \mathbf{f} \right)^2 \mathbf{f}^T \mathbf{C}^{-1} \frac{\partial \mathbf{C}}{\partial H_y} \mathbf{C}^{-1} \mathbf{f}}{M^2 N (\mathbf{f}^T \mathbf{C}^{-1} \mathbf{f})^2} \right)^2 se(\widehat{H}_y) \right)^2 + \left(\frac{\partial \widehat{\sigma}^2}{\partial \theta_{f_1}} se(\widehat{\theta}_{f_1}) \right)^2 + \left(\frac{\partial \widehat{\sigma}^2}{\partial \theta_{f_2}} se(\widehat{\theta}_{f_2}) \right)^2 + \dots + \left(\frac{\partial \widehat{\sigma}^2}{\partial \theta_{f_n}} se(\widehat{\theta}_{f_n}) \right)^2 \right) \quad (136)$$

where the (i,j) th entry of matrix $\frac{\partial \mathbf{C}}{\partial H_x}$ and $\frac{\partial \mathbf{C}}{\partial H_y}$ can be calculated via the following equations:

$$\left(\frac{\partial \mathbf{C}}{\partial H_x}\right)_{ij} = \begin{cases} \frac{1}{2} \left(\frac{y_i^{2Hy} + y_j^{2Hy}}{|y_i - y_j|^{2Hy}} \right) \left(x_i^{2Hx} \ln x_i + x_j^{2Hx} \ln x_j \right); & \text{for } x_i = x_j \\ \frac{1}{2} \left(\frac{y_i^{2Hy} + y_j^{2Hy}}{|y_i - y_j|^{2Hy}} \right) \left(\frac{x_i^{2Hx} \ln x_i + x_j^{2Hx} \ln x_j}{-|x_i - x_j|^{2Hx} \ln |x_i - x_j|} \right); & \text{for } x_i \neq x_j \end{cases} \quad (137)$$

$$\left(\frac{\partial \mathbf{C}}{\partial H_y}\right)_{ij} = \begin{cases} \frac{1}{2} \left(\frac{x_i^{2Hx} + x_j^{2Hx}}{|x_i - x_j|^{2Hx}} \right) \left(y_i^{2Hy} \ln y_i + y_j^{2Hy} \ln y_j \right); & \text{for } y_i = y_j \\ \frac{1}{2} \left(\frac{x_i^{2Hx} + x_j^{2Hx}}{|x_i - x_j|^{2Hx}} \right) \left(\frac{y_i^{2Hy} \ln y_i + y_j^{2Hy} \ln y_j}{-|y_i - y_j|^{2Hy} \ln |y_i - y_j|} \right); & \text{for } y_i \neq y_j \end{cases} \quad (138)$$

A7 Proof of Proposition 5.1

The FBS $\{B_H(x, y, z) | (x, y, z) \in R^3\}$ is a random field defined in a three-dimensional space with stationary cubic increments, i.e., three-dimensional fractional Gaussian noise (FGN), defined as follows:

$$\begin{aligned} Y_H(k, l, j) = & B_H(k, l, j) - B_H(k-1, l, j) - B_H(k, l-1, j) - \\ & B_H(k, l, j-1) + B_H(k-1, l-1, j) + B_H(k, l-1, j-1) + \\ & B_H(k-1, l, j-1) - B_H(k-1, l-1, j-1); k, l, j \in Z_+ \end{aligned} \quad (139)$$

Based on the definition, it can be shown that the summation of three-dimensional FGN is the FBS as follows:

$$B_H(o, f, g) = \sum_{k=1}^o \sum_{l=1}^f \sum_{j=1}^g Y_H(k, l, j) \quad (140)$$

Using the covariance function of FBS in Equation (94), the covariance function of $Y_H(k, l, j)$ can be calculate as:

$$\begin{aligned}
\gamma_Y(m, n, w) &= \text{Cov}(X_H(k, l, j), X_H(k+m, l+n, j+w)) \\
&= \text{Cov} \left(\begin{array}{l} \left(B_H(k, l, j) - B_H(k-1, l, j) - B_H(k, l-1, j) - \right. \\ \left. B_H(k, l, j-1) + B_H(k-1, l-1, j) + B_H(k, l-1, j-1) \right), \\ \left. + B_H(k-1, l, j-1) - B_H(k-1, l-1, j-1) \right) \\ \left(B_H(k+m, l+n, j+w) - B_H(k+m-1, l+n, j+w) - \right. \\ \left. B_H(k+m, l+n-1, j+w) - B_H(k+m, l+n, j+w-1) + \right. \\ \left. B_H(k+m-1, l+n-1, j+w) + B_H(k+m, l+n-1, j+w-1) + \right. \\ \left. B_H(k+m-1, l+n, j+w-1) - B_H(k+m-1, l+n-1, j+w-1) \right) \end{array} \right) \\
&= \frac{1}{2} \left(|m-1|^{2H_x} + |m+1|^{2H_x} - 2|m|^{2H_x} \right) \times \frac{1}{2} \left(|n-1|^{2H_y} + |n+1|^{2H_y} - 2|n|^{2H_y} \right) \\
&\quad \times \frac{1}{2} \left(|w-1|^{2H_z} + |w+1|^{2H_z} - 2|w|^{2H_z} \right) \\
&= E \left((B_{H_x}(k) - B_{H_x}(k-1))(B_{H_x}(k+m) - B_{H_x}(k+m-1)) \right) \times \\
&\quad E \left((B_{H_y}(l) - B_{H_y}(l-1))(B_{H_y}(l+n) - B_{H_y}(l+n-1)) \right) \times \\
&\quad E \left((B_{H_z}(j) - B_{H_z}(j-1))(B_{H_z}(j+w) - B_{H_z}(j+w-1)) \right) \\
&= \text{Cov}(X_{H_x}(k), X_{H_x}(k+m)) \times \text{Cov}(X_{H_y}(l), X_{H_y}(l+n)) \times \\
&\quad \text{Cov}(X_{H_z}(j), X_{H_z}(j+w))
\end{aligned} \tag{141}$$

where $X_{H_x}(k) = B_{H_x}(k) - B_{H_x}(k-1)$, $X_{H_y}(l) = B_{H_y}(l) - B_{H_y}(l-1)$ and

$X_{H_z}(j) = B_{H_z}(j) - B_{H_z}(j-1)$ are the incremental processes of the standard one-dimensional

fractional Brownian motions $B_{H_x}(k)$, $B_{H_y}(l)$ and $B_{H_z}(j)$, respectively. The standard fractional

Brownian motion $\{B_H(t) | t \in R\}$ is a stochastic process with a Hurst parameter H , and the

autocovariance function of its stationary incremental process

$\{X_H(k) = B_H(k) - B_H(k-1) | k \in Z_+\}$ is calculated as:

$$\begin{aligned}
\gamma_{X_H}(d) &= \text{Cov}(X_H(k), X_H(k+d)) \\
&= E \left((B_H(k) - B_H(k-1))(B_H(k+d) - B_H(k+d-1)) \right) \\
&= \frac{1}{2} \left(|d-1|^{2H} + |d+1|^{2H} - 2|d|^{2H} \right)
\end{aligned} \tag{142}$$

Based on the autocovariance function, the spectral density function of $X_H(k)$ can be derived as [119]:

$$\begin{aligned}
f_{X_H}(\omega) &= \frac{1}{2\pi} \sum_{d=-\infty}^{+\infty} e^{-i\omega k} \gamma_{X_H}(d) \\
&= \frac{\Gamma(2H+1)\sin(H\pi)}{2\pi} |1 - e^{-i\omega}|^2 \sum_{d=-\infty}^{+\infty} |\omega + 2\pi d|^{-1-2H} \\
&\sim \frac{\Gamma(2H+1)\sin(H\pi)}{2\pi} |\omega|^{1-2H} \quad \text{as } \omega \rightarrow 0
\end{aligned} \tag{143}$$

Based on the autocovariance $Y_H(k, l, j)$, the spectral density function of $Y_H(k, l, j)$ is then obtained as:

$$\begin{aligned}
s(\omega_1, \omega_2, \omega_3) &= \left(\frac{1}{2\pi}\right)^2 \sum_{m=-\infty}^{+\infty} \sum_{n=-\infty}^{+\infty} \sum_{w=-\infty}^{+\infty} e^{-i\omega_1 m - i\omega_2 n - i\omega_3 w} \gamma_Y(m, n, w) \\
&= \left(\frac{1}{2\pi}\right)^2 \sum_{m=-\infty}^{+\infty} \sum_{n=-\infty}^{+\infty} \sum_{w=-\infty}^{+\infty} e^{-i\omega_1 m - i\omega_2 n - i\omega_3 w} \gamma_{X_{Hx}}(m) \gamma_{X_{Hy}}(n) \gamma_{X_{Hz}}(w) \\
&= \left(\frac{1}{2\pi} \sum_{m=-\infty}^{+\infty} e^{-i\omega_1 m} \gamma_{X_{Hx}}(m)\right) \left(\frac{1}{2\pi} \sum_{n=-\infty}^{+\infty} e^{-i\omega_2 n} \gamma_{X_{Hy}}(n)\right) \\
&\quad \left(\frac{1}{2\pi} \sum_{w=-\infty}^{+\infty} e^{-i\omega_3 w} \gamma_{X_{Hz}}(w)\right)
\end{aligned} \tag{144}$$

Via substituting Equation (143) into Equation (144), $s(\omega_1, \omega_2, \omega_3)$ is further calculated as:

$$\begin{aligned}
s(\omega_1, \omega_2, \omega_3) &= \frac{\Gamma(2H_x + 1)\sin(H_x\pi)}{2\pi} \left|1 - e^{-i\omega_1}\right|^2 \sum_{d=-\infty}^{+\infty} |\omega_1 + 2\pi d|^{-1-2H_x} \\
&\quad \frac{\Gamma(2H_y + 1)\sin(H_y\pi)}{2\pi} \left|1 - e^{-i\omega_2}\right|^2 \sum_{d=-\infty}^{+\infty} |\omega_2 + 2\pi d|^{-1-2H_y} \\
&\quad \frac{\Gamma(2H_z + 1)\sin(H_z\pi)}{2\pi} \left|1 - e^{-i\omega_3}\right|^2 \sum_{d=-\infty}^{+\infty} |\omega_3 + 2\pi d|^{-1-2H_z} \\
&= f_{X_{H_x}}(\omega_1) f_{X_{H_y}}(\omega_2) f_{X_{H_z}}(\omega_3) \\
&\sim \left(\begin{array}{c} \frac{\Gamma(2H_x + 1)\sin(H_x\pi)}{2\pi} \\ \frac{\Gamma(2H_y + 1)\sin(H_y\pi)}{2\pi} \\ \frac{\Gamma(2H_z + 1)\sin(H_z\pi)}{2\pi} \end{array} \right) |\omega_1|^{1-2H_x} |\omega_2|^{1-2H_y} |\omega_3|^{1-2H_z} \quad \text{as } \omega_1, \omega_2, \omega_3 \rightarrow 0
\end{aligned} \tag{145}$$

It can be observed that when $H_x, H_y, H_z \in (0.5, 1)$, Equation (145) satisfies the condition of the spatial LRD effect specified in Equation (61). Therefore, the proposed anisotropic spatial model can capture the anisotropic spatial LRD effect along x , y and z directions, respectively.